



**UNIVERSIDAD NACIONAL AUTÓNOMA DE MÉXICO**  
PROGRAMA DE MAESTRÍA Y DOCTORADO EN INGENIERÍA

INGENIERÍA EN EXPLORACIÓN Y EXPLOTACIÓN EN RECURSOS  
NATURALES – YACIMIENTOS

**EXPERIMENTAL MECHANICS OF FRACTURED POROUS ROCKS**

TESIS

QUE PARA OPTAR POR EL GRADO DE:

**DOCTOR EN INGENIERÍA**

PRESENTA:

**DANIEL CABRERA SOTELO**

TUTOR PRINCIPAL

DR. FERNANDO SAMANIEGO VERDUZCO,  
FACULTAD DE INGENIERÍA

CIUDAD UNIVERSITARIA, CD. MX. JUNIO 2021



Universidad Nacional  
Autónoma de México



**UNAM – Dirección General de Bibliotecas**  
**Tesis Digitales**  
**Restricciones de uso**

**DERECHOS RESERVADOS ©**  
**PROHIBIDA SU REPRODUCCIÓN TOTAL O PARCIAL**

Todo el material contenido en esta tesis esta protegido por la Ley Federal del Derecho de Autor (LFDA) de los Estados Unidos Mexicanos (México).

El uso de imágenes, fragmentos de videos, y demás material que sea objeto de protección de los derechos de autor, será exclusivamente para fines educativos e informativos y deberá citar la fuente donde la obtuvo mencionando el autor o autores. Cualquier uso distinto como el lucro, reproducción, edición o modificación, será perseguido y sancionado por el respectivo titular de los Derechos de Autor.


**JURADO ASIGNADO:**

Presidente: Dr. Ricardo J. Padilla Y Sánchez  
Secretario: Dr. Erick Emanuel Luna Rojero  
1 er. Vocal: Dr. Fernando Samaniego Verduzco  
2 do. Vocal: Dr. Sergio Berumen Campos  
3 er. Vocal: Dr. Jorge Carrera Bolaños

Lugar o lugares donde se realizó la tesis: Facultad de Ingeniería, UNAM, Ciudad de México.

**TUTOR DE TESIS:**

Dr. Fernando Samaniego Verduzco



---

**FIRMA**

## Resumen

Este trabajo presenta nuevas metodologías experimentales para la medición e interpretación de propiedades petrofísicas avanzadas en rocas fracturadas y areniscas. La clasificación propuesta para rocas está basada en las propiedades petrofísicas más importantes como porosidad efectiva, permeabilidad, compresibilidad, el esfuerzo experimental aplicado. El límite de esfuerzo efectivo aplicado puede ser considerado un criterio experimental de falla en rocas.

La determinación experimental de las elipses representativas del tensor de permeabilidades permite la estimación de las permeabilidades direccionales como función del esfuerzo efectivo de confinamiento aplicado. El tensor experimental de permeabilidades permite estimar y discretizar la permeabilidad del sistema matriz – fractura, aspecto fundamental, para estudiar el comportamiento de flujo y la saturación de aceite residual, ya que la morfología de las rocas de doble porosidad esta afectada por la presión de confinamiento.

Se presenta el diseño de un desplazamiento inmisible agua – aceite, para determinar la saturación de aceite residual en rocas de doble porosidad. Un nuevo numero adimensional, para el tiempo de desplazamiento fue obtenido mediante análisis dimensional. Dicha expresión es una generalización del tiempo adimensional obtenido por Mattax y Kytte, ya que incluye la relación de esfuerzos aplicados. Además, se presenta la similitud física mediante números adimensionales entre el desplazamiento de laboratorio y el comportamiento de yacimiento.

Finalmente, las pruebas experimentales planteadas pueden ser implementadas como pruebas de rutina para el análisis de núcleos. Los datos obtenidos mediante análisis experimental son fundamentales para el desarrollo de y validación de modelos matemáticos que representan el comportamiento constitutivo Termo-Hidro-Mecánico y Químico (THMQ) para rocas vulgares y fracturadas.

## Abstract

This thesis presents new petrophysical methods for obtaining and characterizing physical properties of fractured carbonate and sandstone rocks. The proposed classification of rocks is based on the petrophysical properties of porosity, permeability, compressibility and experimental effective stress. The stress condition can be established as a failure criterion for fractured rocks.

The experimental determination of the permeability tensor ellipses, allows identifying the directional permeabilities of the analyzed rock and the dependence on the effective confining stress. The experimental permeability tensor contributes to discretize the values of the properties of the fractures and the matrix system, key aspect for the estimation of the residual oil saturations in the double porosity system (matrix and fractures), since the morphology of the rock is affected by the confining pressure.

The design of an immiscible displacement test (gas - oil, water - oil) is presented to determine the residual oil saturation in porous fractured rocks. With dimensional analysis, a new dimensionless geomechanical time was obtained for each of the displacements. The expression is a generalization of the time of Mattax and Kytte, that includes a stress ratio. Also, the physical similitude of the displacement in the laboratory was compared with the reservoir behavior.

Finally, the experimental tests proposed in this work can be easily implemented in routine core analysis. The valuable information obtained by the experiments can be applied in the development and validation of advanced mathematical models, of coupled THMC (Thermo-Hydro-Mechanical and Chemical) processes about constitutive behavior of fractured rocks.

## *Agradecimientos*

*Gracias Dios por siempre guiarme por el camino correcto y por aquellos misteriosos momentos en las etapas mas duras de mi vida cuando realmente siento tu esencia en mi alma y me das la fuerza para salir adelante. Gracias por todas las maravillosas personas que has puesto en mi camino para lograr este sueño.*

*Gracias Mama y Papa por su gran amor. Mama gracias por el trabajo y sacrificio que realizaste para mi formación y por tu gran ejemplo de vida. Son mis ángeles en el cielo que siempre están conmigo y tengo esperanza que en algún momento del tiempo infinito nos volveremos a reunir.*

*Gracias Li por tu amor y apoyo incondicional. Eres el amor de mi vida y el anhelo de mi corazón. Gracias por tu paciencia infinita y por llevarme de la mano por un camino de felicidad y confianza.*

*Gracias Víctor, mi querido hermano, por tus consejos y tus cuidados en los momentos más difíciles.*

*Gracias Dr. Fernando por su guía y apoyo incondicional para la realización de mi doctorado. Gracias por abrir las puertas del Laboratorio de Rocas Fracturadas a mi libre pensamiento en donde conocí algo tan bello y multidisciplinario como lo es la mecánica de rocas, un verdadero desafío intelectual.*

*Aún recuerdo aquel sueño cuando estaba estudiando la vocacional, de un gigante elipsoide emergiendo lentamente de agua cristalina, sin noción del espacio y el tiempo. Quien podría imaginar en aquellos años, que representaba ese sueño.*

## List of Symbols

$V_p$	=	Pore volume
$V_o$	=	Oil saturation volume
$V_{op}$	=	Oil displaced produced
$\varphi$	=	Porosity
$\varphi_m$	=	Matrix porosity
$\varphi_f$	=	Fracture porosity
$C_m$	=	Matrix compressibility
$C_f$	=	Fracture compressibility
$k$	=	Permeability
$k_x$	=	Directional permeability in the “x” axis
$k_y$	=	Directional permeability in the “y” axis
$k_z$	=	Directional permeability in the “z” axis
$k_m$	=	Matrix permeability
$k_f$	=	Fracture permeability
$k_{maxt}$	=	Theoretical maximum permeability
$k_{maxr}$	=	Real maximum closing pressure of the pseudo-matrix region
$k_{matrix}$	=	Maximum theoretical permeability of the pseudo-matrix region
$k_{HMAX}$	=	Maximum horizontal permeability
$k_{H90}$	=	Minimum permeability perpendicular to $k_{HMAX}$
$k_v$	=	Vertical permeability

- $k_{df}$  = Directional permeability in the flow direction
- $k_{dp}$  = Directional permeability in the velocity potential gradient vector
- $\bar{\bar{k}}$  = Permeability tensor in the principal axes
- $\bar{\bar{k}}_f$  = Permeability tensor of the fractured region
- $\bar{\bar{k}}_m$  = Permeability tensor of the pseudo-matrix region
- $\bar{\bar{k}}_{pr}$  = Permeability tensor of the primary porosity region
- $k_{330}$  = Directional permeability 330°
- $k_{60}$  = Directional permeability 60°
- $\mu$  = Nitrogen gas viscosity
- $\mu_w$  = Water viscosity
- $\mu_o$  = Oil viscosity
- $\rho_w$  = Water density
- $\rho_o$  = Oil density
- $\sigma$  = Interfacial tension
- $L$  = Length of the core
- $L_c$  = Characteristic length
- $t_c$  = Characteristic time
- $S_{wi}$  = Connate water saturation
- $S_{orw}$  = Residual oil saturation to water
- $S_{org}$  = Residual oil saturation to gas
- $S_{ort}$  = Total residual oil saturation
- $S_{orf}$  = Fracture residual oil saturation



- $S_{orm}$  = Matrix residual oil saturation  
 $\bar{p}$  = Mean pressure  $(p_1 + p_2)/2$   
 $\Delta p$  = Pressure drop between the inlet and the outlet  $(p_1 - p_2)$   
 $p_1$  = Nitrogen gas injection pressure  
 $p_2$  = Outlet Pressure  
 $P_c$  = Confining pressure  
 $P_p$  = Pore pressure  
 $p_{frac}$  = Maximum closing pressure of the fractured vuggy region  
 $p_{maxr}$  = Real maximum closing pressure of the pseudo-matrix region  
 $p_{maxt}$  = Theoretical maximum closing pressure of the pseudo-matrix region  
 $q_1$  = Nitrogen gas volumetric flow rate  
 $S$  = Overburden stress  
 $b$  = Klinkenberg parameter  
 $\alpha$  = One half of the opening angle  $(\theta/2)$   
 $G(\alpha)$  = Geometric correction factor  
 $\beta$  = The acute angle between the Darcy velocity vector and the velocity potential flow gradient vector  
 $\theta$  = Opening angle exposed to nitrogen gas flow  
 $\Pi$  = Dimensionless variable  
 $\vec{v}$  = Velocity vector flow  
 $\Phi$  = Potential velocity flow function  
 $\nabla$  = Nabla operator

# Contents

<b>List of Figures</b>	<b>4</b>
<b>List of Tables</b>	<b>8</b>
<b>1 Introduction</b>	<b>9</b>
1.1 Petrophysics or Geomechanics: A branch of mechanics . . . . .	9
1.2 Experimental design in reservoir engineering . . . . .	10
1.3 Experimental analysis of fractured porous rocks . . . . .	11
1.4 Advantages of whole core fractured rocks samples . . . . .	13
1.5 Thesis overview . . . . .	17
1.6 Industrial application . . . . .	18
<b>2 Petrophysical Classification of Rocks</b>	<b>19</b>
2.1 Rock Type I: Limestone rock with very low porosity and permeability . . . . .	21
2.2 Rock Type II: Compact rock, with low porosity and permeability . . . . .	22
2.3 Rock Type III: Sandstone rock of intermediate consolidation . . . . .	24
2.4 Rock Type IV: Sandstone rock of low consolidation . . . . .	26
2.5 Rock Type V: Fractured rock with low porosity and permeability matrix . . . . .	27
2.6 Rock Type VI: Fractured rock with high porosity and permeability matrix . . . . .	28
2.7 Rock type VII: Rock with triple porosity (matrix, vugs, and fractures) . . . . .	31
2.8 Rock type VIII: Salt rock . . . . .	35
2.9 Rock type IX: Artificial rock . . . . .	37

<i>CONTENTS</i>	2
2.10 Compressibility of rocks . . . . .	39
<b>3 Experimental Permeability Tensor for Fractured Vuggy Carbonate Rocks</b>	<b>40</b>
3.1 Abstract . . . . .	40
3.2 Introduction . . . . .	41
3.3 Research Objectives . . . . .	41
3.4 Background . . . . .	42
3.5 Methodology . . . . .	43
3.6 Experimental methodology . . . . .	45
3.7 Experimental analysis results . . . . .	46
3.8 Linear compaction tendency . . . . .	48
3.9 Vertical permeability . . . . .	52
3.10 Permeability ellipses . . . . .	53
3.11 Permeability experimental results . . . . .	55
3.12 Permeability tensor . . . . .	65
3.12.1 Secondary permeability tensor . . . . .	65
3.12.2 Primary permeability tensor . . . . .	67
3.13 Conclusions . . . . .	68
<b>4 Estimation of Residual Oil Saturation in a Fractured Rock by Scaling Immiscible Displacement</b>	<b>69</b>
4.1 Abstract . . . . .	69
4.2 Introduction . . . . .	70
4.3 Classical scaling techniques . . . . .	71
4.4 Dimensional analysis . . . . .	72
4.5 Inspectional analysis . . . . .	73
4.6 Background . . . . .	74
4.7 Experimental design . . . . .	79
4.8 Experimental methodology . . . . .	81
4.8.1 Sample cutting and trimming . . . . .	82

<i>CONTENTS</i>	3
4.8.2 Core cleaning and drying . . . . .	84
4.8.3 Bulk porosity, effective porosity, compressibility and permeability data	85
4.8.4 Wettability . . . . .	89
4.8.5 Fluids saturation . . . . .	90
4.8.6 Scaling and geomechanical dimensionless time . . . . .	92
4.8.7 First displacement (Residual oil saturation in vuggy-fracture-matrix system) . . . . .	98
4.8.8 Second displacement (Residual oil saturation in the pseudo-matrix system) . . . . .	102
4.8.9 Discretization of the residual oil saturation in the pseudo-matrix and vuggy-fracture system . . . . .	106
4.9 Physical similitude between model and prototype . . . . .	107
4.10 Concluding remarks . . . . .	108
<b>5 General Conclusions</b>	<b>109</b>
<b>Bibliography</b>	<b>111</b>

# List of Figures

1.1	Fractured whole core sample native from naturally fractured oil field from gulf of Mexico. . . . .	11
1.2	The objective of the experimental design is to simulate the behavior of the reservoir at the scale of the rock specimen, in a short scaled time (laboratory scale). . . . .	12
1.3	Comparison of plug type samples with whole core samples. . . . .	13
1.4	Conventional core plugs used in the petroleum industry. . . . .	14
1.5	Experimental time for rock samples (plugs and whole cores) as a function on the volume of the rock. . . . .	15
1.6	Photograph taken with microscope 800 x in a superficial of a fractured rock. . . . .	17
2.1	Conventional rock samples used in the oil and gas industry, with a 12 in ruler reference. . . . .	20
2.2	Rock type I, limestone rock samples (very low permeability and porosity matrix). . . . .	21
2.3	Rock type II, compact full diameter sample 1 (low permeability and porosity). . . . .	22
2.4	Rock type II, compact full diameter sample 2 (low permeability and porosity). . . . .	23
2.5	Rock type II, compact plug core sample 3 (low permeability and porosity). . . . .	23
2.6	Rock type III, full diameter sandstone 1 with intermediate consolidation. . . . .	24
2.7	Rock type III, full diameter sandstone 2 with intermediate consolidation. . . . .	25
2.8	Rock type III, qualitative measurement of contact angle in a thin rock sample. . . . .	25
2.9	Rock type IV, fragmented rock sandstone of low consolidation. Sample 1. . . . .	26

2.10 Rock type IV, sandstone of low consolidation. Sample 2. . . . .	26
2.11 Rock type V, fractured with low matrix porosity and permeability. . . . .	27
2.12 Rock type VI, fractured rock with high porosity and permeability matrix. . . . .	28
2.13 Rock type VI, fractured rock with high porosity and permeability matrix, with irregular and complex geometry. . . . .	29
2.14 Rock type VI, fractured rock with high porosity and permeability matrix, with intense fracturing. . . . .	29
2.15 Rock type VI, fractured rock with high fracturing with natural saturation of native residual oil in fractures and matrix. . . . .	30
2.16 Rock type VI, quantitative measurement of wettability. Convex meniscus with respect to water (preferential wettability to oil) . . . . .	30
2.17 Rock type VII with vugs and intense fracturing. . . . .	31
2.18 Rock type VII, with representative vuggy- fractures-matrix system. . . . .	32
2.19 Rock type VII, with representative vuggy- fracture system, with high permea- bility and porosity in the matrix system. . . . .	32
2.20 Rock type VII, with representative vuggy- fracture system, with intermediate permeability and porosity in the matrix system. Sample A. . . . .	33
2.21 Rock type VII, with representative vuggy- fracture system, with intermediate permeability and porosity in the matrix system. Sample B. . . . .	33
2.22 Rock type VII, with representative vuggy- fracture system, with intermediate permeability and porosity in the matrix system. Sample C. . . . .	34
2.23 Rock type VII, with representative vuggy- fracture system, with intermediate permeability and porosity in the matrix system. Sample D. . . . .	34
2.24 Rock type VIII, salt rock. Cylindrical fragment. . . . .	35
2.25 Rock type VIII, salt rock. Fragment with irregular shape. . . . .	36
2.26 Rock type VIII, salt rock. Cylindrical sample. . . . .	36
2.27 Rock type IX, handmade artificial sandstone rock, homogeneous grain size. . . . .	37
2.28 Rock type IX, handmade artificial sandstone rock, variable grain size. . . . .	38
2.29 Rock type IX, Crystal spheres to simulate artificial porous media. . . . .	38

3.1	Experimental measurement of horizontal directional permeability in fractured vuggy rock (whole core), every 30° along 360° . . . . .	44
3.2	Schematic diagram of the experimental system used to measure the directional permeability in the whole rock sample. . . . .	45
3.3	Geometric factor for transverse permeability calculation . . . . .	47
3.4	Directional permeabilities as a function of confining pressure in the interval 500-7000 psi. . . . .	48
3.5	Permeability tendency as a function of confining pressure. . . . .	50
3.6	Linear permeability plot for 120° directional permeability. . . . .	51
3.7	Vertical permeability as a confining pressure function. . . . .	52
3.8	Relationship between the Darcy velocity vector flow and the velocity potential gradient vector in porous rocks. . . . .	53
3.9	Directional permeabilities measured at a confining pressure of 500 psi. . . . .	55
3.10	Directional permeabilities measured in the confining pressure range of 500 -7000 psi. . . . .	56
3.11	Directional permeabilities measured at a confining pressure of 500 psi. Ellipse of permeabilities in the direction of flow. . . . .	57
3.12	Directional permeabilities measured in the confining pressure range of 500 -7000 psi. Ellipse of permeabilities in the direction of flow. . . . .	58
3.13	Compaction tendency of the primary permeability in a pressure range of 500-3000 psi. . . . .	59
3.14	Compaction tendency of primary permeability in a pressure range of 3000 -7000 psi. . . . .	60
3.15	Comparison of secondary permeability ellipse and primary permeability ellipse, at confining pressures of 500 psi and 7000 psi. . . . .	61
3.16	Primary and secondary permeability ellipses in terms of $1/\sqrt{k}$ , at a confining pressure of 500 psi in the direction of the velocity potential gradient. . . . .	62
3.17	Primary and secondary permeability ellipses of $1/\sqrt{k}$ , at a confining pressure of 7000 psi in the direction of the velocity potential gradient. . . . .	63

3.18 Principal horizontal permeability axes tendency. . . . .	64
4.1 Schematic representation of mathematical and physical scaling of a naturally fractured reservoir (prototype) and fractured whole rock (model). . . . .	70
4.2 Comparative diagram between dimensional and inspectional analysis. . . . .	73
4.3 Complete scaled experimental displacement for estimating residual oil saturation in a secondary porosity whole core sample. . . . .	80
4.4 Distribution of residual oil saturation in full diameter fractured rock. . . . .	81
4.5 Cut sections of the core selected. . . . .	82
4.6 Full diameter sample A-1. . . . .	83
4.7 Cleaning of a full diameter sample for an average of 30 days. . . . .	84
4.8 Effective porosity as a function of confining pressure, sample A-1. . . . .	87
4.9 Permeability as a function of confining pressure, sample A-1. . . . .	88
4.10 Wettability behavior of the thin section rock extracted from sample A-1. . . . .	89
4.11 Assembly for core mounting in the high-pressure vessel. . . . .	90
4.12 High-pressure and high temperature permeameter, for full diameter samples. . . . .	91
4.13 First displacement, production of fluids in the sample A-1. . . . .	100
4.14 First displacement, oil recovered in the sample A-1. . . . .	100
4.15 Second displacement, production of fluids in the sample A-1. . . . .	103
4.16 Second displacement, oil recovered in the sample A-1. . . . .	104



# List of Tables

2.1	Operational effective stress and compressibility for the different types of rocks.	39
4.1	Dimensions and weight of the full diameter samples.	83
4.2	Total bulk porosity of the full diameter sample A-1.	85
4.3	Effective porosity of the sample A-1.	86
4.4	Compressibility of the sample A1.	86
4.5	Principal values of permeability of the sample A-1.	88
4.6	Experimental value of connate water after a mechanical forced imbibition by reservoir A oil.	91
4.7	Characteristics of the model (core) and the prototype (reservoir).	95
4.8	Oil-water contact of field A.	95
4.9	Representative characteristic lengths for reservoir scale.	96
4.10	Values of stresses for the reservoir at depth of 1900 m.	97
4.11	Values of stresses for the core at laboratory scale.	97
4.12	Characteristic times and velocities for the core displacements.	98
4.13	Data of produced fluids during the first displacement in the sample A-1.	99
4.14	First displacement. Residual oil saturation in the sample A- 1.	101
4.15	Data of produced fluids during the second displacement in the sample A- 1, under an effective stress of 3000 psi.	102
4.16	Second displacement. Residual oil saturation in the sample A-1.	105
4.17	Distribution of residual oil saturation in the full diameter sample A-1.	106
4.18	Comparison of the dimensionless number between model and prototype.	107

# Chapter 1

## Introduction

### 1.1 Petrophysics or Geomechanics: A branch of mechanics

In the petroleum industry, petrophysics is considered on a laboratory scale as a set of standard experiments to be carried out in natural or artificial homogeneous rocks, such tests are applied as routine procedures. Rock mechanics studies stress-strain problems in the rock without considering the effects of fluid flow within the rock. Conventional fluid dynamics theory in porous media does not consider stress and mechanical deformation. The bridge between both theories is given by the effective stress (relation between fluid pressures and mechanical stresses), this concept is of vital importance in many engineering applications.

Due to the immense complexity and discontinuous nature of rocks, it is necessary to define petrophysics as applied science, based on the fundamental principles of mechanics, that implies analyzing from a unified point of view coupled mechanical conditions of stress-strain, the flow of fluids, convective and conductive transport of heat (thermo-hydro-mechanical stresses), chemical processes, dissolution and precipitation of minerals (Stephansson et al. (1996)).

## **1.2 Experimental design in reservoir engineering**

The prediction of reservoir performance can be realized with physical and mathematical models. The principal features of both mathematical and physical models are next presented.

### **a) Physical models**

This type of models allows visualizing the effects of the different factors that influence the production of hydrocarbons. This knowledge usually contributes to the improvement in the computational programs (simulators) used to adjust and predict the reservoir behavior. Sometimes the laboratory experiments (whole core, plugs) of the reservoir performance, permit the identification (inference) of some effects that govern the production of hydrocarbons. Such types of physical effects can be modeled and implemented in reservoir simulation software.

### **a) Mathematical models**

These types of representations are composed of nonlinear partial differential equations, with initial and boundary conditions, which describe the flow of fluids (hydrocarbons and water) in the porous medium.

The non-linearity of the equations that describe the flow in petroleum reservoirs, coupled with the irregular and complex geometry of the flow domain, result in computational mathematical (discrete) models with numerical solutions.

In the literature, some articles compared the predictions by physical and mathematical models at the reservoir scale, frequently concluding that the predictions realized with physical models are the best approximation to real behavior.

### 1.3 Experimental analysis of fractured porous rocks

The experimental design of models for laboratory scale representation of naturally fractured reservoirs aims to predict properties and flow behavior of fluids at the reservoir scale, which develops over a period of several years. The study of fractured vuggy porous rocks presents conceptual and experimental challenges due to the complex morphology of the rock (Fig. 1.1). Experimental studies in the literature are scarce in fractured rocks and in most publications, sandstone samples, Helle Shaw models, and synthetic prototypes are used. In addition to the conventional determinations made on homogeneous matrix-type rocks (rocks where the fractures reside), it is necessary to determine the properties of the secondary porosity (vugular cavities and fractures) in the reservoir and the changes with depth and compaction, which generates a mechanical tendency to close the fractures (specially those oriented in the horizontal direction).



**Fig. 1.1:** Fractured whole core sample native from naturally fractured oil field from gulf of Mexico.

The challenge for the realization of experiments at the laboratory scale consists of studying and simulating the behavior of the prototype (reservoir scale) in a reasonable period of time in the laboratory scale with field conditions (high pressure, temperature, real and native fluids (oil and water), effective stress) in a reduced size model (core specimen).

It is considered that the prototype (giant naturally fractured reservoir of Gulf of Mexico) is extremely heterogeneous and has multiple structures formed by units with similar mechanical and petrophysical properties; The unit of small scale compared with that of the prototype is considered an element of the prototype. The fractured full diameter samples for laboratory studies are elements of the reservoir (plugs and whole core samples)(Fig. 1.2). The design of experiments usually requires the application of advanced scaling techniques (Chapter 4) for the correct development of the process and the interpretation of the obtained test data.

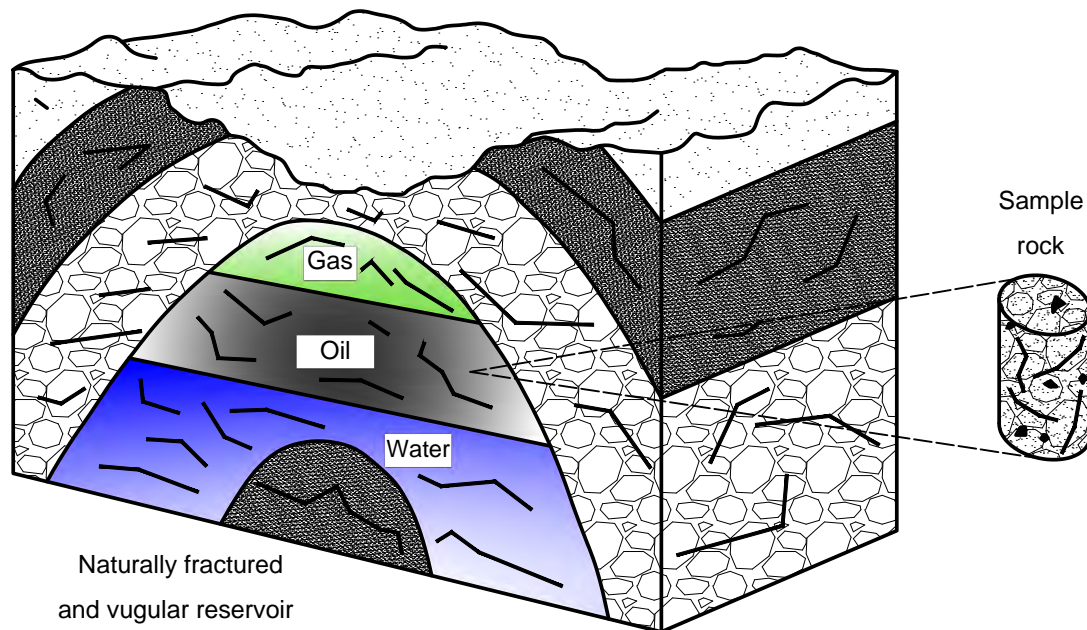


**Fig. 1.2:** The objective of the experimental design is to simulate the behavior of the reservoir at the scale of the rock specimen, in a short scaled time (laboratory scale).

## 1.4 Advantages of whole core fractured rocks samples

The whole core sample analysis is important for the understanding of the complex physical behavior derived from the double porosity of naturally fractured reservoirs at the field scale. Measurements in these types of rocks are essential to study the basic and special petrophysical properties, such as directional permeability, porosity, relative permeabilities, capillary pressures, compressibility, wettability, and fluid saturation in fractures and matrix regions.

In Fig. 1.3 is possible to observe the qualitative differences between plugs and fractured full diameter samples. The complex properties of these rocks like double compressibility and ductility under high pressure and temperature permits the realization of advanced experimental test. However, the risk of destroying the rock in the experiment development is very high, resulting in a significant increment in the economic cost and a waste of time on the project.



**Fig. 1.3:** Comparison of plug type samples with whole core samples.

The analysis of representative fractured rocks let it interpreting the behavior of the naturally fractured reservoir under study, due to its own characteristics of heterogeneity and anisotropy distinctive of the secondary porosity (vuggy-fracture region). The physical process of flow and deformation can be simulated under variable conditions in these types of rocks.

In conventional laboratories, experiments are performed on typical plugs, with conventional dimensions of 1" - 2" in diameter and 2" to 5 "in length, which are small and homogeneous (only matrix porosity), and do not allow the understanding of the fundamental physical mechanisms (multiphase flow in deformable porous media) for predicting the behavior of fractured reservoirs. The conventional tests in plugs are limited and suitable in the case of sandstone reservoirs. usually, the plugs are extracted from long naturally fractured cores, however, only the samples obtained from the matrix portion are tested (Fig. 1.4).



**Fig. 1.4:** Conventional core plugs used in the petroleum industry.

However, the experimental time increases exponentially depending on the volume of the sample rock (Fig. 1.5). The long experimentation time should be considered as an investment of time and resources, with the objective of a deep and representative characterization of the rock, and valuable information for predicting reservoir performance with potential economic benefits. Furthermore, a combination of theoretical, numerical, and experimental analysis must be applied in the interpretation of the data, in order to establish new experimental methodologies and procedures. Experimental results and field data are the key to this process and in order to validate computational simulations (interaction between reservoir-laboratory scale).

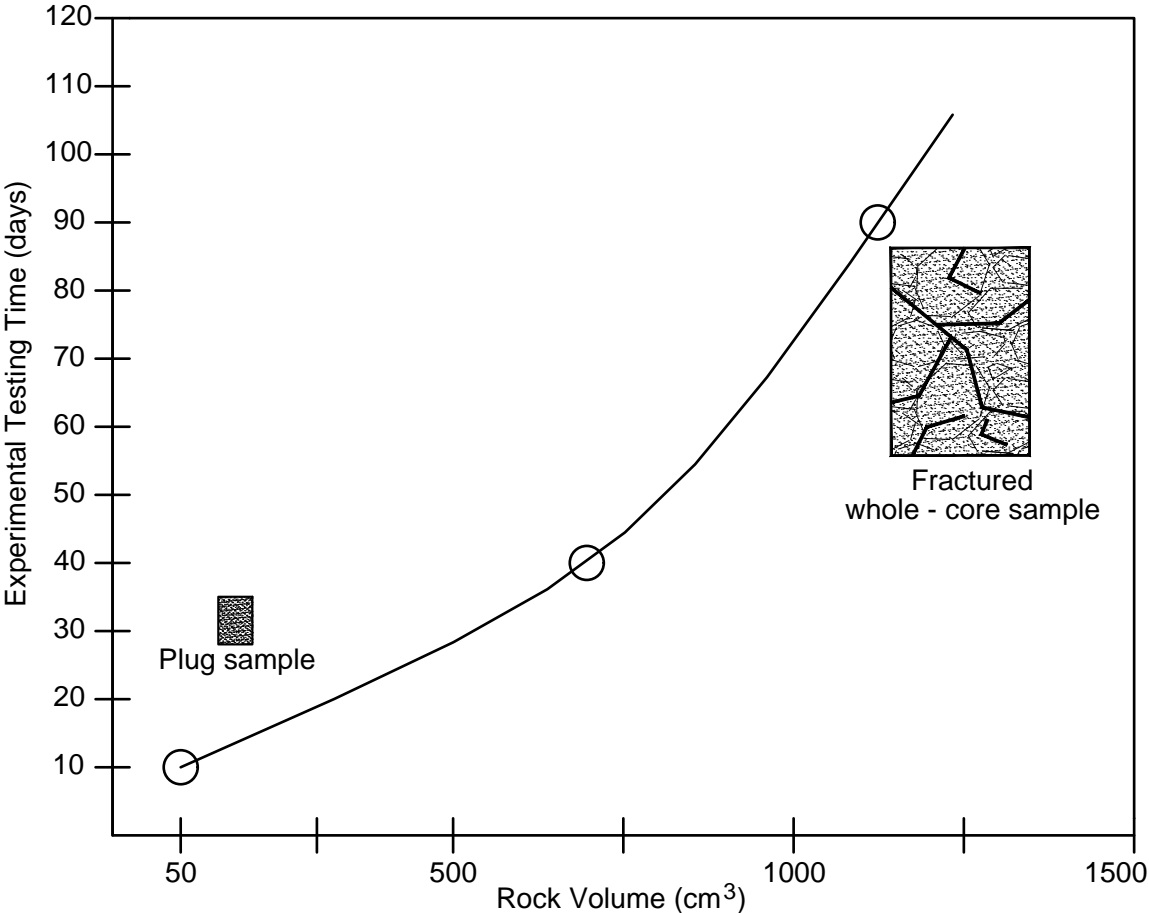


**Fig. 1.5:** Experimental time for rock samples (plugs and whole cores) as a function on the volume of the rock.



Next, updated arguments are presented in relation to Nelson (2001) about the advantages of whole core samples. The most important petrophysical determinations in the characterization of fractured rocks are:

1. Vuggy - fracture permeability (secondary porosity).
2. Matrix permeability and porosity (primary porosity).
3. Directional permeability tensor (secondary and primary porosity).
4. Fluid saturation within vuggy – fracture system.
5. Fluid saturation within matrix system.
6. Matrix to vuggy – fracture system fluid transfer.
7. The recovery factor expected from the matrix – fractures system.
8. The preferential wettability of the rock at reservoir conditions.
9. Compressibility of secondary and primary porosity system.

Whole core samples are useful in naturally fractured reservoir evaluation for three reasons:

1. Due to the larger volume compared to conventional plug type samples, they contain the complex vuggy-fracture system and the matrix system. Therefore, they are more closely physically representative samples of a naturally fractured reservoir.
2. The permeability tensor can be determined at reservoir conditions, with the determination of directional permeabilities. This valuable property permits correcting reservoir simulators software.
3. It is possible to perform a scaling process between laboratory scale and field scale, to develop experiments (displacements) representative of reservoir exploitation conditions.

## 1.5 Thesis overview

This thesis presents new petrophysical methods for obtaining and characterizing physical properties of fractured carbonate rocks and sandstone rocks. The experimental determination of the permeability tensor allows identifying the directional permeabilities of the rock analyzed and the dependence on the effective confining stress. With the principal permeability directions determined, the mayor permeable direction is defined for developing a representative immiscible displacement (water - oil) at reservoir conditions. The experimental utility of the permeability tensor contributes to discretize the values of the properties of the fractures and the matrix system, key aspect for teh estimation of the residual oil saturation in the double porosity system (matrix - fractures), since the morphology of the rock is dependent on the confining pressure.

The design of an immiscible displacement test (gas - oil, water - oil) is presented to determine the residual oil saturation in porous fractured rocks. It is possible to determine the residual oil saturation in the fracture and matrix system of the rock, depending on the effective stress applied to the rock (Fig. 1.6).

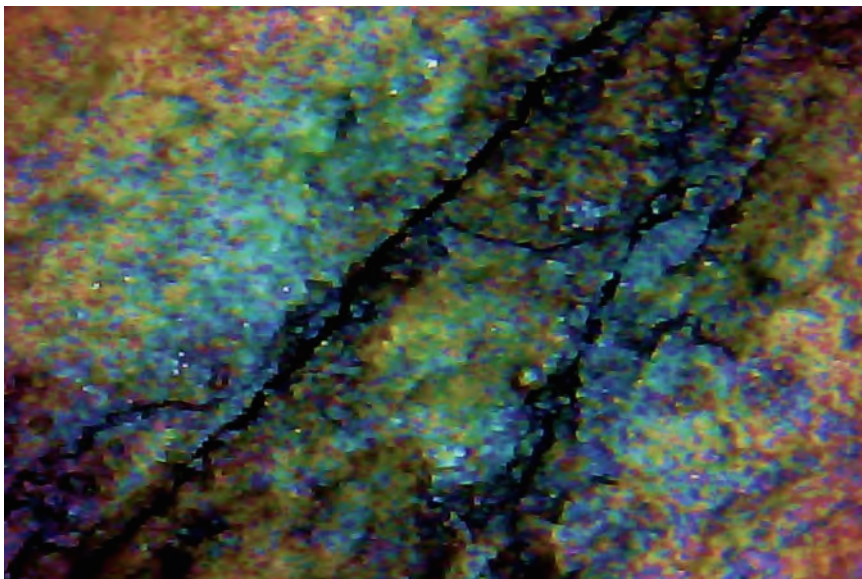


**Fig. 1.6:** Photograph taken with microscope 800 x in a superficial of a fractured rock.

## 1.6 Industrial application

The reserves of oil can be increased based on the discovery of new reservoirs (currently increasingly in more difficult conditions of depth and in the case of marine fields, greater water depth, varying between 500 and 3000 meters), or improving the Recovery Factor. Currently, the average recovery factor of oil at the international level is approximately 35 %, indicating that a considerable amount of the total volume that has been discovered remains in the underground.

That is, the area of opportunity related to the implementation of enhanced oil recovery processes is very important (assuming, that hydrocarbon prices are sufficient to guarantee the profitability of these projects).

The value for residual oil saturation to water  $S_{orw}$ , and to gas  $S_{org}$ , are the most important data for the design and implementation of an enhanced oil recovery process, so it is imperative a reliable estimation. The experimental design procedure exposed in this work allows for obtaining this essential information.

Furthermore, the experimental tests proposed in this work can be easily implemented in routine core analysis offered by conventional labs. The valuable information obtained by the experiments can be applied in the development and validation of advanced mathematical models, that consider the coupled fluid flow with the deformation in fractured porous rocks at high pressure and temperature conditions (reservoir conditions).

## Chapter 2

# Petrophysical Classification of Rocks

The following classification of rocks is based on the petrophysical properties of porosity, permeability, compressibility and experimental effective stress, applied to obtain representative results at reservoir conditions for whole core samples (diameter = 4 in) (high pressure and temperature); the stress condition can be established as a failure criterion for fractured rocks. The classification is based on specialized experimental procedures for full diameter samples, developed in approximately 20 years of experience and operation of Fractured Rocks Laboratory, UNAM.

Additionally, recommendations are established for developing conventional and special petrophysics experimental studies. Defining conventional petrophysics to the set of experiments to determine the physical properties of the rock such as porosity, effective porosity, directional permeability, and compressibility. Special petrophysics can be defined as the set of tests that include single-phase and multi-phase flow in the rock specimen with applied effective stress (compaction), such as, determination of the permeability tensor, wettability at reservoir conditions (USBM test for fractured rocks), determination and discretization of residual oil saturation and flow interaction in the matrix - fracture system. The presented classification can be extended to a reservoir classification, which coincides with other classifications in the literature.

The term “Rock type” is used to describe the major distinguishing features of core material. This can refer to the degree of consolidation, existence of fractures or vugs, composition, or physical properties of the rock. Geological descriptions of rocks are more complex and classification schemes has been devised to categorize specific rock types with respect to texture, type of cementation, grain size, etc., these aspects are not considered in the proposed classification, however, can be easily included (API-RP-40 (1998)).

The plugs should be extracted from the uniform and consolidated sections of whole cores (typically length of 9 m), oriented either vertically or horizontally with respect to the whole core axis or with reference to the normal of the bedding planes. These plugs will provide data on matrix properties. In the following classification, the rock type (plug diameter 2 in) samples shown in (Fig. 2.1), can be considered, depending on their characteristics, as a subset of the various types of rocks presented.



**Fig. 2.1:** Conventional rock samples used in the oil and gas industry, with a 12 in ruler reference.

## 2.1 Rock Type I: Limestone rock with very low porosity and permeability

Consolidated limestone are rocks, with very low porosity and permeability (Fig. 2.2). Physically it can be interpreted as matrix rock. The studies carried out in this type of rock are limited and less representative. The experimental tendency of porosity and permeability is a linear function of overburden stress. These types of rocks present the following characteristics: a) low compaction and therefore low compressibility, b) high overburden stress range can be applied, c) is suitable for rock mechanics studies, and d) preferential intermediate wettability to oil. The risk of failure of the experiments under high pressure and temperature conditions in this rock type is low, due to the consolidation and hardness (result of cementation) properties of the sample. Furthermore, the cutting and trimming operations can be applied without risk of damaging the rock.



**Fig. 2.2:** Rock type I, limestone rock samples (very low permeability and porosity matrix).

## 2.2 Rock Type II: Compact rock, with low porosity and permeability

Compact rock, with low porosity, compressibility and permeability properties (Fig. 2.3, Fig. 2.4 and 2.5). Recommended for basic petrophysics studies. It is possible to develop special petrophysics studies at low effective stress conditions (confining pressure < 2000 psi). This rock can be considered as homogeneous isotropic or anisotropic rock. Suitable for studies of rock mechanics with high applied stress and temperature conditions. It is possible to study horizontal directional permeabilities; regularly, these types of rocks have a greater horizontal permeability compared to vertical permeability,  $k_{horizontal} > k_{vertical}$ . Preferential intermediate wettability to water.

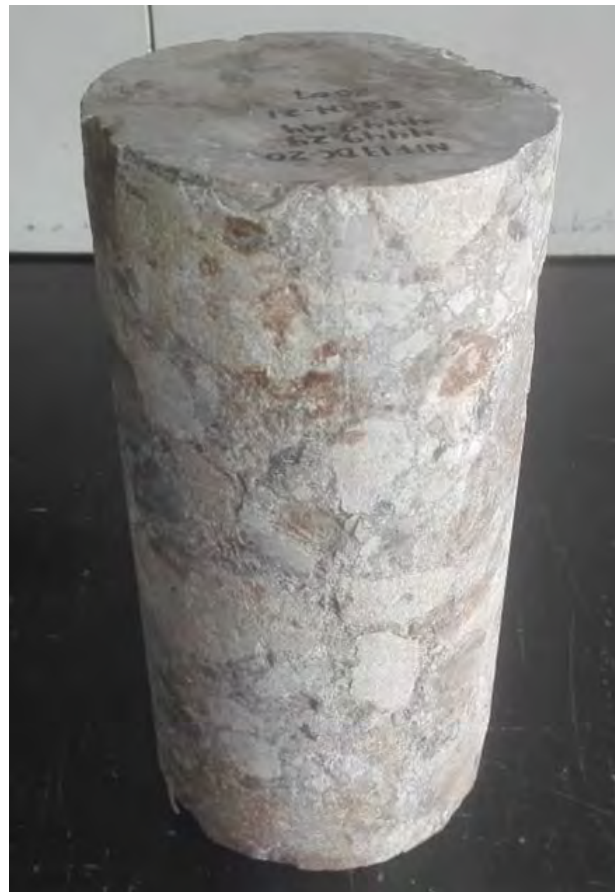


**Fig. 2.3:** Rock type II, compact full diameter sample 1 (low permeability and porosity).



**Fig. 2.4:** Rock type II, compact full diameter sample 2 (low permeability and porosity).

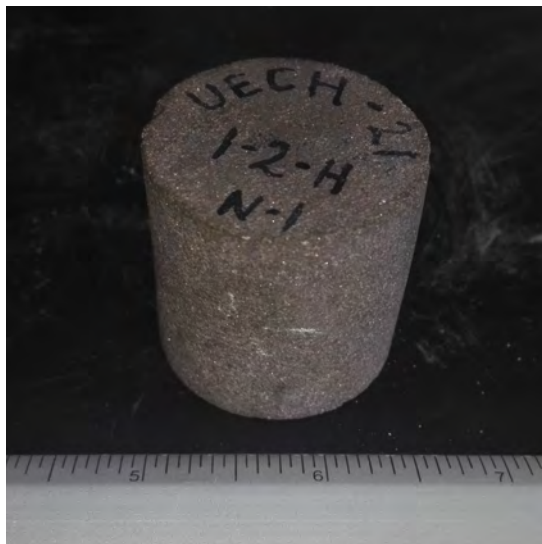


**Fig. 2.5:** Rock type II, compact plug core sample 3 (low permeability and porosity).



## 2.3 Rock Type III: Sandstone rock of intermediate consolidation

Sandstone rock of intermediate consolidation and homogeneous with good porosity properties, effective porosity, permeability, and compressibility (Fig. 2.6, Fig. 2.7 ). Recommended for the complete set of petrophysical studies. Experimental linear compaction tendency of porosity and permeability as a function of effective stress is expected. This type of rocks can resist high overburden pressure (confining pressure) and temperature conditions. Preferential wettability to water (Fig. 2.8). The cleaning, cutting and trimming operations should not physically damage the core. Precautions must be taken from erosion by the drip of clean solvent when utilizing the distillation extraction technique. Sometimes in the realization of displacements, the disintegration of the sandstone can obstruct the internal flow in the rock and the pipelines connected to measurement devices.



**Fig. 2.6:** Rock type III, full diameter sandstone 1 with intermediate consolidation.

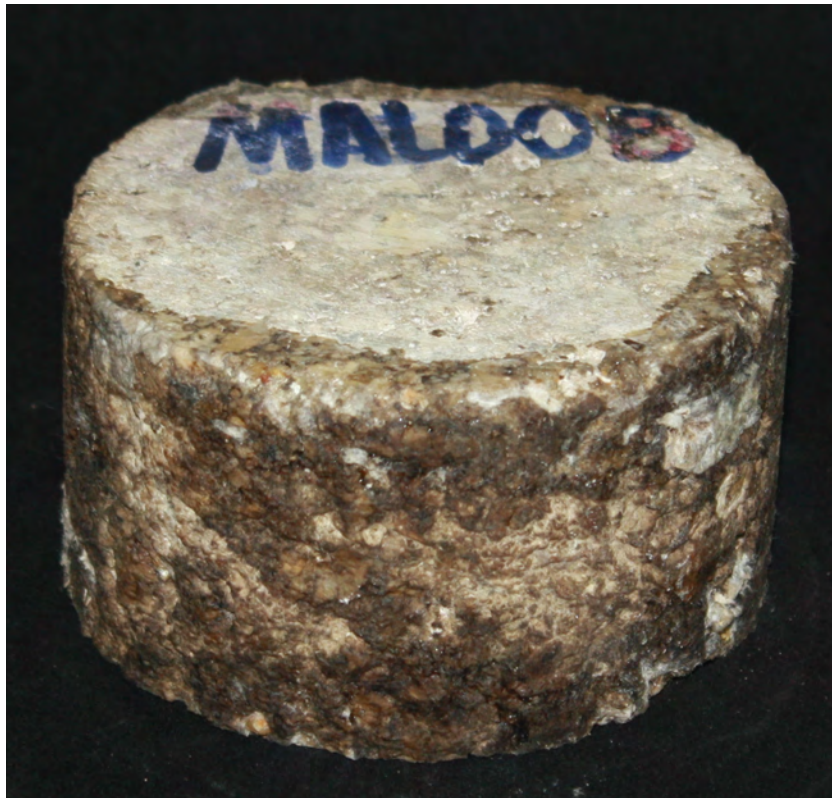


**Fig. 2.7:** Rock type III, full diameter sandstone 2 with intermediate consolidation.

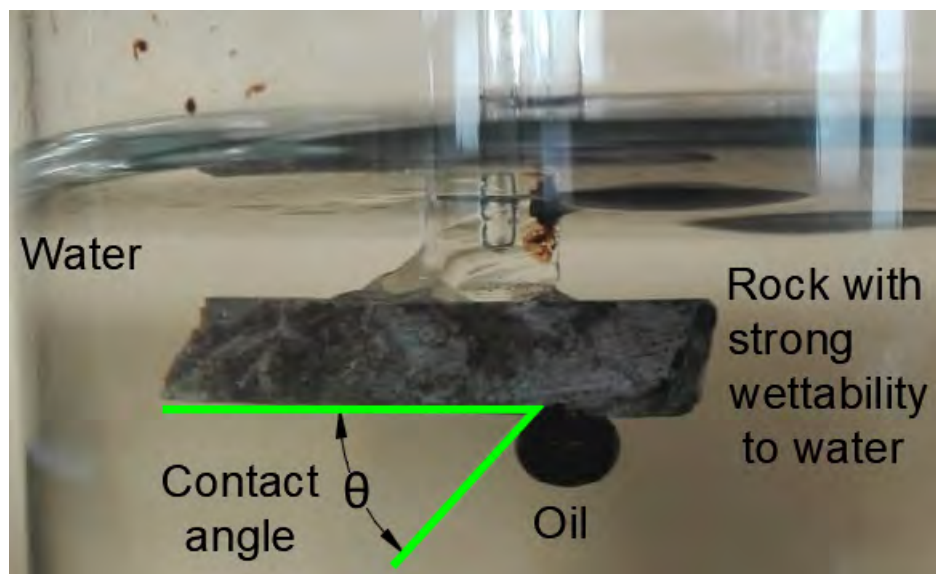


**Fig. 2.8:** Rock type III, qualitative measurement of contact angle in a thin rock sample.

## 2.4 Rock Type IV: Sandstone rock of low consolidation

Sandstone rock of low consolidation and high compressibility. Rock or representative material suitable for basic and special petrophysics studies (Fig. 2.9 and Fig. 2.10). It is possible to operate at very high conditions of effective stress and temperature. Experimental linear decrease of porosity - permeability depending on the stress applied. Strong water wettability. The risk of obstruction of the pipelines connected to measurement devices is high due to the flow of loose sand from the rock, this problem can damage the laboratory equipment.



**Fig. 2.9:** Rock type IV, fragmented rock sandstone of low consolidation. Sample 1.



**Fig. 2.10:** Rock type IV, sandstone of low consolidation. Sample 2.

## 2.5 Rock Type V: Fractured rock with low porosity and permeability matrix

Fractured rock with low porosity and permeability matrix. Heterogeneous and anisotropic rock. This type of rock has double porosity and double permeability behavior (Fig. 2.11). The fractured region provides excellent permeability. Little or no storage capacity in the matrix system. Recommended for basic and special petrophysics studies. Double compressibility characteristic, for matrix and fracture. Operational conditions from low to intermediate range of effective stress applied due to double porosity. If the stress applied to the rock exceeds the failure criteria, natural fractures can propagate throughout the entire rock and the experiment can fail. Ideal for the realization of immiscible and miscible displacements; it is necessary to determine the critical rate of injection for a representative flow in the rock. Strong wettability to the oil due to carbonate (dolomite, limestone) origin.



**Fig. 2.11:** Rock type V, fractured with low matrix porosity and permeability.

## 2.6 Rock Type VI: Fractured rock with high porosity and permeability matrix

Fractured rock with high porosity and permeability matrix. Heterogeneous and anisotropic rock. Recommended for basic and special petrophysics studies (Fig. 2.12, Fig. 2.13, Fig. 2.14 and Fig. 2.15). This type of rocks has a double linear compaction tendency of porosity and permeability depending on the applied effective stress. Also, high storage capacity in the fractured and matrix region. Double compressibility characteristic, high compressibility in the fractured region and low for the matrix region. With high conditions of applied effective stress, the fractured region of high permeability can decrease until it fusion with the matrix permeability and porosity, and reach a pseudo matrix state. Ideal rocks for studies of immiscible and miscible displacement, residual oil saturations in the matrix-fracture system, matrix-fracture transfer. If the stress applied to the rock exceeds the failure criteria, natural fractures can propagate throughout the entire rock and the experiment can fail. The wettability to the oil is due to carbonate origin (Fig. 2.16).



**Fig. 2.12:** Rock type VI, fractured rock with high porosity and permeability matrix.



**Fig. 2.13:** Rock type VI, fractured rock with high porosity and permeability matrix, with irregular and complex geometry.



**Fig. 2.14:** Rock type VI, fractured rock with high porosity and permeability matrix, with intense fracturing.



**Fig. 2.15:** Rock type VI, fractured rock with high fracturing with natural saturation of native residual oil in fractures and matrix.

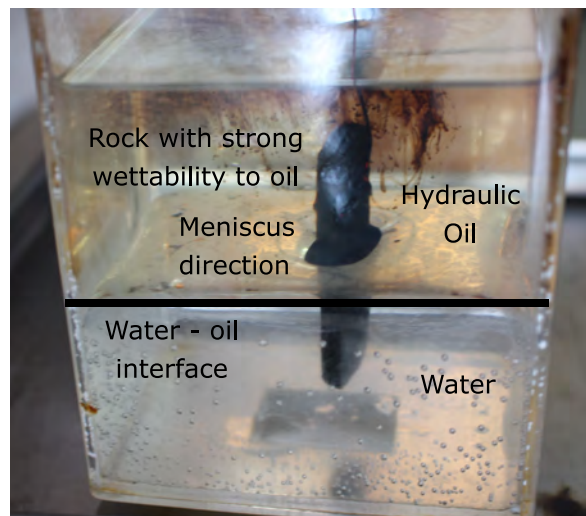


**Fig. 2.16:** Rock type VI, quantitative measurement of wettability. Convex meniscus with respect to water (preferential wettability to oil)

## 2.7 Rock type VII: Rock with triple porosity (matrix, vugs, and fractures)

Rock with triple porosity (matrix, vugs, and fractures). Heterogeneous and anisotropic rock. Recommended for basic and special tests (Fig. 2.17, Fig. 2.18, Fig. 2.19, Fig. 2.20, Fig. 2.21, Fig. 2.22 and Fig. 2.23 ). This type of rocks have a double compaction tendency of porosity and permeability as a function of effective stress. It is possible to analyze a triple compaction behavior for each type of porosity-permeability; however, it is more physically representative and natural the double behavior vuggy-fractures and matrix. The compaction behavior is similar to rock type V. These rocks have great storage and permeability for the flow of fluids, double compressibility, high compressibility for the vuggy - fracture system. Ideal for the realization of immiscible a miscible displacements, measurement of permeability tensor, estimation of residual oil saturation and fluid interaction in the vuggy-fracture- matrix system. Regularly these rocks have a strong wettability to the oil, due to its carbonate (limestone and dolomite) nature. If the stress applied to the rock exceeds the failure criteria, natural vuggy - fractures can propagate throughout the entire rock and the experiment can fail; therefore, the experiments in this type of rocks are developed at intermediate effective stress conditions.



**Fig. 2.17:** Rock type VII with vugs and intense fracturing.





**Fig. 2.18:** Rock type VII, with representative vuggy- fractures-matrix system.



**Fig. 2.19:** Rock type VII, with representative vuggy- fracture system, with high permeability and porosity in the matrix system.



**Fig. 2.20:** Rock type VII, with representative vuggy- fracture system, with intermediate permeability and porosity in the matrix system. Sample A.



**Fig. 2.21:** Rock type VII, with representative vuggy- fracture system, with intermediate permeability and porosity in the matrix system. Sample B.



**Fig. 2.22:** Rock type VII, with representative vuggy- fracture system, with intermediate permeability and porosity in the matrix system. Sample C.



**Fig. 2.23:** Rock type VII, with representative vuggy- fracture system, with intermediate permeability and porosity in the matrix system. Sample D.

## 2.8 Rock type VIII: Salt rock

Drilling and completions in salt formations can be difficult because of the creep behavior that the salt formations exhibit. Creep behavior results from the instability of the salt formation, which causes a slow flow and permanent deformations. The constant creep causes an excess stress on the wellbore casing, which may eventually cause the casing to collapse (Wang and Samuel (2016)). Scaling this phenomenon in laboratory scale can contribute to predict and mitigate the severity of salt mobility and reduce the risks of casing collapse. Salt rock samples, are used for triaxial testing and obtaining static modules (Young modulus, Poisson ratio, axial stress vs strain, etc.). It is advisable to develop experiments in this type of rocks at reservoir conditions (pressure and temperature) to perform creep and strain tests. It does not apply to basic and special petrophysical studies (Fig. 2.24, Fig. 2.25 and Fig. 2.26). The experimental data can be used for the construction and validation of numerical predictive constitutive model for creep deformation at the reservoir scale.



**Fig. 2.24:** Rock type VIII, salt rock. Cylindrical fragment.



**Fig. 2.25:** Rock type VIII, salt rock. Fragment with irregular shape.



**Fig. 2.26:** Rock type VIII, salt rock. Cylindrical sample.

## 2.9 Rock type IX: Artificial rock

Artificial formed porous media. This type of rock arrangement can be formed by sand and rock fragments, to simulate homogeneous porous media (classic in the petroleum industry), or heterogeneous and fractured rocks. It is possible to simulate multiple regions of porosity and permeability. Based on saturation aging techniques it is possible to establish a preferential wettability (oil or water) tendency of the medium. High operational conditions of applied effective stress can be used. The classic arrangements with sand and glass spheres, Hele-Shaw models and synthetic 3D printed rocks, operated at variable conditions of pressure and temperature, can be included in this type of rocks.

Fig. 2.27 and Fig. 2.28, show handmade plugs elaborated from loose sand. Conventional and special petrophysical experiments can be developed with these samples (Fig. 2.29). These simulate the behavior of sandstone rock.



**Fig. 2.27:** Rock type IX, handmade artificial sandstone rock, homogeneous grain size.



**Fig. 2.28:** Rock type IX, handmade artificial sandstone rock, variable grain size.

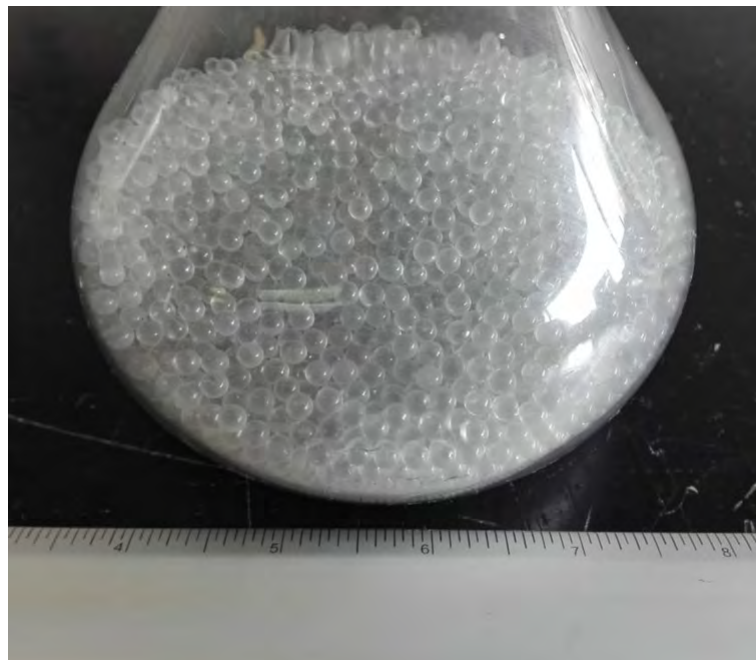


**Fig. 2.29:** Rock type IX, Crystal spheres to simulate artificial porous media.

## 2.10 Compressibility of rocks

Table. 2.1, shows the data of effective stress or overburden pressure applied to each type of rock. Average operational limits are established for each sample. The pressure range indicates the operational effective stress at which the representative results of the basic and special petrophysics studies can be obtained. In addition, the upper limits in pressure establish the empirical failure criteria for developing the experiments in order to prevent the propagation of fractures induced by the overburden pressure. The rock type VIII does not include because it is not typical for petrophysical studies.

The operational limits and the compressibility values must be employed with caution and according to the desired experimental result and the measured physical properties. The reported compressibility range are hard data for numerical reservoir simulation and rock mechanics studies.

**Table 2.1:** Operational effective stress and compressibility for the different types of rocks.

Rock Type	Operational Effective Stress (Representative petrophysical measurement)	Average Compressibility (psi) <sup>-1</sup>	
		Primary (matrix)	Secondary (Vuggy - fractures)
I	0 psi < $p$ < 3000 psi	< 1.00 x 10 <sup>-6</sup>	-----
II	0 psi < $p$ < 6000 psi	3.00 - 5.00 x 10 <sup>-6</sup>	-----
III	0 psi < $p$ < 20000 psi	40.00 - 70.00 x 10 <sup>-6</sup>	-----
IV	0 psi < $p$ < 20000 psi	70.00 - 120.00 x 10 <sup>-6</sup>	-----
V	0 psi < $p$ < 7000 psi	10.00 - 20.00 x 10 <sup>-6</sup>	80.00 - 100.00 x 10 <sup>-6</sup>
VI	0 psi < $p$ < 7000 psi	20.00 - 50.00 x 10 <sup>-6</sup>	175.00 - 200.00 x 10 <sup>-6</sup>
VII	0 psi < $p$ < 7000 psi	50.00 - 100.00 x 10 <sup>-6</sup>	200.00 - 400.00 x 10 <sup>-6</sup>
IX	0 psi < $p$ < variable superior limit	Function of the physical properties of the material	



# Chapter 3

## Experimental Permeability Tensor for Fractured Vuggy Carbonate Rocks

### 3.1 Abstract

This paper presents a novel petrophysical experiment for measuring the 3D permeability tensor at reservoir conditions in a fractured vuggy carbonate rock. The permeability variation with confining pressure is demonstrated through the experimental investigation; the permeability ellipses plots show the decrease of permeability, as a function of the increase in effective stress. The experiment was developed at reservoir conditions (120°C temperature and variable confining pressure) in a native whole rock sample, from a Gulf of Mexico naturally fractured and vuggy reservoir. The analysis of the laboratory data reveals the elliptical behavior of permeability. Two ellipses were generated, one corresponding to the secondary porosity system and another for the matrix system. An important result is the compaction of the secondary porosity ellipse, until it fusion with the primary porosity ellipse at a high confining pressure state. The test contributes to the understanding of the mechanical and flow aspects of permeability, for naturally fractured reservoirs. The experimental results provide a basis for improving reservoir simulation studies, to obtain realistic predictions of reservoir behavior.

## 3.2 Introduction

On a laboratory scale, the existing petrophysical characterization methods are applicable to homogeneous samples (plugs), packings of rock fragments and sand. Several researchers simulate fractures and irregularities, of a fractured medium by experimental arrangements of well-defined fracture sets. The above is done experimentally and with computational methods.

The experiment was developed at reservoir conditions (120°C temperature and variable confining pressure) in a native double porosity rock from Gulf of Mexico reservoir. The analysis of the laboratory results show the elliptical nature of the permeability.

Two ellipses are generated, one corresponding to the secondary porosity system and another for the matrix system. An important result is the compaction of the secondary porosity ellipse until it fusion with the primary porosity ellipse at a high confining pressure.

## 3.3 Research Objectives

To design a new petrophysical test for measurement the 3D permeability tensor, at reservoir conditions. Find the principal values of the 3D permeability tensor for anysotropic fractured rock. Demonstrate the behavior of the decrease in permeability as the applied effective stress increases, on the elliptic permeability graphs at various stress states. To establish the advantages of the linear compaction model of [Herrera \(2000\)](#) compared with the model of [Gangi \(1978\)](#). Contribute to the understanding of the flow of fluids in fractured media.

To establish the advantages of the linear compaction model of [Herrera \(2000\)](#) compared with the model of [Gangi \(1978\)](#). Contribute to the understanding of the flow of fluids in fractured media.

### 3.4 Background

There are several studies in the literature that reflect the interest in the characterization of fractured media at a laboratory scale. The main features of the fractured rocks are the heterogeneity and anisotropy caused by the diagenetic processes, in comparison with the sandstone rocks that have uniform properties. There are several works that describe the importance of the determination of directional permeabilities.

Sheidegger (1954, 1956) derived the permeability tensor theory by interpreting experimental data from the literature. These data were interpreted by permeability ellipses plots. The procedure described in the article is of practical application on the laboratory scale, since it allows to calculate the direction and the principal values of the permeability tensor. A valuable contribution is polar plotting  $k^{-1/2}$  depending on the angles of measurement.

The compaction effects in the permeability allow a detailed study of the petrophysical effects due to the effective stress applied. The most important effect is the permeability reduction in fractured vuggy reservoirs. Gangi (1978) established a model based on the asperities contained in the fracture planes. The obtained model is power law, which considers the variation of confining pressure, fits the experimental data in the literature for fractured carbonate rocks. The Gangi model predicts the behavior of the decrease in permeability as a function of the confining pressure, continuously in a pressure interval. However, it does not distinguish the qualitative characteristics of the rock, such as permeability in the fracture system and the transition to a pseudo-matrix stage.

Leung (1986), studied the effects of the crossed terms of the permeability tensor and the limitations when not considering them in the simulators. The results can lead to errors in the prediction of well-production response at the field scale.

Herrera (2000) proposed an interpretation method for the reduction of permeability in fractured rocks as a function of the confining pressure, which allows distinguishing the permeability of the fracture system and the permeability of the matrix as the effective stress increases, by means of two matching lines, one corresponding to each mechanical state. The fundamental principle is to start the increase in stress, from a minimum value (500 psi), which allows the fractures to be mainly open. However, this work only proposed the experimental procedure and qualitative interpretation of the results.

Lei et al. (2015) presented an excellent permeability tensor literature review. Through the combination of numerical simulation results and experiments performed in artificial fractured media, they obtained a 2D permeability tensor. Furthermore, a mathematical model of the 3D permeability tensor is derived, based on the stress-dependent permeability model of Gangi (1978).

### 3.5 Methodology

A new experimental method applicable to fractured vuggy rocks and sandstone is proposed, which is carried out at reservoir conditions, in order to get the 3D permeability tensor, considering the influence of the confining pressure or effective stress applied to the rock. According to the elliptical nature of the permeability, the behavior of the permeability tensor is described with the linear stress permeability model, which has advantages compared to that of Gangi (1978). The following methodology was designed:

- Measurement of horizontal directional permeability in fractured vuggy rock (whole core) every 30° along 360°. Horizontal directional permeability is measured for each angle (12 directions). Directional horizontal permeability is measured for each angle (12 directions). For each direction, ten nitrogen gas flow measurements are made. The experimental scheme is shown in Fig. 3.1.

- Determination of vertical permeability with nitrogen gas flow.
- Each permeability measurement was performed at the following confining pressure sequence, 500 psi, 1000 psi, 2000 psi, 3000 psi, 4000 psi, 5000 psi, 6000 psi, 7000 psi, and determination of directional permeability based on the conformal transformation method of [Collins \(1952\)](#).
- Generation of permeability ellipses for each confining pressure state.
- Fitting of the experimental permeability data according to the confining pressure for each directional measurement, with the linear model of [Herrera \(2000\)](#), which describes the characteristics of the matrix-fracture system.
- Graphical analysis of the decrease in the permeability ellipse as the confining pressure increases and description by the permeability stress linear model.

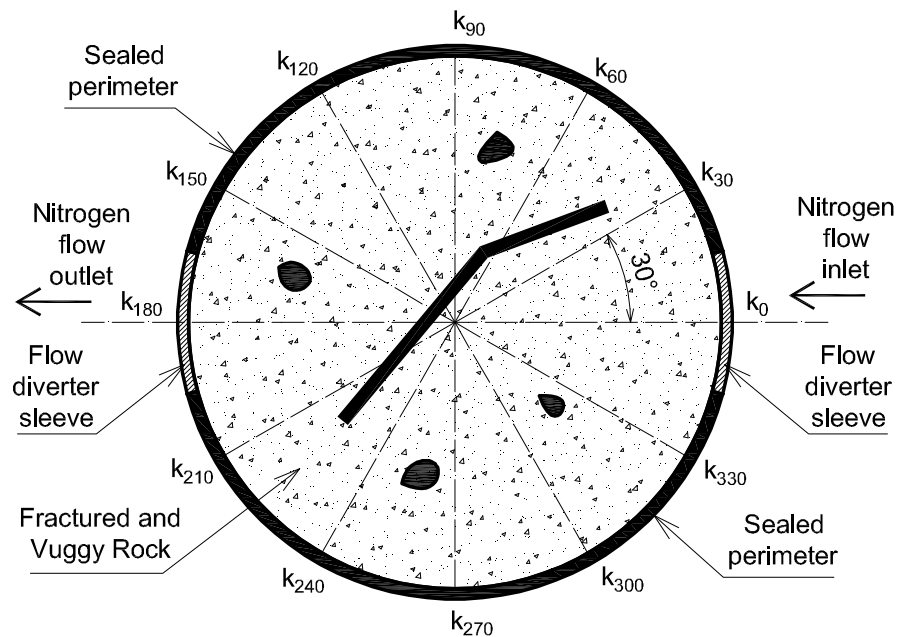


**Fig. 3.1:** Experimental measurement of horizontal directional permeability in fractured vuggy rock (whole core), every 30° along 360°.

### 3.6 Experimental methodology

A fractured vuggy cylindrical whole core of the Gulf of Mexico naturally fractured reservoir was used, with a diameter of 4 inches and a length of 4.40 inches. The test was conducted in a pressure vessel filled with a pressurized fluid, with an operational capacity of 20, 000 psi and 150 °C. The pressure of the fluid is the confining pressure (uniform hydrostatic stress), measured by a manual pressure gauge. The specimen was covered with an impermeable rubber sleeve and upper and bottom end-caps with pore fluid port. Additionally, a flow diverter sleeve was implemented for redirecting the nitrogen gas flow to a horizontal direction (Fig. 3.2) . The experimental design is based on the proposed by Peters (2012).

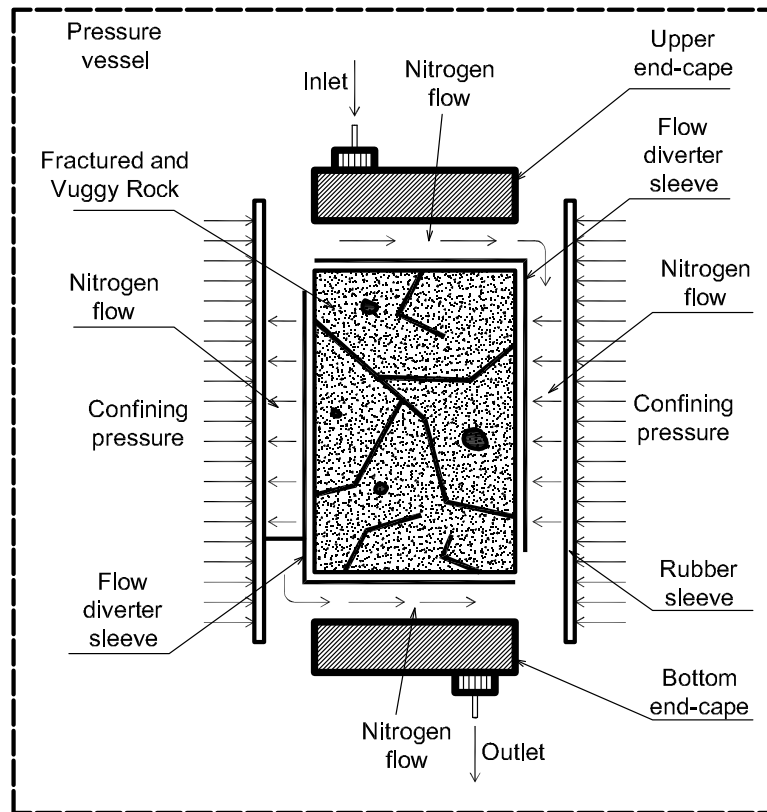


**Fig. 3.2:** Schematic diagram of the experimental system used to measure the directional permeability in the whole rock sample.

The first step was to identify a reference axis on the rock surface to establish the direction of 0° -180°. The confining pressure was increased to a value of 500 psi, considering a stabilization time before the measurement of permeability with nitrogen gas flow. With the permeability measurement developed in the direction of 0° to 180°, the connections are exchanged to reverse the gas flow in the direction of 180° to 0°. Next, with the two directions of permeability tested, the confining pressure is increased to 1000 psi, waiting the adequate stabilization time. The existing connection in the direction of 180°to 0° was used, and the measurement is carried out. The test continued with the inversion of the gas flow and the corresponding measurements from 0° to 180°.

The procedure described was repeated in increments of 1000 psi until reaching 7000 psi of confining pressure. The inlet pressure, the outlet pressure, and the volumetric outlet flow were measured for each confining pressure state. Once a permeability direction was made, for example, direction 0° - 180°, the sample is removed from the pressure vessel, unpacked in order to rotate the flow diverter sleeve to the direction of 30° - 210°. The sample was prepared for a new direction test, and the above procedure described was repeated, until covering the 360° at 30° intervals.

### 3.7 Experimental analysis results

The permeability ellipse determination for a whole fractured vuggy rock sample was obtained from the measurement of the transverse directional permeabilities of the specimen. Through the experimental procedure described directional horizontal permeabilities were measured. The Collins (1952) formula was applied to calculate the transversal directional permeability values, measured with nitrogen gas flow (in Darcy units).

The formula was derived by conformal mapping method:

$$k = \frac{p_1 q_1 \mu}{2\bar{p}L(1 + \frac{b}{\bar{p}})\Delta p} G(\alpha) \quad (3.1)$$

Where  $p_1$  is the inlet pressure,  $q_1$  is the volumetric flow measured at  $p_1$ ,  $\bar{p}$  is the mean pressure  $(p_1 + p_2)/2$ ,  $\Delta p$  is the pressure drop between the inlet and the outlet  $(p_1 + p_2)$ ,  $b$  is the Klinkenberg parameter,  $L$  is the height of the core,  $\theta$  is the opening angle exposed to nitrogen gas flow,  $\alpha$  is equal to  $\theta/2$ , in this case  $\theta = 30^\circ$ ,  $G(\alpha)$  is a geometric correction factor to account for the complex flow geometry of the gas from inlet to outlet.

The Fig. 3.3 shows the plot of  $G(\alpha)$  versus  $\alpha$  from Collins (1952). The results analyzed from the directional permeability experiments are shown in the following graphs.

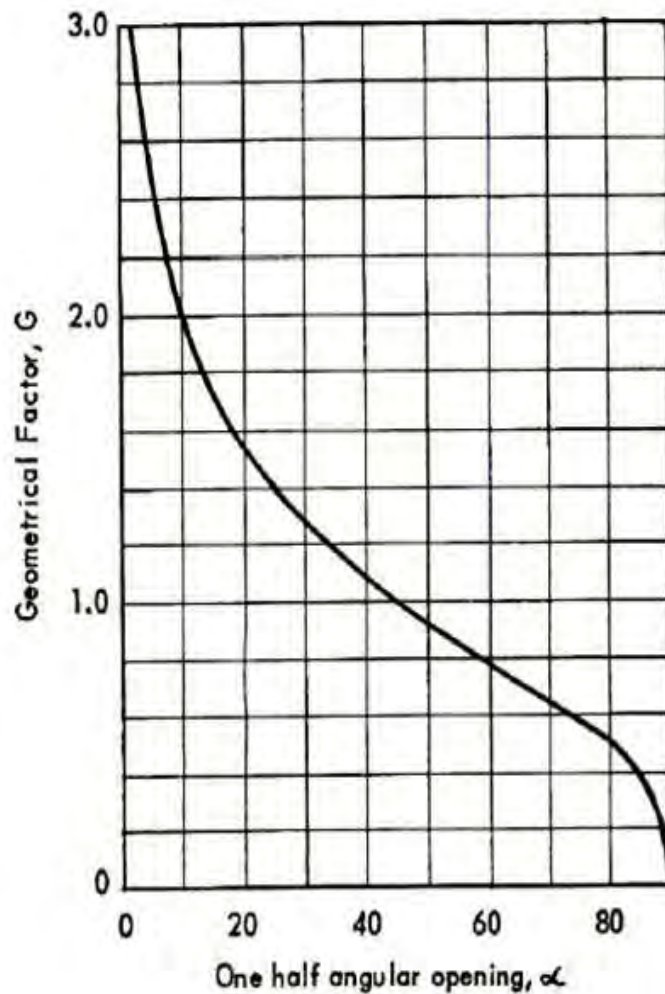


**Fig. 3.3:** Geometric factor for transverse permeability calculation



### 3.8 Linear compaction tendency

The Fig. 3.4 shows the obtained results for the horizontal directional permeabilities as a function of the confining pressure, in relation to the respective angles. The permeability decrease is clearly observed as the confining pressure increases. The directions of 30° - 210° and 150° - 330° show lower values compared to those obtained for the other directions. The transition of the straight lines occurs approximately at a confining pressure of 3000 psi, a change that occurs in the 0°, 60°, 90°, 120°, 180°, 240°, 270°, and 300° directions.

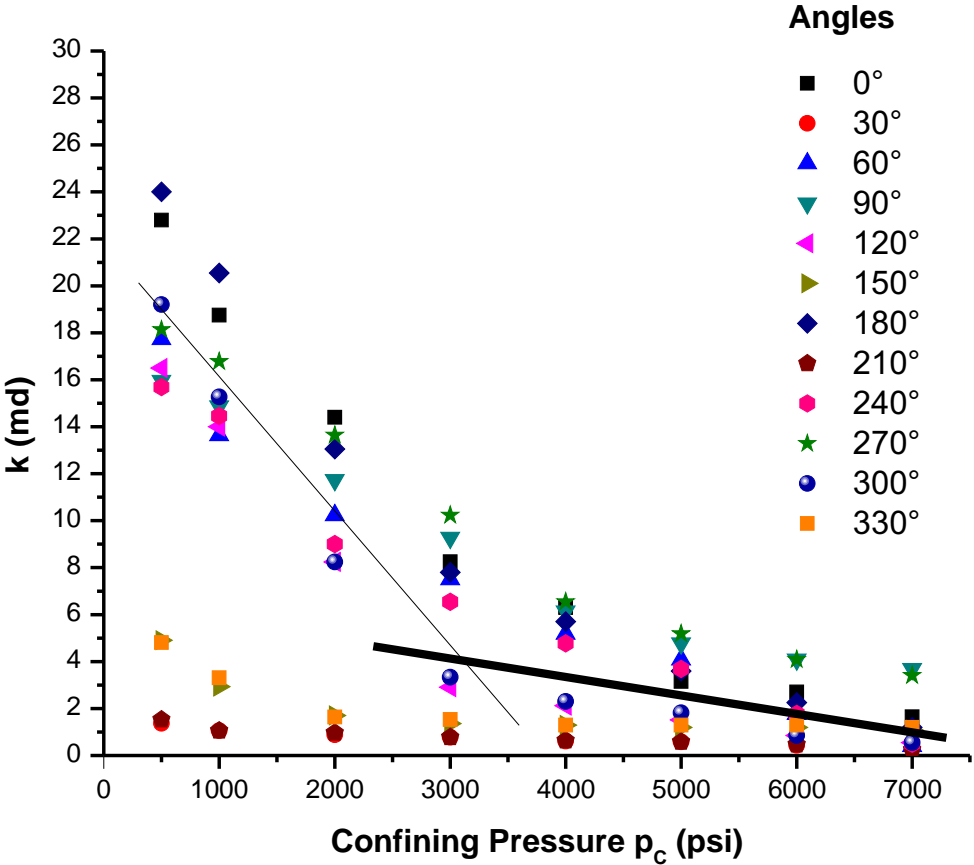


**Fig. 3.4:** Directional permeabilities as a function of confining pressure in the interval 500-7000 psi.

A low permeability region bounded by the directions 30° - 210° and 150° - 330° is distinguished in which a matrix or "primary" permeability can be defined in comparison with the remaining directions that describe a "secondary" permeability type, with mayor permeability values, distinctive characteristic of the double porosity system. Exceeding a confining pressure of 3000 psi, the secondary permeability values, approximate the primary permeability values.

The behavior of the results is similar to those obtained by Nelson (1975). In comparison with the equation of Gangi (1978), the description of Herrera (2000) is proposed in which two lines can be fitted for the representative data of Fig. 3.5, which qualitatively describes the mechanical state of the rock as a function of the confining pressure, or effective stress.

The linear functions are given by the following equations:

$$k_{p_c} = \begin{cases} \frac{k_{500} - k_{3000}}{\Delta p_{c1}} * p_c + k_{maxt} & 500 \text{ psi} \leq p_c \leq 3000 \text{ psi} \\ \frac{k_{3000} - k_{7000}}{\Delta p_{c2}} * p_c + k_{matrix} & 3000 \text{ psi} \leq p_c \leq 7000 \text{ psi} \end{cases} \quad (3.2)$$

The calculation of the slopes of the straight lines with the reference permeabilities is a good approximation, since the adjustment of the straight lines is precise to the experimental points.

In Fig. 3.5, the mechanical behavior of the rock morphology is conceptually shown, in terms of the decrease in secondary permeability as a function of the increase in confining pressure. The experiment was developed up to a pressure of 7000 psi, because exceeding this confining pressure limit there is a risk of fracturing the specimen. In addition, from the determination of the linear functions that describe the permeability trend in the double porosity or fractured region and the matrix region, it is possible to identify the following important facts.

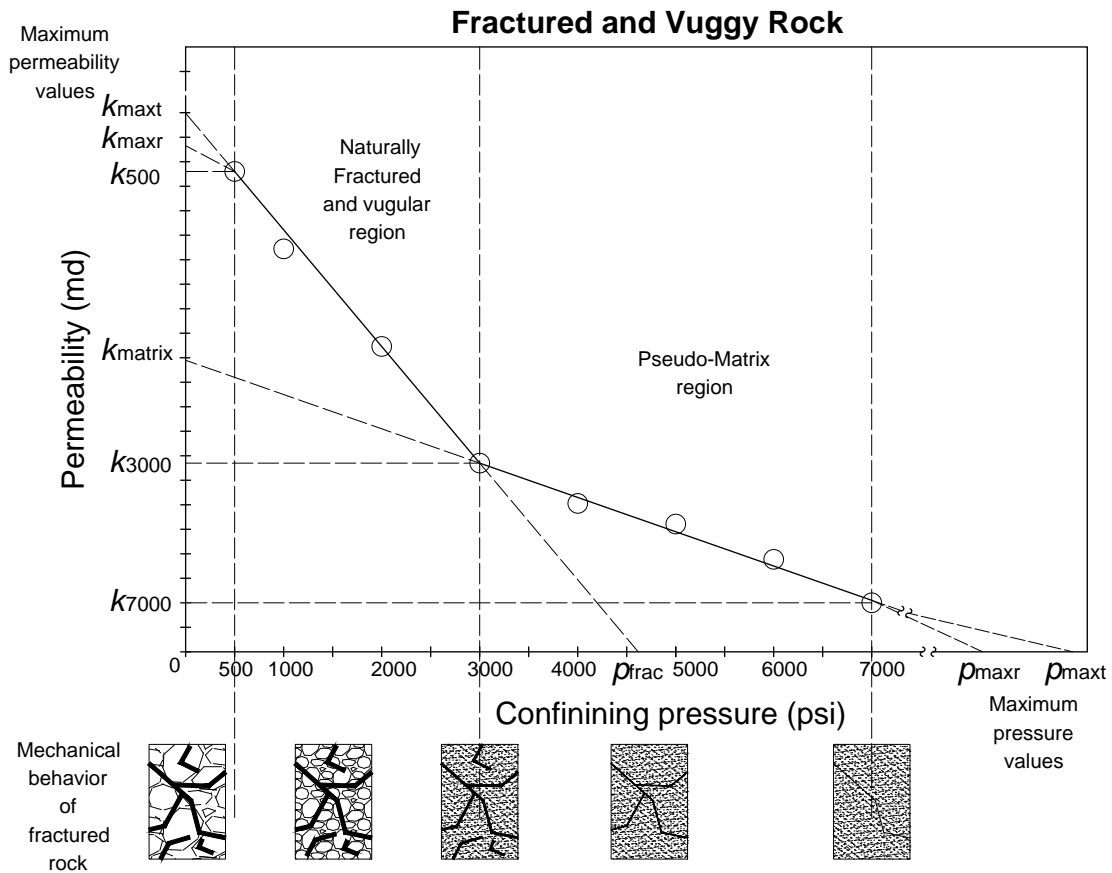


**Fig. 3.5:** Permeability tendency as a function of confining pressure.

A purely fractured region is defined, with a representative high permeability of the double porosity system and with minimum matrix permeability, which is bounded on the "x" axis in the range  $0 \leq x \leq p_{frac}$ , and the "y" axis in the range  $0 \leq y \leq k_{maxt}$  where  $k_{maxt}$  is the theoretical maximum permeability defined by the intersection of the double porosity line with the "y" axis. The value  $k_{maxt}$  is greater than the  $k_{maxr}$ , which is the maximum rock permeability without confining pressure. It is possible to define a predominantly matrix homogeneous region with low and uniform permeability, characteristic of sandstone rocks. This region is bounded in the "x" axis on the pressure interval  $3000 \text{ psi} \leq x \leq 5000 \text{ psi}$ ; it can be extended in the range  $0 \leq x \leq p_{maxt}$  where  $p_{maxt}$  is the theoretical maximum pressure at which the permeability and the porosity tend to reach a null value.

Furthermore, the value  $p_{maxr}$  is the maximum real or experimental pressure in which the permeability and porosity decrease to an approximately zero value. We assume that  $p_{maxr} \leq p_{maxt}$ . This region is initially bounded in the "y" axis by the range  $k_{7000} \leq y \leq k_{3000}$ ; it can be extended to the range  $0 \leq y \leq k_{matrix}$ , where  $k_{matrix}$  is the value determined by the intersection of the pseudo-matrix straight line with "y" axis.

An illustrative example is shown in Fig. 3.6. The linear tendency and the corresponding equations for each region were determined, for the directional permeability of 120°. In this case, the the calculated values with Eq. 3.2 are comparable to those obtained by the least squares fitting.

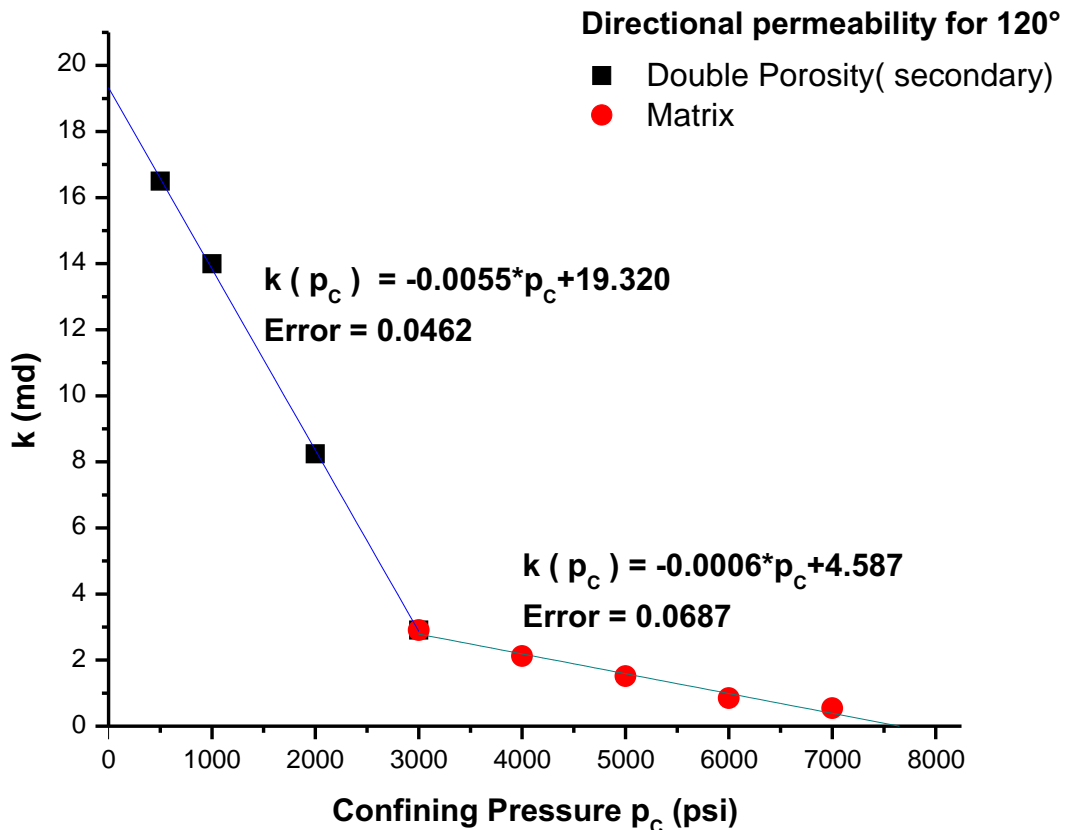


**Fig. 3.6:** Linear permeability plot for 120° directional permeability.

### 3.9 Vertical permeability

The measurement of vertical permeability was performed with nitrogen gas injection in the upper part of the specimen. The results were obtained applying Darcy’s law for gas flow with the necessary corrections. The tendency of compaction is similar to the horizontal directional permeabilities (Fig. 3.7). An important aspect is that the vertical permeability is lower than the horizontal permeabilities. With the linear functions of vertical permeability, it is possible to generate the permeability ellipsoid and build the permeability tensor in 3D with the principal permeability values.  $k_v$  is the vertical permeability along the "z" axis, perpendicular to the plane "x" and "y".

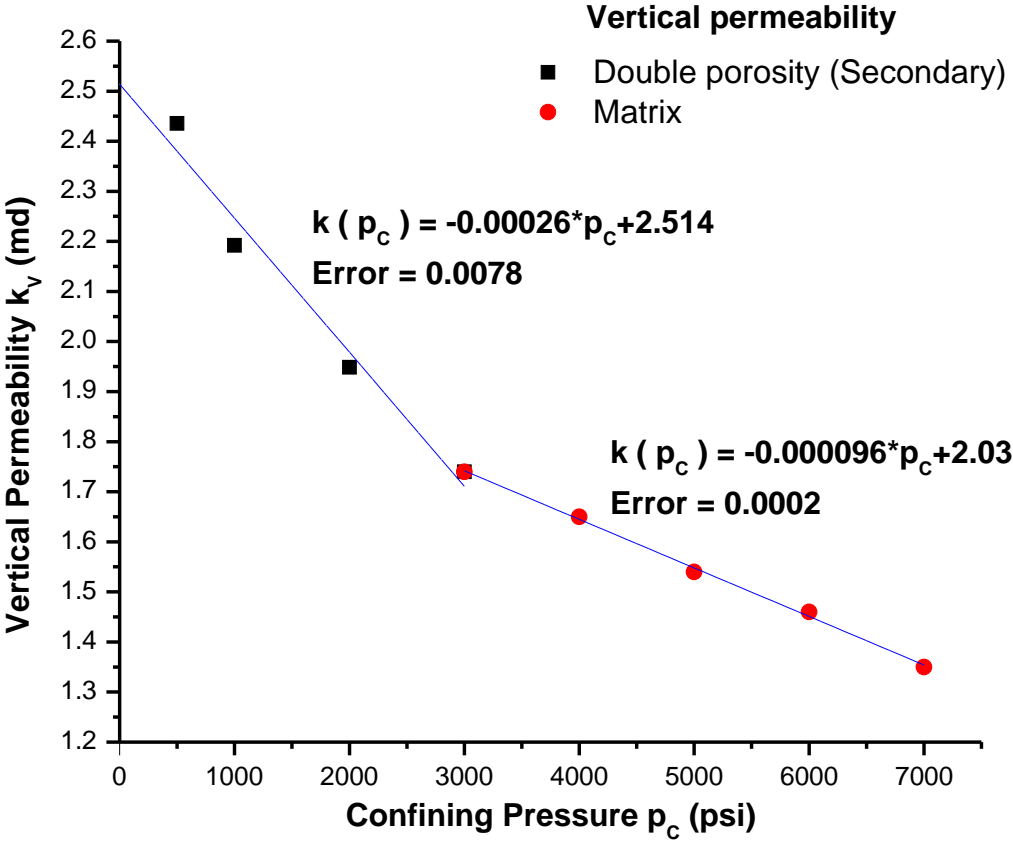
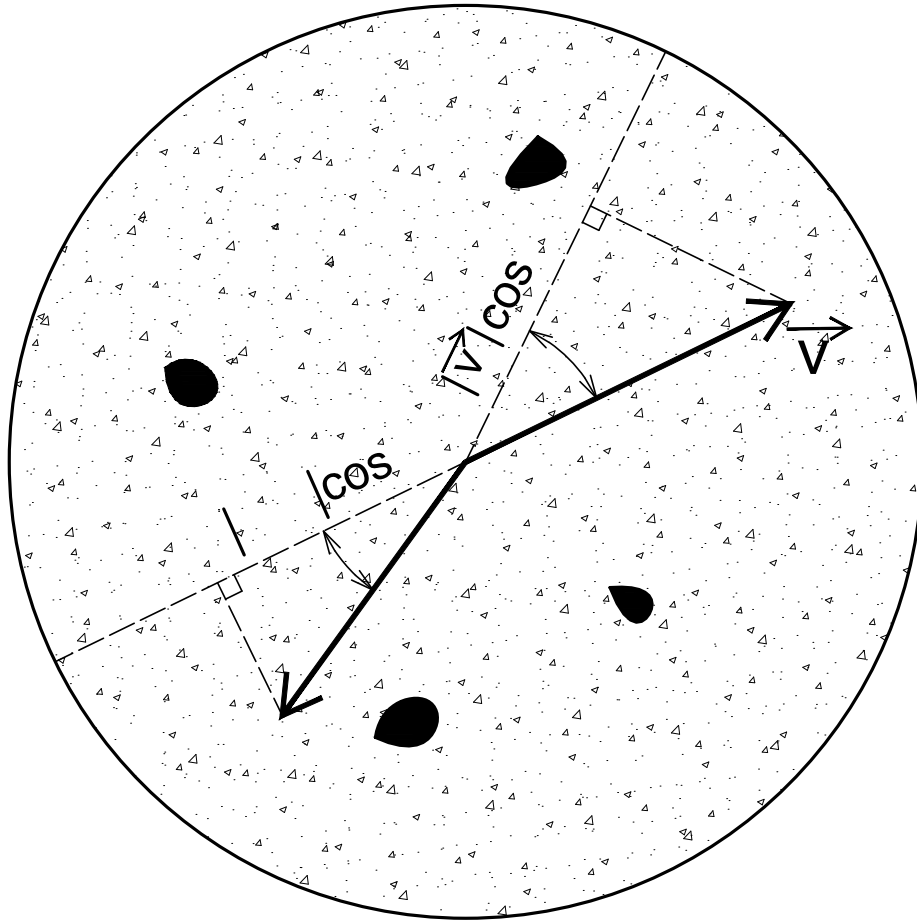


Fig. 3.7: Vertical permeability as a confining pressure function.

### 3.10 Permeability ellipses

Three types of permeability ellipse plots are developed; a) the graph of  $k$  as a function of the directional angle; b) the graph of  $\sqrt{k}$  as a function of the directional angle, which corresponds to the directional permeability in the direction of Darcy velocity vector flow; c) the graph of  $1/\sqrt{k}$  as a function of the directional angle which corresponds to the directional permeability in velocity potential gradient. Next, the corresponding equations for the permeability ellipses are defined. For anisotropic media, the Darcy velocity vector and the velocity potential gradient vector are not collinear (Fig. 3.8).



**Fig. 3.8:** Relationship between the Darcy velocity vector flow and the velocity potential gradient vector in porous rocks.

The directional permeability  $k_{df}$  in the flow direction is defined in Darcy units:

$$k_{df} = \frac{\mu |v|}{|\nabla\Phi| \cos \beta} \quad (3.3)$$

The canonical equation of the permeability ellipse is obtained by analyzing the relationship of directional permeability in the direction of flow as a function of the principal permeabilities:

$$\frac{x^2}{(\sqrt{k_x})^2} + \frac{y^2}{(\sqrt{k_y})^2} + \frac{z^2}{(\sqrt{k_z})^2} = 1 \quad (3.4)$$

The directional permeability  $k_{df}$  in the direction of velocity potential gradient vector is defined in Darcy units:

$$k_{df} = \frac{\mu |v| \cos \beta}{|\nabla\Phi|} \quad (3.5)$$

Analyzing the relationship of the permeability in the direction of the velocity potential gradient as a function of the principal directional permeabilities, the following equation is obtained:

$$\frac{x^2}{\left(\frac{1}{\sqrt{k_x}}\right)^2} + \frac{y^2}{\left(\frac{1}{\sqrt{k_y}}\right)^2} + \frac{z^2}{\left(\frac{1}{\sqrt{k_z}}\right)^2} = 1 \quad (3.6)$$

The next section presents the tendency of two ellipses corresponds to the double porosity of the rock (matrix and vuggy - fractures).

### 3.11 Permeability experimental results

The ellipse fitting was done by the method of direct square minimums and the algorithm of Fitzgibbon et al. (1999). The ellipses plotted with the permeability data for a confining pressure of 500 psi are shown in Fig. 3.9. Two types of data were classified, those corresponding to primary permeability (primary porosity) and secondary permeability data (secondary porosity). Directions of 30° - 210°, 150° - 330° belong to the primary permeability ellipse. The directions of 0° - 180°, 60° - 240°, 90° - 270°, 120° - 300° belong to the secondary permeability ellipse.

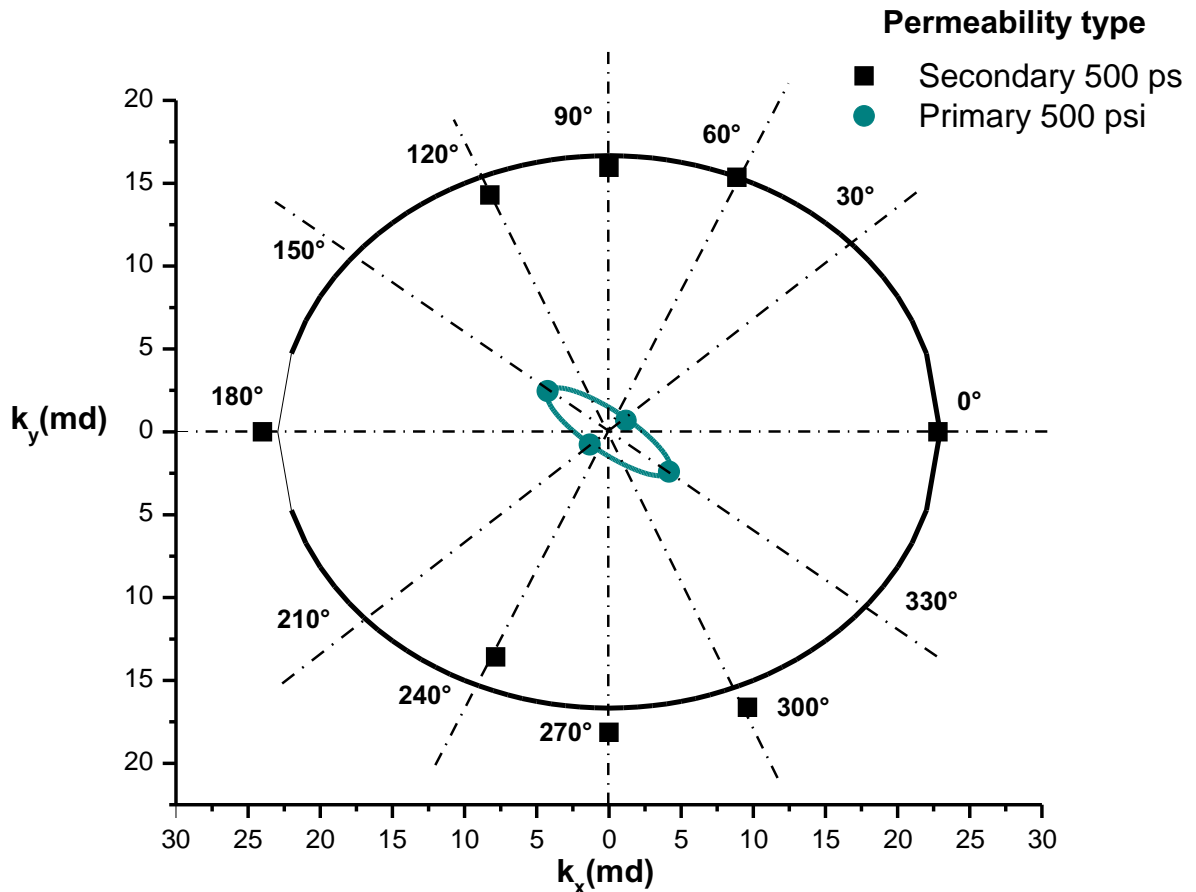
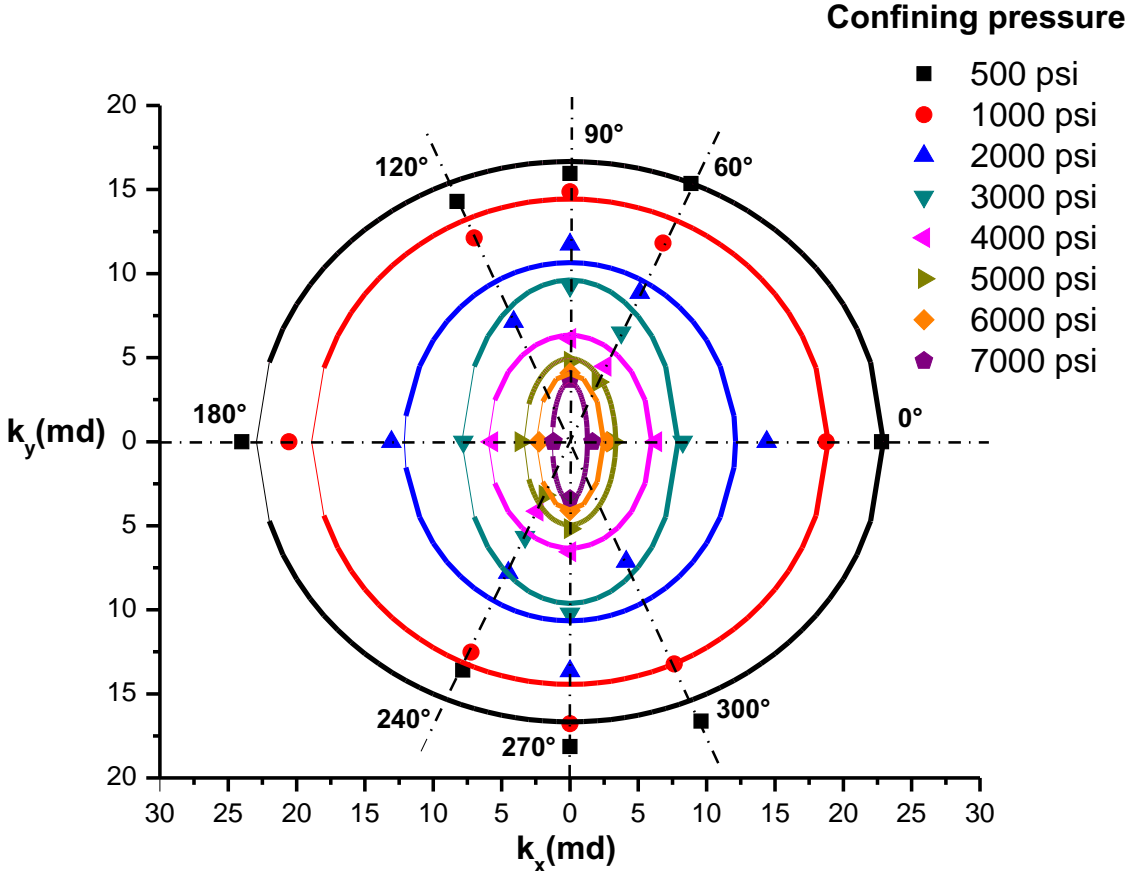


Fig. 3.9: Directional permeabilities measured at a confining pressure of 500 psi.



Fig. 3.10 shows the influence of confining pressure on secondary permeability ellipses, for pressure increases of 500 psi and 1000 psi in the range of 500 to 7000 psi. The permeability graph clearly reflects the behavior as a stress function. The ellipses present a size reduction as a function of the increment in confining pressure and a constant temperature of 120 °C.

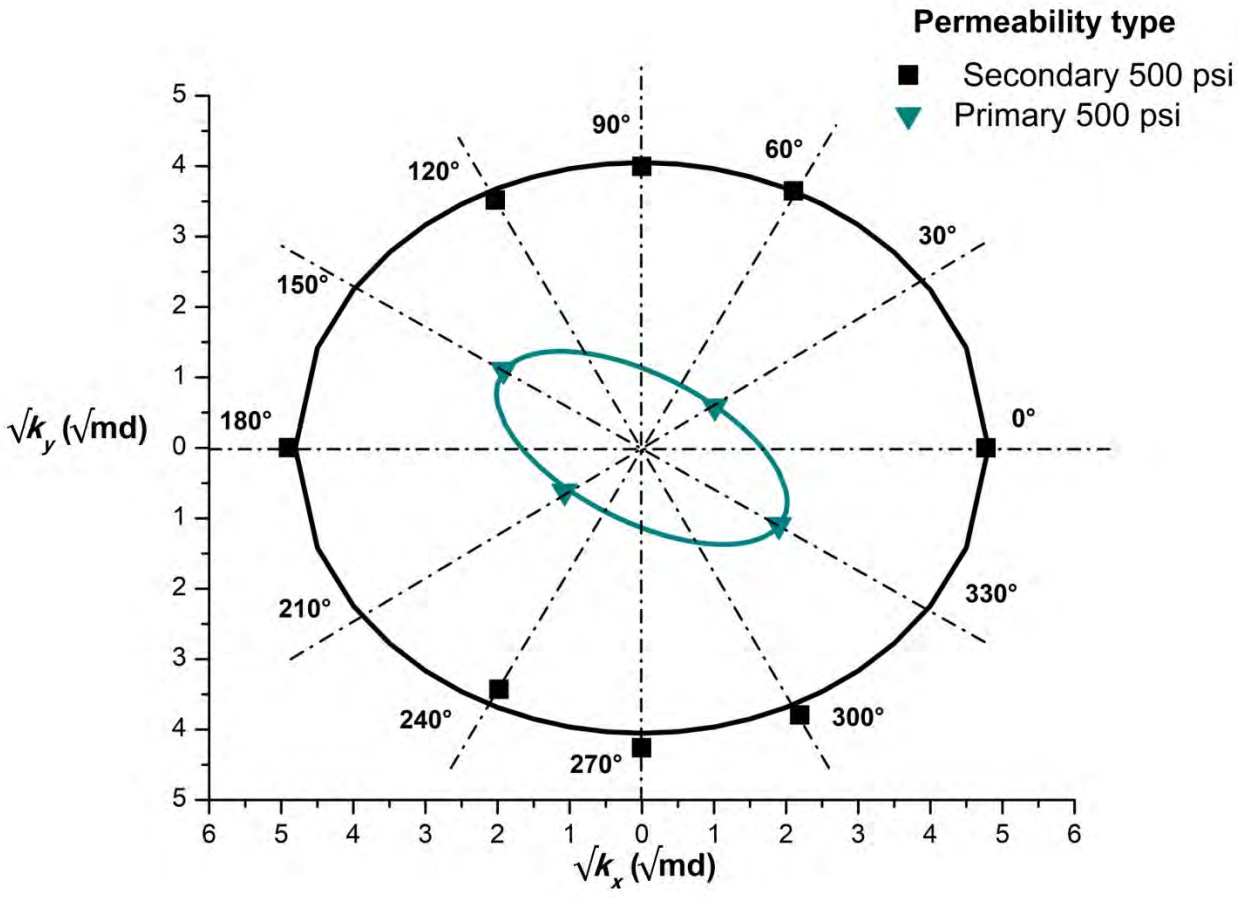
The combination of high-pressure and high-temperature permit an elastoplastic behavior and ductility in the rock. Figs. 3.11 and 3.12 shows the permeability plots in the flow direction version of Figs. 3.9 and 3.10.



**Fig. 3.10:** Directional permeabilities measured in the confining pressure range of 500 -7000 psi.

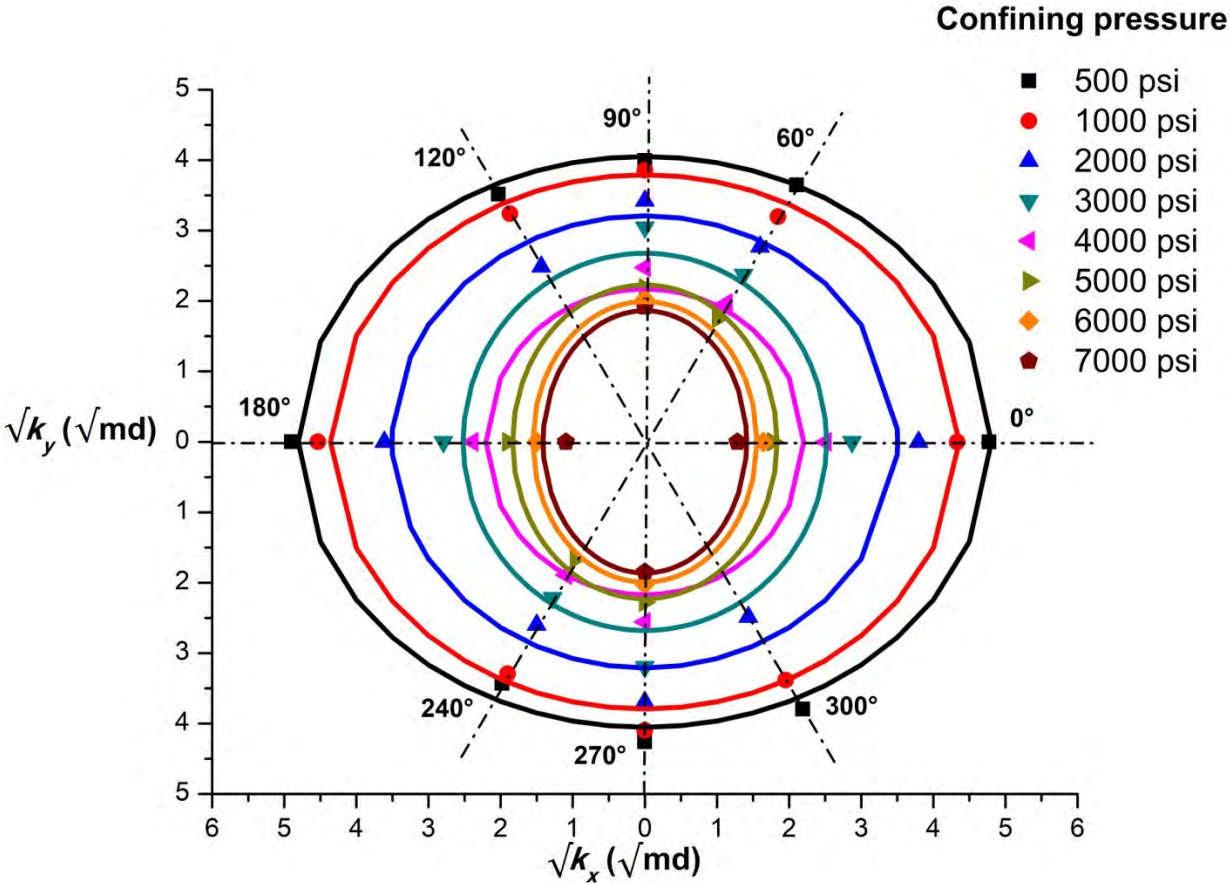
Fig. 3.11 shows the plots of secondary and primary permeability ellipses for a constant confining pressure value of 500 psi and a constant temperature of 120 °C. The two permeability ellipses show the initial morphology of the rock with a minimum value of confining pressure (effective stress).

Also, this graph is a function of the  $\sqrt{k}$  value of permeability, representative of the nitrogen flow direction. This type of plot of  $\sqrt{k}$  and directional permeabilities permit a better visualization and best fitting of the data than the plots as a function of permeability  $k$ .



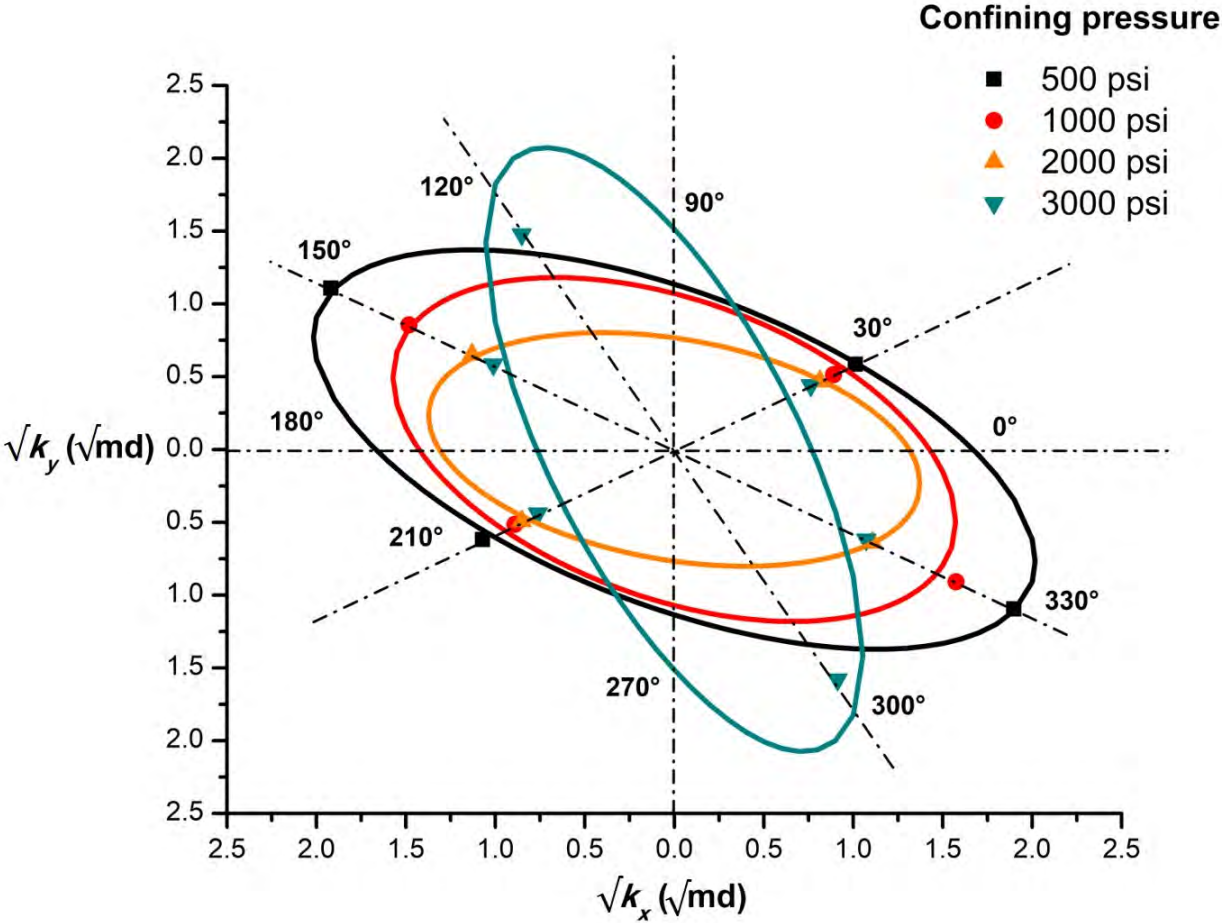
**Fig. 3.11:** Directional permeabilities measured at a confining pressure of 500 psi. Ellipse of permeabilities in the direction of flow.

Fig. 3.12 shows the plots of secondary permeability ellipses as a function of  $\sqrt{k}$  for pressure increments of 500 psi and 1000 psi in the range of 500 to 7000 psi, and constant temperature of 120 °C. In this graph only are plotted the directional permeabilities of 0° - 180°, 60° - 240°, 90° - 270°, 120° - 300°. The principal axes of the permeability ellipse in the direction 0°-180° (maximum permeability) and 0°-90° (minimum permeability), for a confining pressure value of 500 psi, present a rotation of 90 degrees due to the increase in the confining pressure. For a pressure of 7000 psi, the ellipse has been reduced to a representative state of pseudo-matrix permeability.



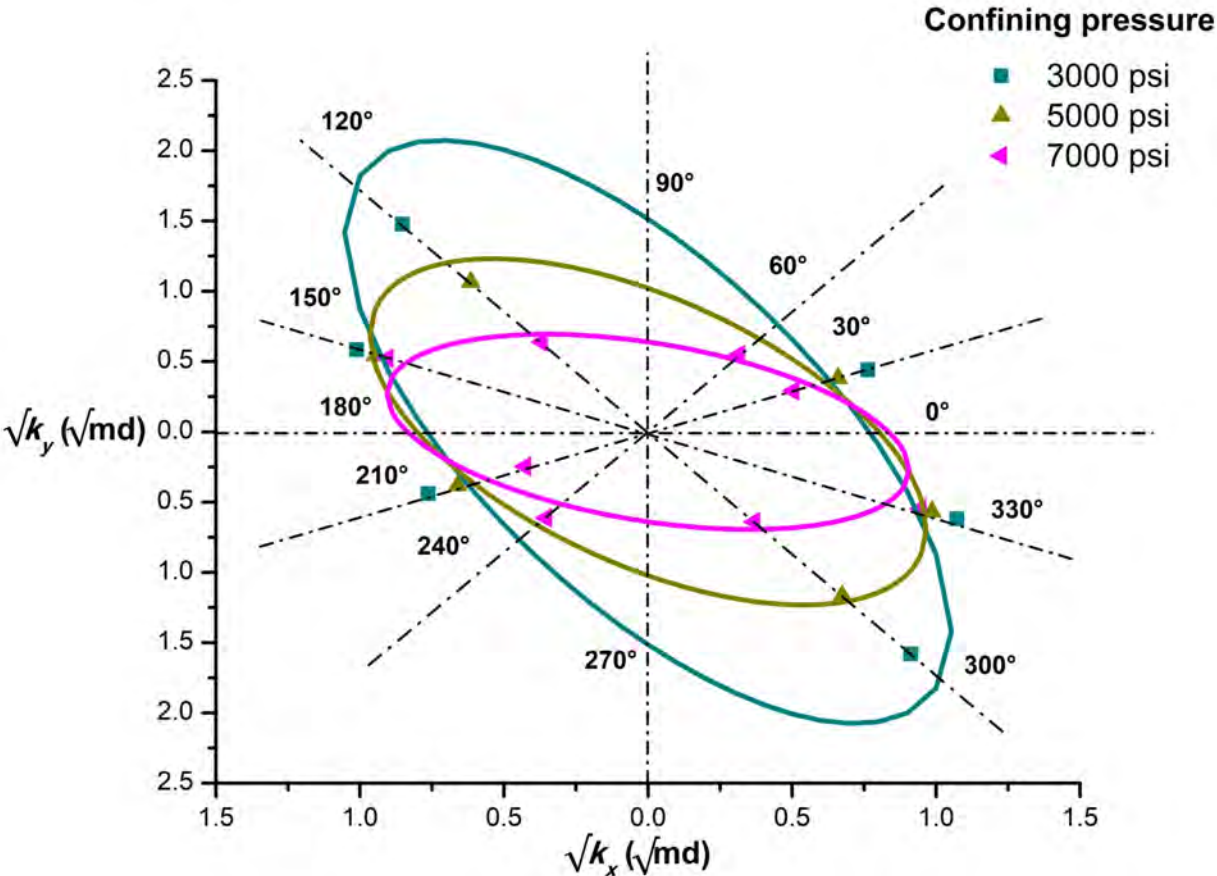
**Fig. 3.12:** Directional permeabilities measured in the confining pressure range of 500 -7000 psi. Ellipse of permeabilities in the direction of flow.

Fig. 3.13 shows the permeability ellipses as a function of  $\sqrt{k}$  for pressures of 500, 1000, 2000 psi, and 3000 psi. The geometrical rotation of ellipses is due to the fact that the higher directional permeabilities decrease from secondary permeability to primary permeability, as applied stress increments. Concerning direction 120° - 300°, at 3000 psi pressure, the permeability reduce from the region of secondary porosity to the pseudo-matrix region. The change in tendency in the straight lines of Fig. 3.4, for a confining pressure of 3000 psi is due to the compaction of the directional permeabilities corresponding to the secondary permeability.



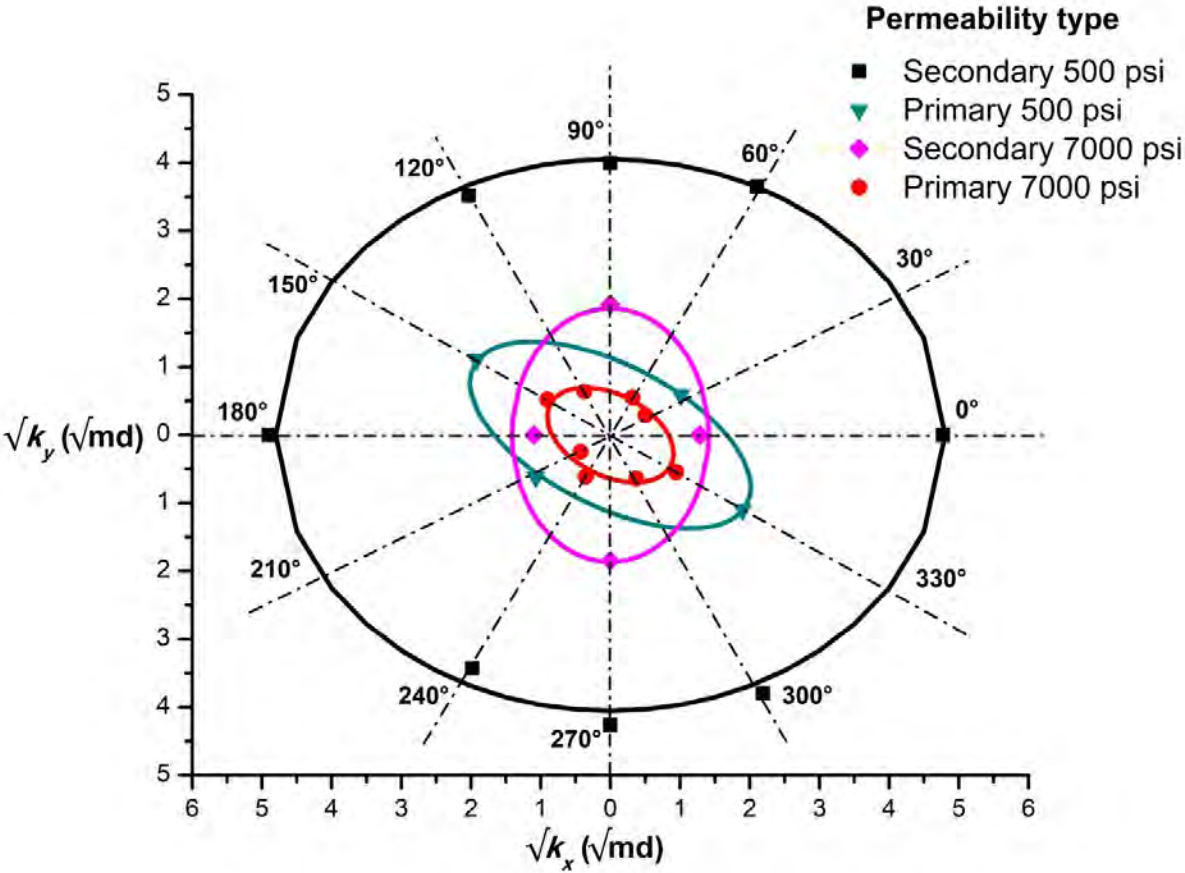
**Fig. 3.13:** Compaction tendency of the primary permeability in a pressure range of 500-3000 psi.

Fig. 3.14 shows the permeability ellipses as a function of  $\sqrt{k}$  for pressures of 3000, 5000 and 7000 psi. The 60° - 240° direction reaches the primary permeability region up to a pressure of 7000 psi. The directions 30° - 210°, 60° - 240°, 120° - 300°, 150° - 330° are mainly compacted at a confining pressure of 7000 psi. The rotation of the axes of the ellipses is a function of the effective stress, a rotation of 30° was generated in a counter-clockwise direction, from the direction of 120°-300° to 150°-330°, produced by an increment in the confining pressure from 3000 to 7000 psi with a constant temperature of 120°C. The observed rotation and reduction physically represents the ductility and compaction of the carbonate rock.



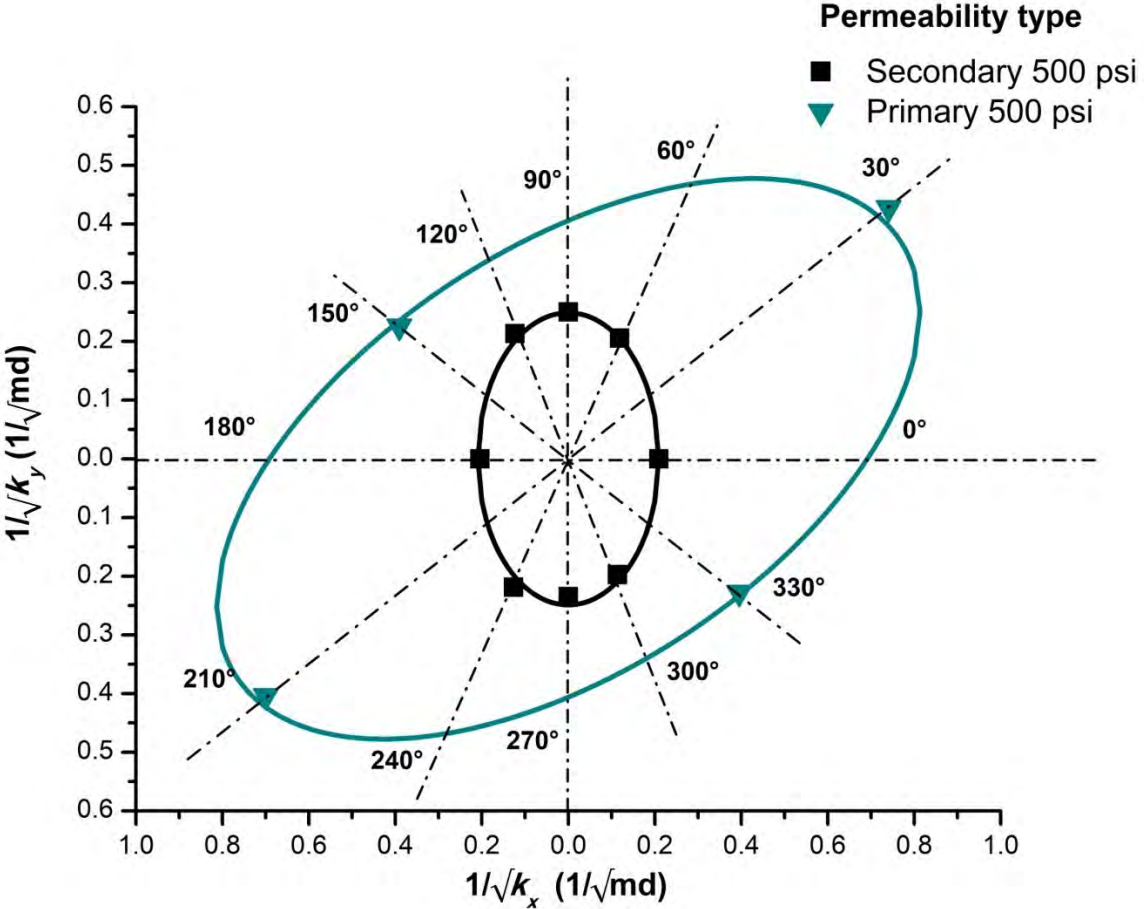
**Fig. 3.14:** Compaction tendency of primary permeability in a pressure range of 3000 -7000 psi.

The confining pressure effect on the permeability ellipse  $\sqrt{k}$  is shown in Fig. 3.15, where a comparison of the results for 500 psi and 7000 psi is shown. The principal directions of permeability are  $0^\circ - 180^\circ$  and  $90^\circ - 270^\circ$ , which have higher values compared to the other directions. The principal axis of the secondary ellipse rotated  $90^\circ$  due to the application of stress. The principal axis of the primary permeability ellipse was approximately constant along the direction of  $150^\circ - 330^\circ$ . For a confining pressure of 7000 psi, all the directional permeabilities were compacted in a unique ellipse that represents the pseudo-matrix morphology of the rock. This change in the directions of the permeability axis, must be taken into account in reservoir simulation studies.



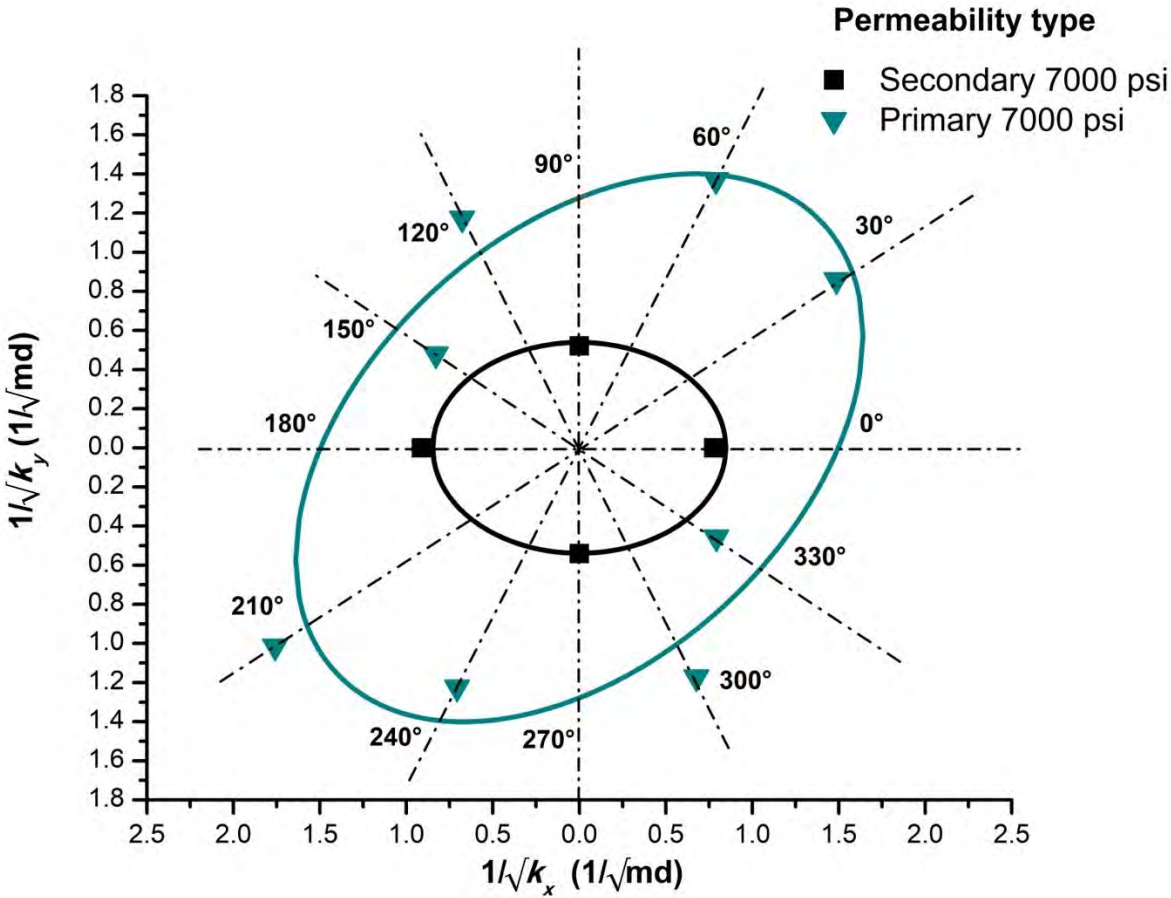
**Fig. 3.15:** Comparison of secondary permeability ellipse and primary permeability ellipse, at confining pressures of 500 psi and 7000 psi.

Fig. 3.16 shows the permeability ellipses  $1/\sqrt{k}$  for a confining pressure of 500 psi, presenting an inverse behavior in comparison with the ellipses  $k$  and  $\sqrt{k}$ , since the ellipse that represents the primary permeability is geometrically greater than the secondary permeability ellipse, due to the construction of the ellipse as a function of the ratio  $1/\sqrt{k}$ . For this type of representation, the principal axis of the secondary permeability ellipse is aligned in the permeability direction of  $30^\circ$ - $210^\circ$  (major axis), and the axis of the primary permeability ellipse, the major coincides with "y" axis. This plot physically represents the permeability in the direction of the velocity potential gradient.



**Fig. 3.16:** Primary and secondary permeability ellipses in terms of  $1/\sqrt{k}$ , at a confining pressure of 500 psi in the direction of the velocity potential gradient.

The permeability ellipses for 7000 psi pressure are shown in Fig. 3.17; the reduction of the directions of 60° - 240° and 120° - 300° to the primary permeability ellipse is observed, generated by the effective stress increment. In this plot, the major axis of the primary permeability is approximately aligned with the direction 30°-210°, and the major axis of the secondary permeability is aligned with the "x" axis. Due to the inverse behavior of the permeability ellipses, it was concluded that the best graphic representation of the permeability is generated from  $\sqrt{k}$ , that is, the ellipses constructed as a function of the direction of flow. Finally, in each representation, permeability is clearly identified.



**Fig. 3.17:** Primary and secondary permeability ellipses of  $1/\sqrt{k}$ , at a confining pressure of 7000 psi in the direction of the velocity potential gradient.



In Fig. 3.18 the decrease of the horizontal permeability values are observed with respect to the main permeability axes, as a function of the confining pressure.  $k_{HMAX}$  is the maximum horizontal principal permeability corresponding to the direction of  $0^\circ - 180^\circ$  on the "x" axis,  $k_{H90}$  is the minimum horizontal principal permeability perpendicular to the maximum permeability axis  $0^\circ - 180^\circ$  or "x" axis, and corresponding to the direction  $90^\circ - 270^\circ$  on the "y" axis. The generated permeability tensor corresponds to the secondary permeability tensor. In this case, the principal permeability values coincide with the direction of the axes "x" - "y" axis; the direction of  $0^\circ - 180^\circ$  was defined based on a visual inspection of the rock that presented superficial relevant secondary porosity (vuggy and fractures). However, the methodology is applicable to heterogeneous complex rocks, and the permeability tensor is determined by the principal axes of the permeability ellipses.

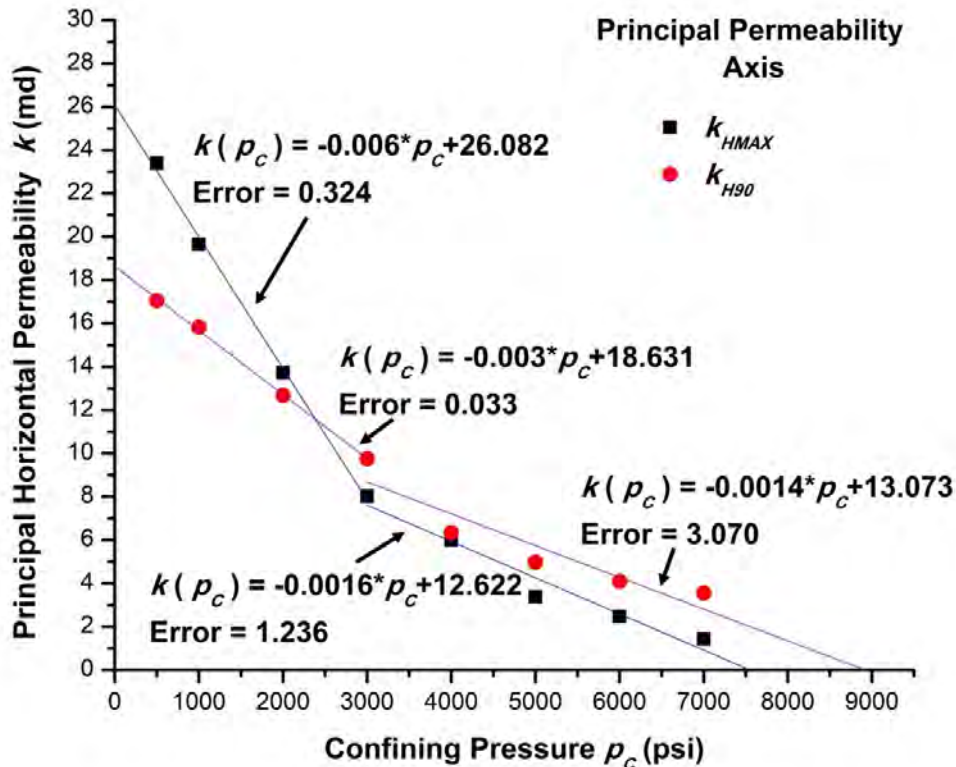


**Fig. 3.18:** Principal horizontal permeability axes tendency.

## 3.12 Permeability tensor

### 3.12.1 Secondary permeability tensor

With the experimental results and the permeability ellipses generation, the principal permeability axes and the principal values of the 3D permeability tensor were determined. With vertical permeability, a 3D permeabilities ellipsoid can be constructed, with geometrically similar behavior to the 2D ellipse, decreasing as the confining pressure increases. It is possible to generate two permeability tensors. This physical behavior and the respective mathematical representation applies to a naturally fractured rock. It is possible to identify triple porosity-permeability behavior and generate three ellipses, however, the author recommends the double media representation like a clear and practical discretization of the morphology of the rock.

The equations of the ellipses of secondary permeability are written in the canonical form of an equation of the ellipse, with center at the origin. For the case of the ellipsoids depending on the permeability  $k$ , varying according to the confining pressure the equations are given by Eq. 3.7

$$\frac{x^2}{(k_{HMAX})^2} + \frac{y^2}{(k_{H90})^2} + \frac{z^2}{(k_v)^2} = 1 \quad (3.7)$$

For the ellipsoids  $\sqrt{k}$ , the equations are of the form:

$$\frac{x^2}{(\sqrt{k_{HMAX}})^2} + \frac{y^2}{(\sqrt{k_{H90}})^2} + \frac{z^2}{(\sqrt{k_v})^2} = 1 \quad (3.8)$$

For the ellipsoids  $1/\sqrt{k}$ , the equation is as follows:

$$\frac{x^2}{\left(\frac{1}{\sqrt{k_{HMAX}}}\right)^2} + \frac{y^2}{\left(\frac{1}{\sqrt{k_{H90}}}\right)^2} + \frac{z^2}{\left(\frac{1}{\sqrt{k_v}}\right)^2} = 1 \quad (3.9)$$

Therefore the 3D permeability tensor  $\bar{\bar{\mathbf{k}}}$  is expressed by the next matrix:

$$\bar{\bar{\mathbf{k}}} = \begin{bmatrix} k_{HMAX} & 0 & 0 \\ 0 & k_{H90} & 0 \\ 0 & 0 & k_v \end{bmatrix} \quad (3.10)$$

The tensor is defined directly from the experimental results for each confinement pressure. The permeability tensor  $\bar{\bar{\mathbf{k}}}_f$ , that represents the fractured region range  $500 \text{ psi} \leq p_c \leq 3000 \text{ psi}$ , also can be expressed as a function of the confining pressure, inserting the equations of Figs. 3.7 and 3.18 in to the matrix given by Eq. 3.11:

$$\bar{\bar{\mathbf{k}}}_f = \begin{bmatrix} -0.006P_c + 26.082 & 0 & 0 \\ 0 & -0.003P_c + 18.631 & 0 \\ 0 & 0 & -0.00026P_c + 2.514 \end{bmatrix} \quad 500 \text{ psi} \leq p_c \leq 3000 \text{ psi} \quad (3.11)$$

For the range  $3000 \text{ psi} \leq p_c \leq 7000 \text{ psi}$ , the principal axis of maximum permeability coincides with the "y" axis. In the 3000 psi transition, a rotation of  $90^\circ$  of the maximum permeability on the "x" axis was generated in the direction of the "y" axis. The permeability tensor  $\bar{\bar{\mathbf{k}}}_m$  that represents the pseudo-matrix (primary) region is given by:

$$\bar{\bar{\mathbf{k}}}_m = \begin{bmatrix} -0.0014P_c + 13.073 & 0 & 0 \\ 0 & -0.0016P_c + 12.622 & 0 \\ 0 & 0 & -0.000096P_c + 2.032 \end{bmatrix} \quad 3000 \text{ psi} \leq p_c \leq 7000 \text{ psi} \quad (3.12)$$

The three matrices are expressed in a diagonal form, with values written as a function of the confining pressure. The matrices are valid only in the pressure range of the linear equations that represent the principal permeability values.

### 3.12.2 Primary permeability tensor

In the case of the tensor corresponding to the region of low permeability it can be observed in Fig. 3.13, Fig. 3.14 and Fig. 3.15, the major major axis of permeability coincides with the direction of  $150^\circ - 330^\circ$ . However, analyzing in detail Figs. 3.13 and Fig. 3.14, it is observed that the principal axes of the permeability ellipses as a function of  $\sqrt{k}$  vary slightly around the main directions  $150^\circ - 330^\circ$  for the major axis, and  $60^\circ - 240^\circ$  for the minor axis of the ellipses.

Additionally, it is possible to transform the primary permeability tensor over the principal directions ("x" and "y" axis) of the secondary permeability tensor by coordinate transformation, with a rotation angle  $\theta = 30^\circ$  from the positive "x" axis.

The 2D tensor  $\overline{\overline{\mathbf{k}}}_{\text{pr}}$  as a function of the positive maximum permeability  $k_{330}$  (directional permeability  $330^\circ$ ) and the positive minimum permeability  $k_{60}$  (directional permeability  $60^\circ$ ), are considered a right-handed coordinate system, is expressed by the matrix of Eq. 3.13; the tensor is a function of the confining pressure:

$$\overline{\overline{\mathbf{k}}}_{\text{pr}} = \frac{1}{4} \begin{bmatrix} 3k_{60} + k_{330} & \sqrt{3}(k_{60} - k_{330}) \\ \sqrt{3}(k_{60} - k_{330}) & k_{60} + 3k_{330} \end{bmatrix} \quad (3.13)$$

The fact that the permeability tensors are symmetric gives rise to great simplifications, because it corresponds only to a transformation from the principal axes to another rectangular system of reference and permits the simple graphical construction of the tensor ellipsoid.

The matrix functions mathematically represent the coupled geomechanical effects in the rock. The tensors can be applied in the construction of a mathematical model for fractured rocks and numerical studies of flow fluids in deformable and high compressible media.

### 3.13 Conclusions

The proposed experimental determination of the permeability tensor offers the following advantages:

- Design of a new petrophysical test for the determination of permeability ellipses in fractured and vugular rocks, at a laboratory scale.
- Methodology of easy application and does not require sophisticated equipment.
- Determination of principal permeability directions to develop representative displacements, for vuggy rocks where visual identification of the best directions is not enough.
- Determination of multi-region permeability ellipses for double porosity rocks. For homogeneous rocks, only one ellipse of permeability is generated.
- Compaction influences in the permeability ellipses.
- Confining pressure of 3000 psi was estimated for the transition from the fractured region to the pseudo-matrix region. An experimental rule for fractured rocks.
- Application of linear model interpretation by straight lines, of the variation in permeability as a function of the effective stress.
- Discretization of the matrix-fracture system based on the linear interpretation for double porosity rocks.
- Contribution to consolidate the theoretical and experimental bases for the theory of "mechanics of fractured porous rocks".

# Chapter 4

## Estimation of Residual Oil Saturation in a Fractured Rock by Scaling Immiscible Displacement

### 4.1 Abstract

A novel experimental immiscible displacement test for full diameter fractured rock samples, was designed to estimate the residual oil saturation in the vuggy-fracture and pseudo-matrix system at the oil-water transition zone of a giant naturally fractured reservoir. The discretization of residual oil saturation is of paramount importance for the implementation of improved oil recovery processes at the field scale. The key to the design is the nature of compaction in the rock described in Chapter 3 and is fundamental to understand the production of fluids and the residual oil saturation.

With dimensional analysis, a dimensionless geomechanical time was obtained for each of the displacements. The expression is a generalization of the time of [Mattax and Kyte \(1962\)](#), that includes a stress ratio. Also, the physical behavior of the displacement in the laboratory was compared with the reservoir behavior.

## 4.2 Introduction

The design of an immiscible displacement test (water-oil) is proposed to determine the residual oil saturations in the transition zone invaded by water in the fracture-matrix system of a giant naturally fractured reservoir from the Gulf of Mexico, depending on the effective stress applied. The design is based on geomechanics scaling laws (fluid flow, petrophysical and geomechanical similitude).

The scaling laws based on mechanical properties of the fluid flow and the rock, satisfy the similitude between the fractured whole core (model) at the laboratory scale and the naturally fractured reservoir oil field (prototype) (Fig. 4.1). Furthermore, the advance of the oil-water contact was simulated experimentally; also, it is possible to simulate the future reservoir behavior in order to obtain a residual oil saturation and estimation of reservoir depletion. The methodology can be applied for the determination of residual oil saturation in the gas-oil contact zone.

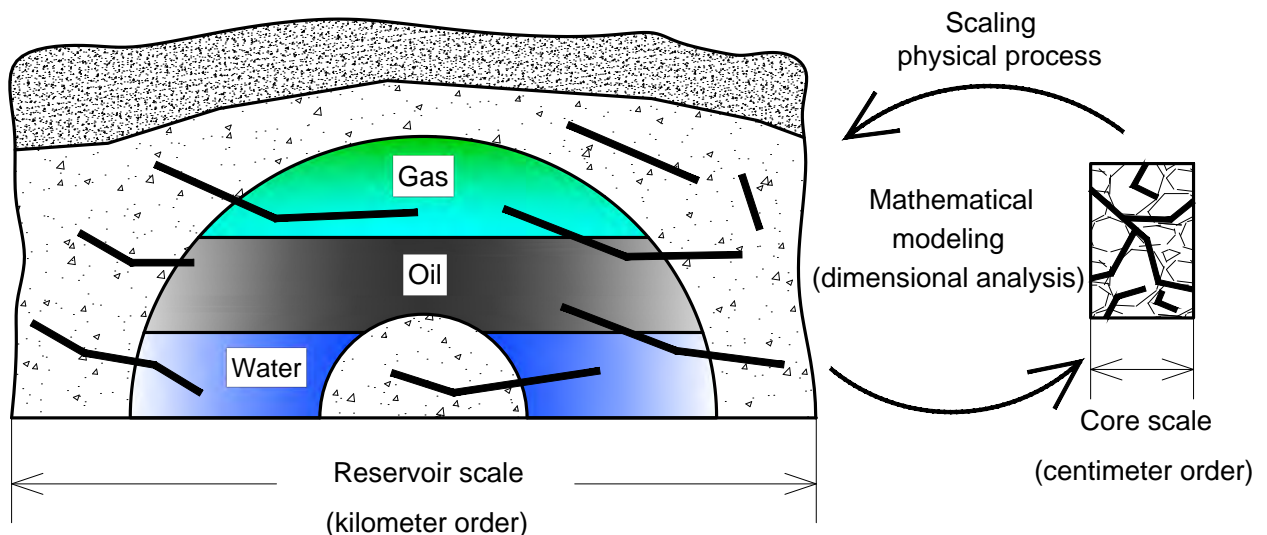


**Fig. 4.1:** Schematic representation of mathematical and physical scaling of a naturally fractured reservoir (prototype) and fractured whole rock (model).

## 4.3 Classical scaling techniques

Scaling is the translation from a larger scale to a smaller one or vice versa; the petrophysical properties of the system are fundamental to scale the experiments, under conditions in which the geomechanical behavior of the rock (fluid and rock dynamics) is physically similar to the reservoir at field conditions. Under scaling conditions, it is possible to estimate a residual oil saturation in the matrix - fracture system equivalent to the naturally fractured reservoir under study.

Understanding the behavior of multiphase flow in a naturally fractured reservoir requires experimental models (rocks) and mathematical techniques of scaling, which allow the experimental test to be scaled (Greenkorn (1964) and Peters et al. (1993)) to reservoir conditions. The methods for scaling the gas-oil-contact and/or the water-oil-contact are:

- Dimensional analysis, which has a physical and mathematical foundation based on Buckingham's  $\pi$  theorem (Buckingham (1914); Rayleigh (1915); Bridgman (1931); Barenblatt (2003)).
- Inspectional analysis (Ruark (1935)).

Next, a brief introduction of the two methods is presented. Concerning the dimensional analysis introduction, taken from the Fluid Mechanics book of White (2011), presents an excellent overview of the dimensional analysis for engineering problems. An advanced treatment of the method is presented in the Scaling book of Barenblatt (2003).



## 4.4 Dimensional analysis

Dimensional analysis is a method for reducing the number and complexity of experimental variables that affect a given physical phenomenon. If a phenomenon on  $n$  dimensional variables, dimensional analysis will reduce the problem to only  $k$  dimensionless variables. Generally  $n - k$  equals the number of different dimensions (sometimes called basic or primary or fundamental dimensions) that govern the problem. In the mechanics of continua field, the four basic dimensions are usually taken to be mass  $M$ , length  $L$ , time  $T$ , and temperature  $\Theta$ , or an  $MLT\Theta$  class of units. The purpose is to reduce variables and group them in dimensionless form. Historically the first person to study extensively about units and dimensional reasoning was Euler in 1765. Euler's ideas were very advanced in his time, as well as those of Joseph Fourier, who wrote in 1822 *Analytical Theory of Heat*, where he establishes the principle of dimensional homogeneity and develops some similarity rules for heat flow. An important contribution is Lord Rayleigh's book, *Theory of Sound*, in which he proposed a method of dimensions and provides several examples of dimensional analysis [White \(2011\)](#).

The final advance that established the method of dimensional analysis as we know it today is attributed to [Buckingham \(1914\)](#); The theory states that any equation that comprehensively describes a relationship between a certain number of physical quantities can be reduced to the form  $\phi(\pi_1, \pi_2, \dots, \pi_n) = 0$ , in which  $\pi$ 's are all dimensionless products that are formed from the original parameters of the problem in question; therefore, dimensionless groups establish global correlations between the fundamental variables, instead of studying the influence of each variable separately. After Buckingham's work, [Bridgman \(1931\)](#) published the classic book *Dimensional Analysis*, definitively establishing the theory of dimensional analysis. Dimensional analysis is a powerful tool, which applied with ingenuity and experience in solving engineering problems, establishes an elegant way of understanding physical phenomena and their causes.

## 4.5 Inspectional analysis

Ruark (1935) established the foundations of the inspection analysis. In this method it is necessary to obtain the differential equations that describe the physical process, and to set the initial and boundary conditions associated with the problem, to determine the dimensionless groups that govern the process. The inspectional analysis allows obtaining more effective dimensionless groups than those determined with the dimensional analysis, due to the physical essence, based on the differential equations (Fig. 4.2).

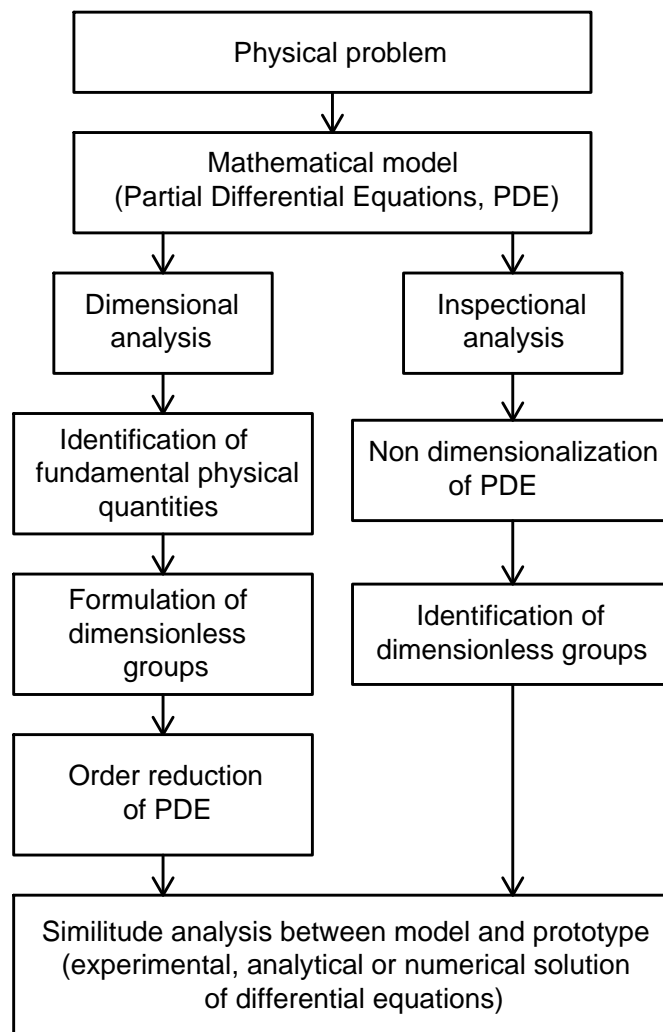


**Fig. 4.2:** Comparative diagram between dimensional and inspectional analysis.

## 4.6 Background

There are many works on scaling and dimensional analysis of multiphase fluid flow in porous media in the literature. Next, a synthesis of the main works is presented.

[Leverett et al. \(1942\)](#), presents two experimental models of flow (radial and linear flows) designed based on dimensional analysis. Experimental limitations are the use of fine and coarse sand, SAE 70 lubricating oil to simulate oil, glycerin to simulate water. [Engelberts and Klinkenberg \(1951\)](#) and [Croes and Schwarz \(1955\)](#) used basic scaling groups and performed experiments in unconsolidated sands that confirmed that the oil/water ratio is one of the major factors governing the efficiency of the displacement process.

[Rapoport and Leas \(1953\)](#) studied the length of the system and injection rate variables required for the scaling of two-phase flow experiments. [Craig et al. \(1955\)](#) performed experiments to study the effect of a mobility gradient on displacement (water drive and gas drive) areal sweep efficiency, in a consolidated sandstone and x-ray shadowgraphs. Only one scaling criterion was applied.

[Rapoport \(1955\)](#), developed the three-dimensional mathematical formulation of a two-phase flow system and obtained scaling laws based on the similitude of relative permeabilities and capillary pressure functions. An important limitation was the use of artificial materials in the experiment.

[Geertsma et al. \(1956\)](#), studied three types of displacement, cold-water drive, hot-water drive, and solvent injection, by a combination of dimensional analysis and inspectional analysis, deriving the fundamental similarity groups for the displacement process.

**Craig et al. (1957)**, used scaled reservoir models (linear, uniform and non-uniform five-spot systems), to study the effect of gravity on oil recovery performance (volumetric sweep efficiency), in frontal drive displacements (water, gas or solvent flooding). Based on the inspectional analysis of differential equation for horizontal and vertical flow through an anisotropic formation, four scaling criteria were obtained.

**Rapoport et al. (1958)**, studied in scaled flow models, the effects of injection rate and of oil-to-water viscosity on oil recovery, developing a correlation between the recovery performance of linear and five-spot water floods. Furthermore, required numerical values of a scaling factor are shown in order to represent stabilized flooding behavior. **Perkins and Collins (1960)**, studied scaling criteria which allows different relative permeability and capillary pressure functions in the model and prototype (reservoir).

**Gaucher and Lindley (1960)**, observed the effects of rate and stratification on recovery for prototypes with different viscosity oils. Scaling criteria were applied in the model prototypes and useful experimental results are presented. **Henley et al. (1961)** performed scaled (dimensional and inspectional analysis) laboratory-model tests, to study the effects of several variables on a bottom-water drive process (well spacing, fluid mobility, rate of production, capillary and gravity forces, well penetration and well completion techniques). An important conclusion is that capillary forces do not affect the sweep efficiency and gravity effects must be considered.

**Mattax and Kyte (1962)** derived a dimensionless time for oil displacement by water imbibition in fractured reservoirs. This paper establishes that relative permeability and capillary pressure functions are matched in a scaled model if a core sample is used as the laboratory model. Another important conclusion is that total recovery for a fractured matrix, water-drive reservoir is independent of the production rate.

**Pozzi and Blackwell (1963)**, carried out several scaled laboratory models for studying miscible displacements and analyzed the principal features of the process, even though some scaling groups are not satisfied. They used a combination of inspectional and dimensional analysis, to interpret the recovery as a function of dimensionless parameters in molecular and convective diffusion. **Greenkorn (1964)**, established a useful general procedure by the combination of dimensional and inspectional analysis applying matrix calculus of the dimensions, to derive the scaling laws for miscible flow in porous media.

**Caudle and Silberberg (1965)**, studied the flow resistance in the aquifer in a two-permeability scaled laboratory model, simulating natural water drive (immiscible flow water-oil). Scaling groups were employed for analyzing geometrical similarity, operating flow conditions, and production history.

**Khan and Caudle (1969)**, realized laboratory experiments to simulate water drive in thin oil columns, obtaining a greater recovery for lower values of rate of production and mobility ratio. The results can be used to predict field performance. **Peters and Flock (1981)**, derived two important scaling groups by stability analysis of two-phase incompressible displacement in homogeneous porous media. The wettability average number values were 5.45 for a strongly oil-wet medium, and 306 for a strongly water-wet medium. The critical stability displacement number for the onset of instability is 13.56 for a coreflood experiment in a sand pack. **Kimber et al. (1988)** and **Kimber and Farouq Ali (1989, 1991)** developed and verified the scaling criteria for steam injection experiments, through dimensional and inspectional analysis of the partial differential equations of the process.

**Shook et al. (1992)**, developed a general procedure of inspectional analysis, that employs linear transformations and matrix analysis to obtain a minimum number of dimensionless groups (five groups) for scaling immiscible flow. The results were applied for predicting breakthrough oil recovery in waterflood process at the oil field scale.

**Peters et al. (1993)**, studied and scaled unstable immiscible laboratory corefloods, applying the concept of self-similar solutions and laboratory CT (computed tomography) imaging. The interpretation of water saturation results in oil-wet and water-wet media by a self-similar dimensionless variable, collapsed the experimental data in general dimensionless response curves. This paper was a change of paradigm in the scaling of displacements, due to the application of self-similarity theory from a generalized Buckley-Leverett mathematical model.

**Gharbi and Peters (1993)** continued the previously cited work (**Peters et al. (1993)**), with CT and numerical modeling for scaling a laboratory coreflood in a homogeneous medium, to forecast the performance in a heterogeneous reservoir generated geostatistically. Tests in sandpicks need to be scaled for reservoirs with high permeability variation and high correlation structure. The scaling of corefloods it is not needed for reservoirs having low permeability variation.

**Li and Lake (1995)**, presented a general method of scaling flow through heterogeneous media for an immiscible displacement (oil by water), based on statistical techniques and inspectional analysis. They divided the dimensionless groups into conventional scaling flow groups and heterogeneity scaling groups. **Kulkarni and Rao (2006)**, studied Gas-Assisted Gravity Drainage through a comparison of laboratory scaled experiments and field applications by pure dimensional analysis.

**Trivedi and Babadagli (2008)**, applied inspectional analysis methodology (**Shook et al. (1992)**) for scaling miscible displacement, in a simulated fractured media (Berea sandstone longitudinally cut in two pieces). The paper proposed and validated the matrix-fracture diffusion number, which is a ratio of viscous forces by flow in the fracture to diffusive forces in the matrix. An efficient recovery/solvent injection is in the range  $2 \times 10^7 - 3.5 \times 10^7$  of matrix-fracture diffusion number.

**Khandoozi et al. (2020)**, applied the inspectional analysis method developed by **Shook et al. (1992)**, combined with dimensional analysis for a numerical study of low salinity waterflooding.

There are few works in the literature about the determination of residual oil saturation by immiscible displacement, at laboratory scale in real fractured rocks under high pressure and temperature conditions. **Moreno et al. (2010)**, determined the residual oil saturation in a large unconsolidated core with live oil field at reservoir conditions (high pressure and temperature) by oil by water displacement. X-ray and CT scanning were employed for monitoring the process. An average value of residual oil saturation of 0.30 was obtained.

**Avila and Samaniego (2015)**, estimated the residual oil saturation in the gas cap of a naturally fractured reservoir by scaling (inspectional analysis) an oil by gas immiscible displacement, in a reservoir native fractured rock at reservoir conditions (high pressure and temperature). A useful practical dimensionless time expression was derived. **Teklu et al. (2013)**, presented an excellent review of field cases on methods for determining residual saturation. An important conclusion was that core analysis is one of the best methods for the determination of residual oil saturation at laboratory scale.

## 4.7 Experimental design

It is clear from the literature review, that no work has been reported to quantify the residual oil saturation in the fracture and matrix of a native rock of a naturally fractured reservoir, under a variable condition of effective stress and high temperature.

To estimate the residual oil saturation in the region invaded by water in the naturally fractured reservoir A, a native fractured rock (whole core) of the field was used, for the development of immiscible displacement oil by water (experimental simulation of aquifer advance). Corefloods were performed at representative reservoir conditions of high pressure and temperature (effective stress range  $2000 \text{ psi} \leq p \leq 7000 \text{ psi}$  and  $120^\circ\text{C}$ ). The displacement was carried out in two stages, an effective stress stage in which the oil contained in the secondary porosity (fractures and vugs) system is displaced, fractures are open and represent the main conducts of immiscible fluid flow. Stage 1 ends when only water is recovered. In combination with effective porosity data, it is possible to estimate the remanent oil saturation in fractures. The second stage corresponds to the continuation of the displacement with high effective stress where the rock has pseudo-matrix characteristics and the secondary porosity is mainly closed due to compaction. The effective stress influence and compaction are studied in Chapter 3. In this stage, the flow channels of the first stage are closed and the displacing fluid (water) moves the oil contained in the porous pseudo-matrix, increasing the recovery of stage 1.

Based on the experimental works carried out by [Craig et al. \(1957\)](#), [Henley et al. \(1961\)](#) and [Mattax and Kyte \(1962\)](#), it is considered that the relative permeability functions and capillary pressure functions are matched automatically if a representative core sample from the reservoir is used as the laboratory model. A representative sample should have the same wettability and relative permeability characteristics as the reservoir prototype. The full diameter rock used in this work is a representative sample, because the oil wettability was restored.



The complete methodology employed for developing the displacements is presented next. The procedure includes connate water saturation, core aging with field oil, scaling displacement time, the variation of the applied effective stress, interpretation of results based on dimensionless numbers and estimation of residual oil saturation in the invaded zone by the aquifer. A complete scaled experimental displacement for estimating residual oil saturation in field A is given by the superposition of two displacements, one for the gas cap and another for the invaded water zone (Fig. 4.3).

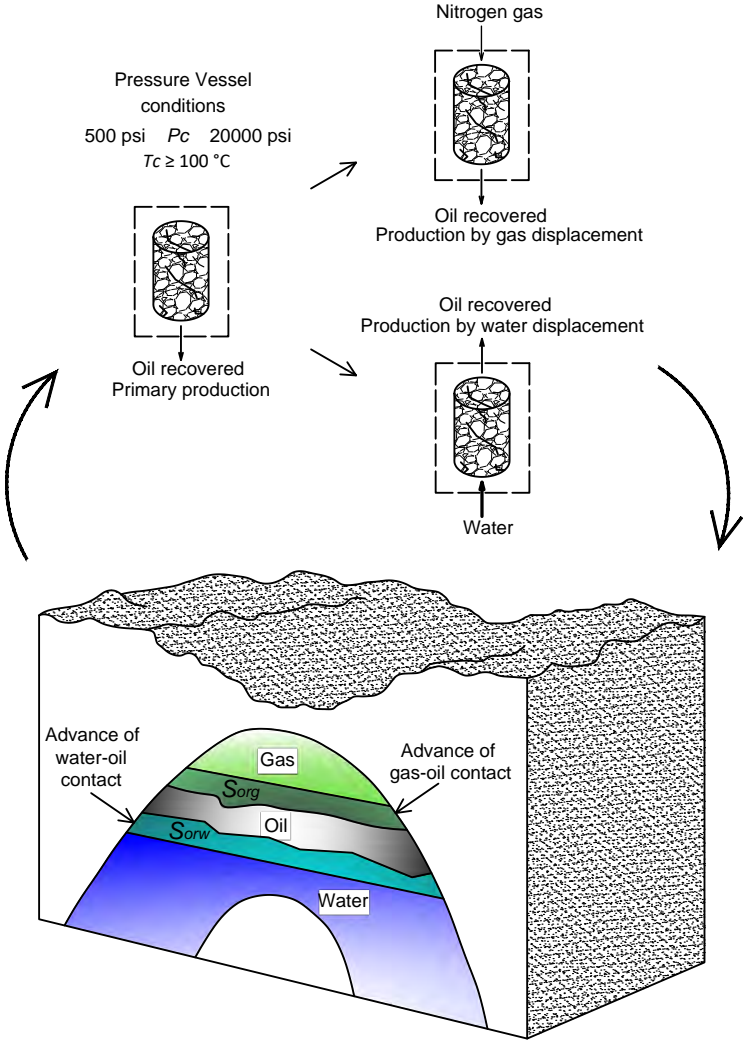


**Fig. 4.3:** Complete scaled experimental displacement for estimating residual oil saturation in a secondary porosity whole core sample.

## 4.8 Experimental methodology

The procedure can be divided into two parts; determination of basic petrophysical properties (bulk porosity, effective porosity, and permeability) and special core analysis for the modeling of complex properties (compressibility, permeability tensor, wettability, and residual oil saturation). The full methodology was designed under the recommended practices for core analysis [API-RP-40 \(1998\)](#). Specific technical details of the experimental procedure are documented in the thesis of [Herrera \(2000\)](#). Two immiscible displacements were developed for determining the residual oil saturation in the fracture and matrix systems. This concept is illustrated in Fig. 4.4.

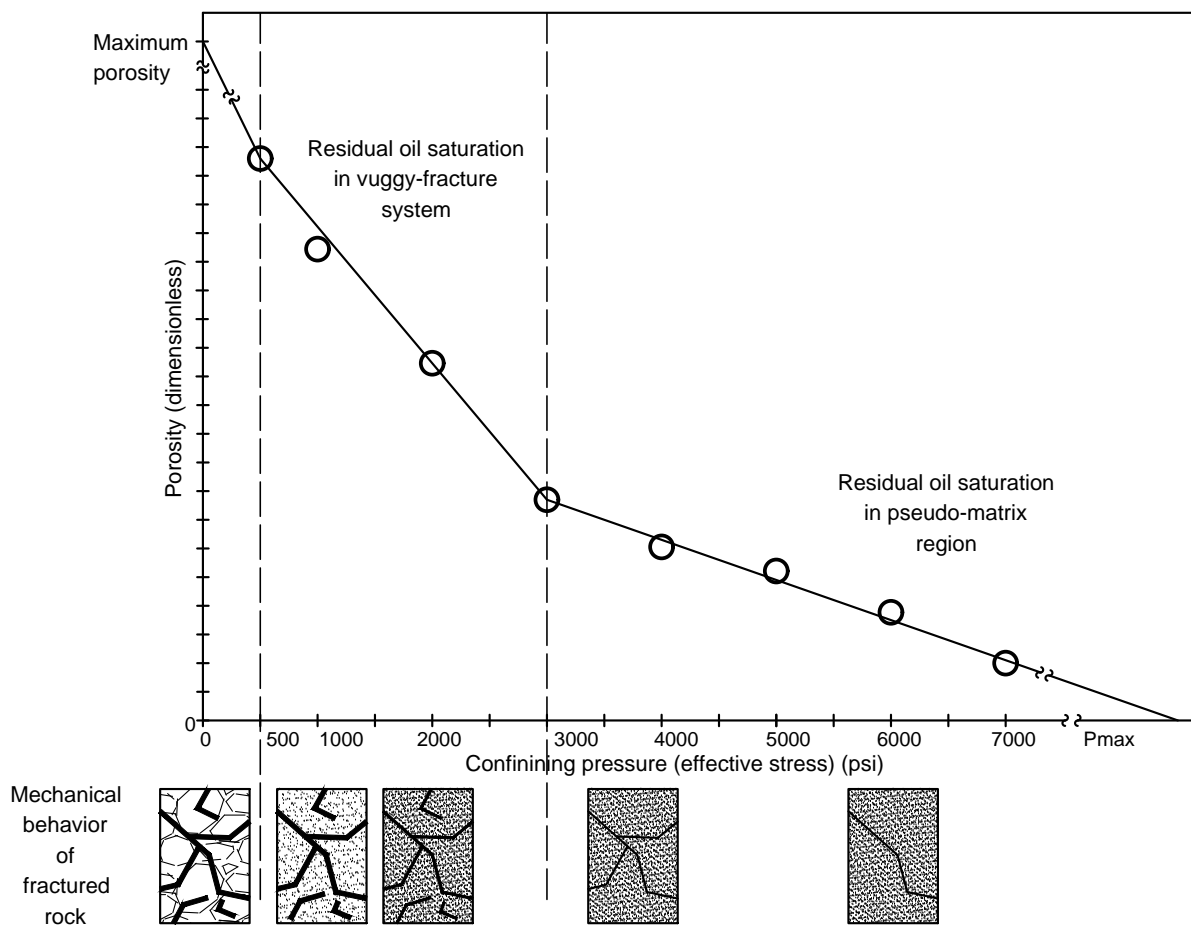


**Fig. 4.4:** Distribution of residual oil saturation in full diameter fractured rock.

The core was selected based on its measured petrophysical properties (porosity, permeability, and wettability) and according with classification of chapter 2. The sample has a natural system of double porosity and is native from field A. The full diameter sample has significant large scale heterogeneities that are different from the average matrix properties. The vugs and fractures can have a significant positive impact on rock porosity and permeability, and the relative proportion of vugs-fractures-to-matrix rock permit the realization of the advanced petrophysical residual oil saturation test. The procedure for developing the test is as follows:

#### **4.8.1 Sample cutting and trimming**

The full diameter sample should be cut and trimmed to provide a regularly shaped sample (cylinder). The cutting process is complicated, due to the implicit risk in the destruction of the sample, and the negative effects on the mechanical integrity of the rock. Fig. 4.5 shows the typical cut process.



**Fig. 4.5:** Cut sections of the core selected.

**Table 4.1:** Dimensions and weight of the full diameter samples.

Sample	Type of rock	Diameter (cm)	Lenght (cm)	Weight (gr)
A-1	VII	10.16	13.20	2553.69

The type of rock according to classification in Chapter 2, weight and operative dimensions of the sample after the cutting process are listed in Table. 4.1. The fractured full diameter sample is shown in Fig. 4.6.

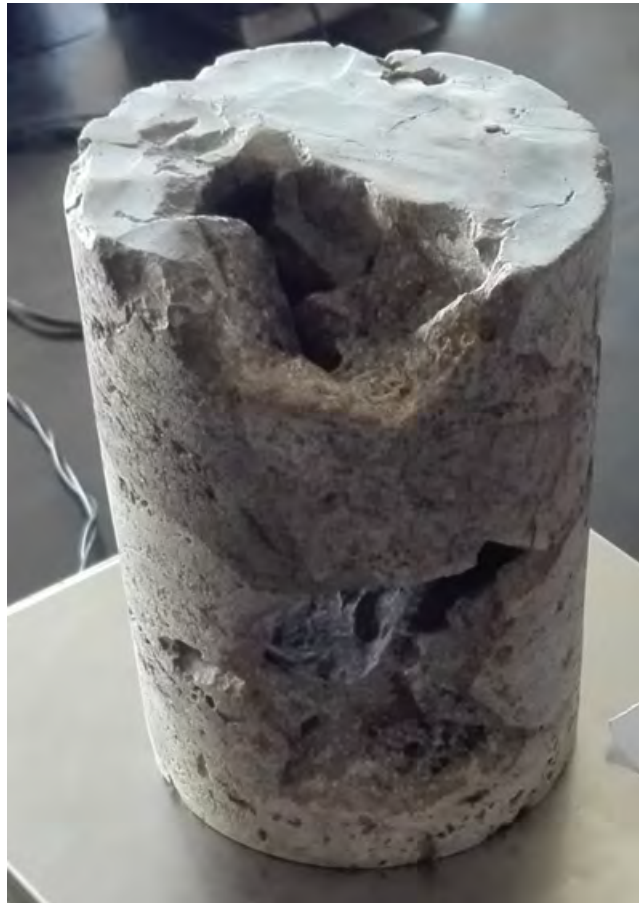


**Fig. 4.6:** Full diameter sample A-1.

## 4.8.2 Core cleaning and drying

The process is developed with a distillation extraction method (Dean Stark). The average duration of this process is 30 days. The cleanliness of the sample is best determined from the color of the solvent that siphons periodically from the extractor (Fig. 4.7). The solvents employed are a combination of 50 % toluene (oil solubility) and 50 % metanol (water and salt solubility). This combination has been found to be excellent for Gulf of Mexico heavy and light oils contained in carbonate rocks. After the cleaning step, the samples were dried in a conventional oven at 120 °C until the weight is constant.



**Fig. 4.7:** Cleaning of a full diameter sample for an average of 30 days.

### 4.8.3 Bulk porosity, effective porosity, compressibility and permeability data

In this section the results are presented of total porosity, effective porosity, compressibility, and vertical permeability of the sample. The permeability was determined along the orthonormal principal axis of the permeability tensor, however, only the vertical permeability data were employed because of the physical requirement of the reservoir process. The displacements at the laboratory scale simulate the vertical advance of the bottom water drive, at reservoir conditions.

The total bulk porosity was determined by Boyle's law method, with a gas helium porosimeter for full diameter sample. The results are shown in Table. 4.2. The values obtained are representative of carbonate rocks. This value is the maximum porosity in the fractured rock at laboratory conditions of pressure and temperature, and it is a reference in conjunction with the effective porosity values for calculating the compressibility of the rock.

In the next figures results are presented of the effective porosity and permeability as a function of variable confining pressure and a temperature of 120 °C. The effective porosity was determined with a combination of a gas helium porosimeter and a high-pressure vessel. The values of fracture porosity and matrix porosity were calculated (Table. 4.3, Fig. 4.8). Furthermore, fracture compressibility and matrix compressibility values were estimated (Table. 4.4). The procedure for the determination of permeability (Table. 4.5, Fig. 4.9) has been described in Chapter 3.

**Table 4.2:** Total bulk porosity of the full diameter sample A-1.

Sample	Bulk Porosity (dimensionless)
A-1	0.24

**Table 4.3:** Effective porosity of the sample A-1.

Effective Porosity		
Rock volume: 1070.1687 cm <sup>3</sup>		
Confining pressure $p_c$ (psi)	Pore volume $V_p$ (cm <sup>3</sup> )	Porosity (dimensionless)
500	143.831	0.1344
1000	114.080	0.1066
1500	101.452	0.0948
2000	97.171	0.0908
3000	91.392	0.0854
4000	80.477	0.0752
5000	60.679	0.0567

The compressibility values for fracture and matrix reported in Table. 4.4 are typically high in comparison with sandstone rocks, due to the secondary porosity characteristics of the rock and the ductility of the rock under high pressure and temperature conditions over during the realization of the test. These features contribute to obtaining a high recovery of fluids during the immiscible displacement of oil by water, because the high compressibility and compaction effect produced by the application of hydrostatic stress and pore pressure in the fractured porous rock. The values of compressibility were determined by the average slopes of the straight lines in Fig. 4.8, and the reference maximum value of porosity reported in Table. 4.2.

**Table 4.4:** Compressibility of the sample A1.

Compressibility	
Fracture compressibility $C_f$ (psi <sup>-1</sup> )	Matrix compressibility $C_m$ (psi <sup>-1</sup> )
121.12 x 10 <sup>-6</sup>	47.36 x 10 <sup>-6</sup>

Fig. 4.8 shows the tendency of effective porosity as a function of confining pressure for the fractured rock Sample A. The graph shows two linear reduction trends of effective porosity, similar behavior to permeability as a function of stress. The interpretation of the data using straight lines allows us to identify the double mechanical behavior of fractured rocks. The graph shows a rapid decrease in porosity from 0.24 to 0.13, in the range of  $0 \text{ psi} \leq p \leq 500 \text{ psi}$ , this reduction was generated due to the seal produced by the confining hydrostatic pressure. In the interval of  $500 \text{ psi} \leq p \leq 2000 \text{ psi}$ , the linear function of decreasing porosity corresponding to secondary porosity (vugs and fractures) is observed, the change in behavior occurs at a confining pressure value of 2000 psi, due to the intense sample fracturing. In the range  $2000 \text{ psi} \leq p \leq 5000 \text{ psi}$ , the linear behavior corresponding to the primary porosity (pseudo-matrix) is predominant, obtaining a porosity value of 0.056 for a confining pressure of 5000 psi.

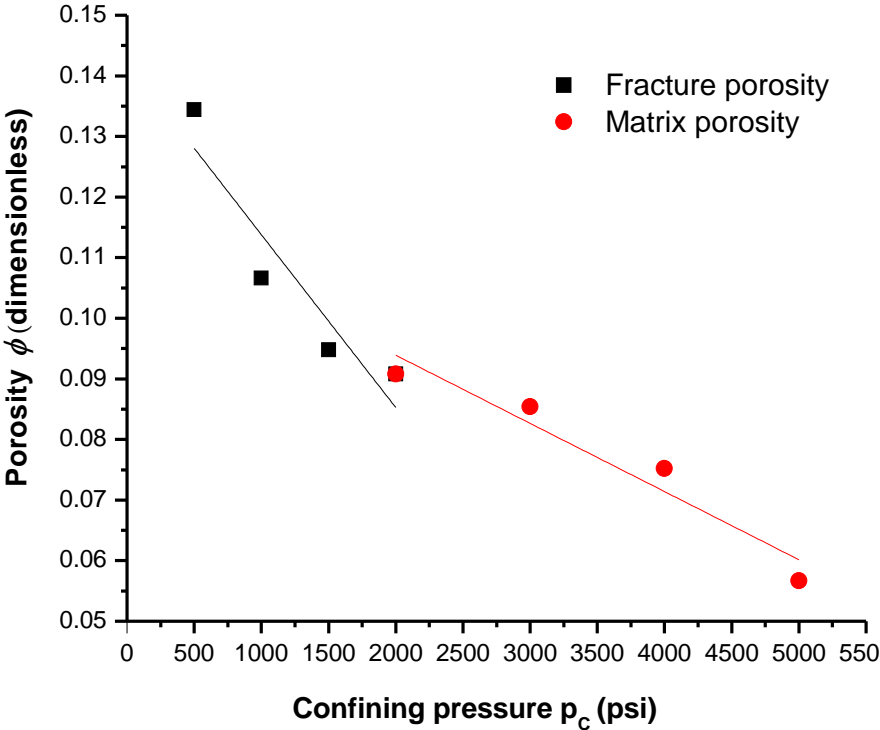
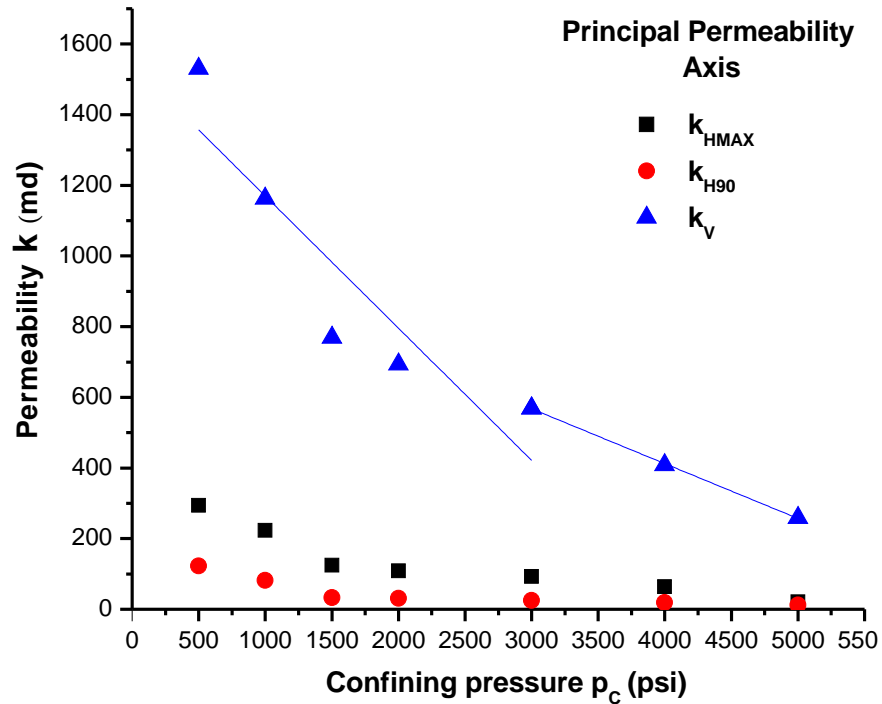


Fig. 4.8: Effective porosity as a function of confining pressure, sample A-1.



**Table 4.5:** Principal values of permeability of the sample A-1.

Permeability			
$p_c$ (psi)	$k_{MAX}$ (md)	$k_{H90}$ (md)	$k_v$ (md)
500	294.034	122.882	1530.948
1000	223.420	81.518	1162.910
1500	124.928	33.042	769.476
2000	108.448	30.524	693.676
3000	93.036	24.586	569.198
4000	63.410	18.530	408.378
5000	20.964	11.564	258.990



**Fig. 4.9:** Permeability as a function of confining pressure, sample A-1.

#### 4.8.4 Wettability

The wettability of the samples was determined by the dynamic Wilhelmy method. The experimental method is a qualitative and quantitative measurement of wettability. Thin sections rocks were obtained from the full diameter cores for the realization of the experiments. The dimensions of the sections are approximately 5.0 cm x 2.5 cm x 4 mm. The sections were aging with Fiel A native oil for 30 days, to restore the oil wettability expected in this carbonate naturally fractured reservoirs. A contact angle value of 40° was estimated. The thin section and the experiment performed at laboratory conditions of pressure and temperature are shown in Fig. 4.10. The figure presents the advance of the section with constant velocity in a hydraulic oil-water (brine) interface, the form, and direction of the meniscus indicates a preferential wettability to oil for the rock.

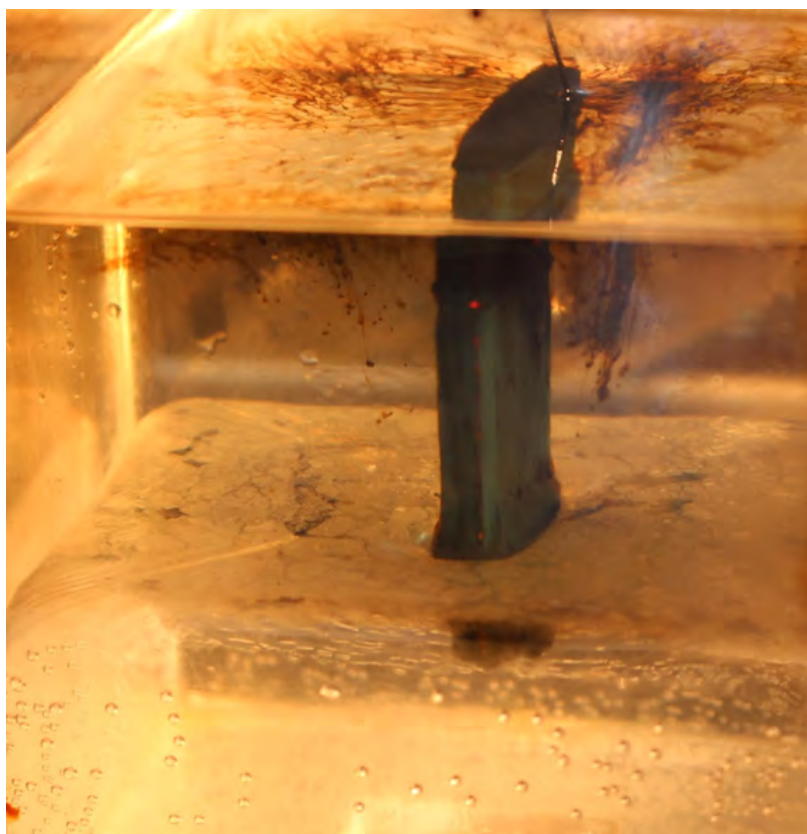


**Fig. 4.10:** Wettability behavior of the thin section rock extracted from sample A-1.

### 4.8.5 Fluids saturation

It is of fundamental importance to represent the same saturation and distribution of fluids at the core scale as in the formation. The sample was packed in rubber sleeve and mounted in the high-pressure vessel; the assembly is shown in Fig. 4.11. The complete permeameter equipment, with the high-pressure vessel, back pressure module, pressure gauges module, gas flow meters, and the external mechanical pump, is shown in Fig. 4.12. The first step is a water drainage displacement in the sample under a confining pressure of 1000 psi in the high-pressure vessel. The injection fluid is a synthetic water (brine) with a salinity of 50,000 ppm, by a mechanical pump and a pressure injection of 300 psi. Ten pore volumes were displaced in the sample.



**Fig. 4.11:** Assembly for core mounting in the high-pressure vessel.



**Fig. 4.12:** High-pressure and high temperature permeameter, for full diameter samples.

The goal of this experimental stage is to establish hydrostatic equilibrium and thermodynamic equilibrium (capillary equilibrium), of the two-phase system as a result of the imbibition of the wetting fluid (oil) to represent reservoir conditions corresponding to the A field. It was assumed that phase distribution during the saturation variation is quasistatically established, through the slowly pushing aside of the displaced water by displacing oil. An aging period of 20 days was applied for the sample, to reach the hydrostatic equilibrium; all the saturation changes occur in a quasi-static (equilibrium) way and are independent on the fluid displacement history. Next, water is displaced by an oil forced imbibition until connate water is reached. The value of the connate water is listed in Table. 4.6.

**Table 4.6:** Experimental value of connate water after a mechanical forced imbibition by reservoir A oil.

Sample	Connate water saturation (dimensionless)
A-1	0.18

#### 4.8.6 Scaling and geomechanical dimensionless time

To represent the water-oil contact advance and estimate the residual oil saturation, it is necessary to scale the coupled fluid flow process with the geomechanical field behavior to laboratory scale. It is necessary to calculate the velocity of the waterfront in the full diameter rock for developing the experiment; the length of the rock sample is known, therefore it is required to calculate the characteristic time for the realization of the displacements. The effective stress condition affects the core and reservoir properties; for this reason, it is necessary to calculate two characteristic times, the characteristic time for the first displacement in the fractured rock condition, and the characteristic time for the second displacement corresponding to the pseudo-matrix rock condition.

According to experimental facts, the characteristic time can be expressed by the next function (Eq. 4.1):

$$t_c = f(S, P_p, k, \phi, \sigma, \mu_w, L_c) \quad (4.1)$$

where,  $S$  is the overburden stress,  $P_p$  is the pore pressure,  $k$  is the permeability,  $\phi$  is the effective porosity,  $\sigma$  is the interfacial tension,  $\mu_w$  is the viscosity of the displacing water, and  $L_c$  is the characteristic length.

The time function can be simplified considering the stress ratio acting in the porous rock  $\Pi_s = S/P_p$ , and the ratio  $k/\phi$ , that represents an intrinsic geometrical property of the porous media (Eq. 4.2) :

$$t_c = f\left(\frac{S}{P_p}, \frac{k}{\phi}, \sigma, \mu_w, L_c\right) \quad (4.2)$$

That can be written like (Eq. 4.3):

$$t_c = \Phi(\Pi_s) * f\left(\frac{k}{\phi}, \sigma, \mu_w, L_c\right) \quad (4.3)$$

where  $\Phi(\Pi_s)$  is a dimensionless function of the stress ratio.

The function can be obtained following the rules of dimensional analysis. With reference to a  $LMT$  (length, mass and time) class of units (Barenblatt (2003)), the dimensions of the quantities of interest in the function are:

$$\begin{aligned} [t_c] &= T; & [S] &= [P_p] = \frac{M}{LT^2}; & \left[ \frac{S}{P_p} \right] &= 1; \\ \left[ \frac{k}{\phi} \right] &= L^2; & [\sigma] &= \frac{M}{T^2}; & [\mu_w] &= \frac{M}{LT}; & [L_c] &= L \end{aligned} \quad (4.4)$$

Then  $t_c$  can be expressed as product of powers of the dimensions of the governing parameters in Eq. 4.5:

$$t_c = \left( \frac{k}{\phi} \right)^a (\sigma)^b (\mu_w)^c (L_c)^d \Phi(\Pi_s) \quad (4.5)$$

Finding the exponents in the last equation, we obtain Eq. 4.6:

$$t_c = \left( \frac{k}{\phi} \right)^{-\frac{1}{2}} \frac{\mu_w L_c^2}{\sigma} \Phi(\Pi_s) \quad (4.6)$$

It is important to mention that the quantity  $\sqrt{k/\phi}$  is the characteristic size of a pore channel in the matrix rock, or the characteristic size of a fracture channel in the sample.

Defining a linear dimensionless function of the stress ratio, the following expression for the characteristic time is derived (Eq. 4.7)

$$t_c = \left( \frac{k}{\phi} \right)^{-\frac{1}{2}} \frac{\mu_w L_c^2}{\sigma} \left( \frac{P_p}{S} \right) \quad (4.7)$$

A dimensionless time parameter  $\Pi_t$  is obtained (Eq. 4.9)

$$\Pi_t = \frac{t_c}{\left( \frac{k}{\phi} \right)^{-\frac{1}{2}} \frac{\mu_w L_c^2}{\sigma} \left( \frac{P_p}{S} \right)} \quad (4.8)$$

$$\Pi_t = \sqrt{\frac{k}{\phi}} \left( \frac{\sigma}{\mu_w L_c^2} \right) \left( \frac{S}{P_p} \right) t_c \quad (4.9)$$

The expression can be defined as a geomechanical dimensionless time because of the nature of the quantities involved, which includes fluid flow and stress variables that affects the mechanical behavior of the rock.

The geomechanical dimensionless parameter is a generalization of the dimensionless time derived by **Mattax and Kyte (1962)**, which includes the effects of the overburden stress and the pore pressure in the porous media. The stress ratio is a dimensionless measure of effective stress acting in the rock.

Homologous times for the representative and native full diameter rock sample (model) and the naturally fractured reservoir (prototype), can be related as follows (Eq. 4.12):

$$\Pi_{t\_sample} = \Pi_{t\_reservoir} \quad (4.10)$$

$$\sqrt{\frac{k}{\phi}} \left( \frac{\sigma}{\mu_w L C^2} \right) \left( \frac{S}{P_p} \right) t_c \Big|_{sample} = \sqrt{\frac{k}{\phi}} \left( \frac{\sigma}{\mu_w L C^2} \right) \left( \frac{S}{P_p} \right) t_c \Big|_{reservoir} \quad (4.11)$$

$$t_{c\_sample} = \frac{\sqrt{\frac{k}{\phi}} \left( \frac{\sigma}{\mu_w L C^2} \right) \left( \frac{S}{P_p} \right) t_c \Big|_{reservoir}}{\sqrt{\frac{k}{\phi}} \left( \frac{\sigma}{\mu_w L C^2} \right) \left( \frac{S}{P_p} \right) \Big|_{sample}} \quad (4.12)$$

**Table 4.7:** Characteristics of the model (core) and the prototype (reservoir).

Characteristic	Core sample	Prototype reservoir
Size, $L$	13.20 cm	629 m
Fracture porosity, $\phi_f$ (dimensionless)	0.0948	0.0850
Matrix porosity, $\phi_m$ (dimensionless)	0.0752	0.0376
Fracture permeability, $k_{f_i}$ (dimensionless)	769.48	2000
Matrix permeability, $k_{m_i}$ (dimensionless)	569.20	900
Water density, $\rho_w$ (gr/cm <sup>3</sup> )	1.027	1.027
Oil density, $\rho_o$ (gr/cm <sup>3</sup> )	0.93	0.765
Water viscosity, $\mu_w$ (cp)	2.91	2.50
Oil viscosity, $\mu_o$ (cp)	18	12
Interfacial tension, $\sigma$ (dyne/cm)	45	35
Connate water saturation, $S_{wi}$ (dimensionless)	0.180	0.114

The most important factors for the analysis of the physical similitude of the model (core) and the prototype (reservoir), are listed in Table. 4.7. The field data about the advance of the oil-water contact is presented in Table. 4.8.

**Table 4.8:** Oil-water contact of field A.

Year	Time interval (year)	Depth (m)	Depth interval (m)
1979	37	3221	629
2016		2592	
Average velocity (m/year)		17.00	



To calculate the characteristic time for the realization of the displacement, it is necessary to estimate the characteristic length for the reservoir scale. In the case of the laboratory scale, the characteristic length can take the value of the length of the core. The characteristic length for the reservoir scale it is a magnitude that represents the physical sense of the flow of fluids in the rock. In this case for a naturally fractured reservoir, it is possible to obtain two characteristic lengths, one for the condition where the fluid dynamics is predominant in the fractures (secondary porosity), the other, when the fractures are collapsed or closed and the matrix and vertical permeability provides the principal production of fluids from the reservoir. By increasing the effective stress in the reservoir as a result of fluid extraction, the secondary porosity with horizontal orientation is mainly closed by the overburden pressure, however, the vertical permeability remains open. Furthermore, the mentioned lengths can be interpreted as the sizes of the matrix blocks in the naturally fractured reservoir A. The characteristic lengths can be estimated with dimensional analysis; the next relation (Eq. 4.13) was employed (Barenblatt et al. (1990)):

$$L_c \sim \frac{\sqrt{k\phi}}{\Pi_c} \quad (4.13)$$

Where  $\Pi_c$  is the capillary number. With the data of Table. 4.7 and Table. 4.8, the value of the capillary number for the reservoir was calculated:

$$\Pi_c = 3.85 \times 10^{-8} \quad (4.14)$$

The characteristic lengths obtained are reported in Table. 4.9.

**Table 4.9:** Representative characteristic lengths for reservoir scale.

Lenght type	Characteristic length (m)
Predominant vuggy-fracture permeability	10.64
Predominant pseudo-matrix permeability	4.75

**Table 4.10:** Values of stresses for the reservoir at depth of 1900 m.

Mechanical state	Type stress	Stress value (psi)
Vuggy-fracture system predominant in the production	Overburden	6232
	Pore pressure	4000
	Effective stress	2232
Pseudo-matrix system predominant in the production	Overburden	6232
	Pore pressure	1000
	Effective stress	5232

Table. 4.10 shows the numerical values required for the calculation of the geomechanical time of the overburden stress, pore pressure, and effective stress, for field-scale with the expected respective mechanical states of the reservoir, and the equivalent values for laboratory-scale experiments are reported in Table. 4.11. The values of the stresses corresponding to laboratory-scale are numerically lower than the field scale stresses, it is possible to perform the displacement at the same stress conditions of reservoir scale, however, it is not imperative and necessary because of the scaling procedure.

**Table 4.11:** Values of stresses for the core at laboratory scale.

Mechanical state	Type stress	Stress value (psi)
Vuggy-fracture system predominant in the production	Overburden	2500
	Pore pressure	1000
	Effective stress	1500
Pseudo-matrix system predominant in the production	Overburden	4000
	Pore pressure	1000
	Effective stress	3000

**Table 4.12:** Characteristic times and velocities for the core displacements.

Displacement	Time	Characteristic velocity
First displacement	1 hour 18 min	$2.83 \times 10^{-3}$ (cm/s)
Second displacement	16 hour 58 min	$2.16 \times 10^{-4}$ (cm/s)

With the available data presented in Tables 4.7, 4.8, 4.9, 4.10, and 4.11 the resultant geomechanical times and the characteristic velocities in the core for developing the displacements are listed in Table. 4.12.

#### **4.8.7 First displacement (Residual oil saturation in vuggy-fracture-matrix system)**

Next, the intrusion of water by the aquifer effect (advancement of the water-oil contact) was reproduced at laboratory scale, by the immiscible displacement oil-water in the vertically upward direction. In this stage, effective stress of 1,500 psi (2,500 psi overburden pressure and 1,000 psi pore pressure) was applied, conditions under which fracture permeability (vuggy-fracture system) has been determined to be mechanically open.

The injection rate of the displacing fluid calculated was 23.20 cm<sup>3</sup>/min, at the reservoir temperature of 120°C. During the development of the displacement test, a record and monitoring of the inlet and outlet pressures of the vessel, volumes of produced fluids, temperature, confining pressure, and back-pressure were controlled and measured.

The experiment was considered completed when only the water displacing phase was recovered, which corresponds to zero oil production.

The production data and residual oil saturation in the vuggy-fracture-matrix system are reported in Tables 4.13 and 4.14 , Figs 4.13 and 4.14 . The variation in fluid production data, under constant hydrostatic stress condition and injection rate, is due to the complex nature and the nonhomogeneous properties of fractured rock (interaction vugs-fracture and pseudomatrix).

**Table 4.13:** Data of produced fluids during the first displacement in the sample A-1.

Pore volume injected $V_i$ (dimensionless)	Production rate of oil $q_o$ (cm <sup>3</sup> /hr)	Production rate of water $q_w$ (cm <sup>3</sup> /hr)	Oil recovery Q (% Percentage)
0.223	0.810	9.120	1.979
0.442	1.485	8.455	5.609
0.665	0.810	9.120	7.589
0.906	1.620	9.310	11.540
1.151	0.945	9.975	13.858
1.383	1.030	7.650	25.737
1.602	1.080	8.740	28.377
1.820	0.270	9.310	29.037
2.039	0.220	9.280	29.697
2.258	1.080	8.740	32.336
2.477	0.260	9.310	32.996
2.696	0.210	9.250	33.656
2.915	0.230	8.850	34.316
3.134	0.180	9.150	34.976
3.352	0.150	8.950	35.636

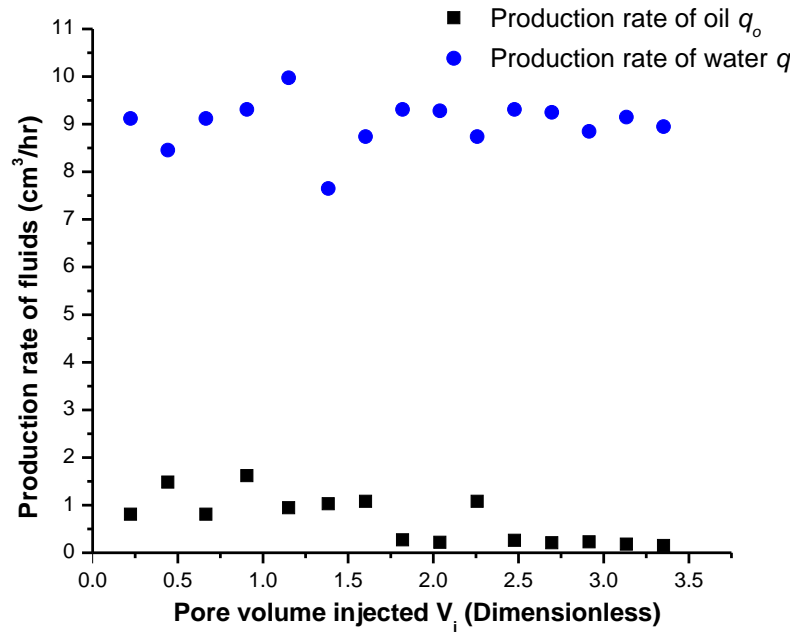


Fig. 4.13: First displacement, production of fluids in the sample A-1.

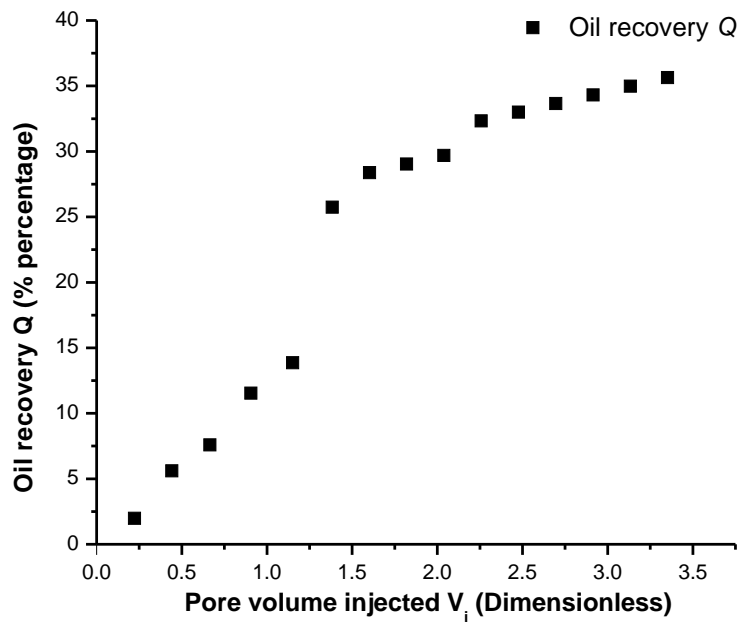


Fig. 4.14: First displacement, oil recovered in the sample A-1.

Quantification of the total residual oil saturation  $S_{ort}$  in the vuggy-fracture-pseudomatrix system is reported in Table. 4.14, the necessary experimental data are listed next:

Pore volume,  $V_p = 101.45 \text{ cm}^3$

Connate water saturation,  $S_{wi} = 18.26 \text{ cm}^3$

Oil saturation volume,  $V_o = 83.19 \text{ cm}^3$

Oil displaced produced,  $V_{op} = 43.26 \text{ cm}^3$

The next result was obtained:

$$S_{ort} = \frac{V_o - V_{op}}{V_p} = \frac{83.19 - 43.26}{101.45} = 0.3935 \quad (4.15)$$

$$S_{ort} = 39.35\% \quad (4.16)$$

The obtained value of residual oil saturation in this displacement stage corresponds to the total oil residual saturation in the rock. In this displacement, the water flows predominantly in the secondary porosity, with little contribution of the primary porosity. The major proportion of oil was recovered in this stage. The displacement was finished when only water was recovered, however, with the increment in the effective stress, flow of oil was produced by the pseudomatrix to the partially closed vugs and fractures. This transfer of oil can be considered the residual oil saturation in the secondary porosity  $S_{orf}$ .

**Table 4.14:** First displacement. Residual oil saturation in the sample A- 1.

Sample	$S_{or}$ (% Percentage)	Displacing fluid
A-1	39.35	Water

#### 4.8.8 Second displacement (Residual oil saturation in the pseudo-matrix system)

The production data and residual oil saturation in the pseudo-matrix system are reported in Tables 4.15 and 4.16, and Figs 4.15 and 4.16. Next, after the first displacement had finished, the effective stress was incremented to a mechanical state of pseudo-matrix in the rock. In the first stage, the fluid transfer of matrix to the vuggy-fracture system was minimum, because the water displaced oil in the preferential flow channels (vugs and fractures).

**Table 4.15:** Data of produced fluids during the second displacement in the sample A- 1, under an effective stress of 3000 psi.

Pore volume injected $V_i$ (dimensionless)	Production rate of oil $q_o$ (cm <sup>3</sup> /hr)	Production rate of water $q_w$ (cm <sup>3</sup> /hr)	Oil recovery Q (% Percentage)
0.370	2.650	9.250	11.010
0.480	1.800	6.440	13.050
0.590	1.440	5.880	14.680
0.700	1.260	6.020	16.110
0.810	0.540	7.540	16.720
0.920	1.440	6.020	18.350
1.030	1.620	5.600	20.180
1.140	0.720	6.860	21.010
1.250	0.360	7.700	21.410
1.360	0.270	8.190	21.710
1.470	0.630	6.370	22.430
1.580	0.360	6.580	22.840

This fact was experimentally tested and is independent of the injection pressure, the most important factor is the mechanical state of the fractures (open or closed); this topic is studied in Chapter 3.

The confining pressure was incremented to 4000 psi; the pore pressure was maintained in 1000 psi, resulting in a value of 3000 psi of effective stress. With the experimental data, the behavior of the production of fluids, oil recovery factor and residual oil saturation in the pseudo-matrix medium was obtained.

The variation in fluid production data showed in Fig. 4.15, under constant hydrostatic stress condition and injection rate, in the same case that the first displacement, is due to the collapsed secondary porosity (vugs and fractures) and the mechanical transformation to a pseudomatrix rock.

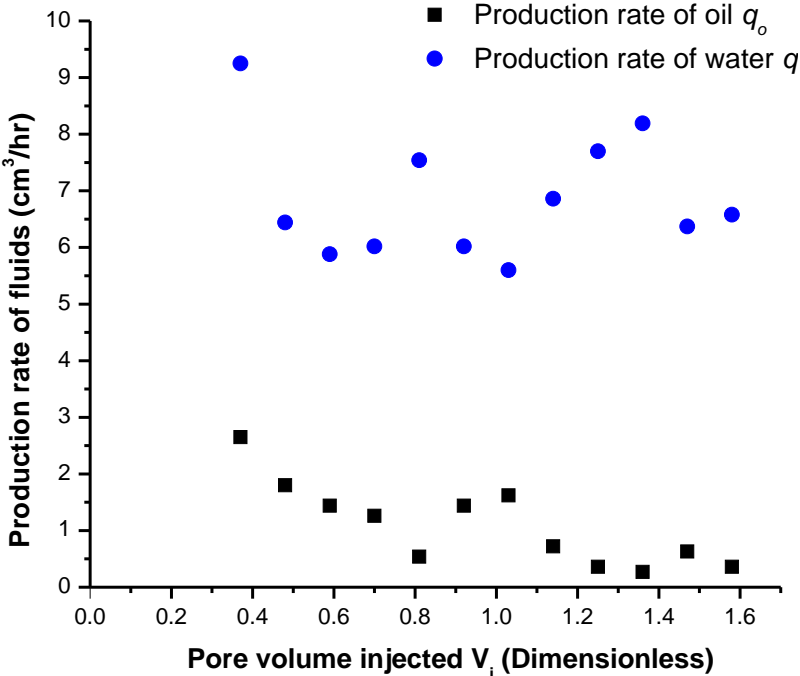
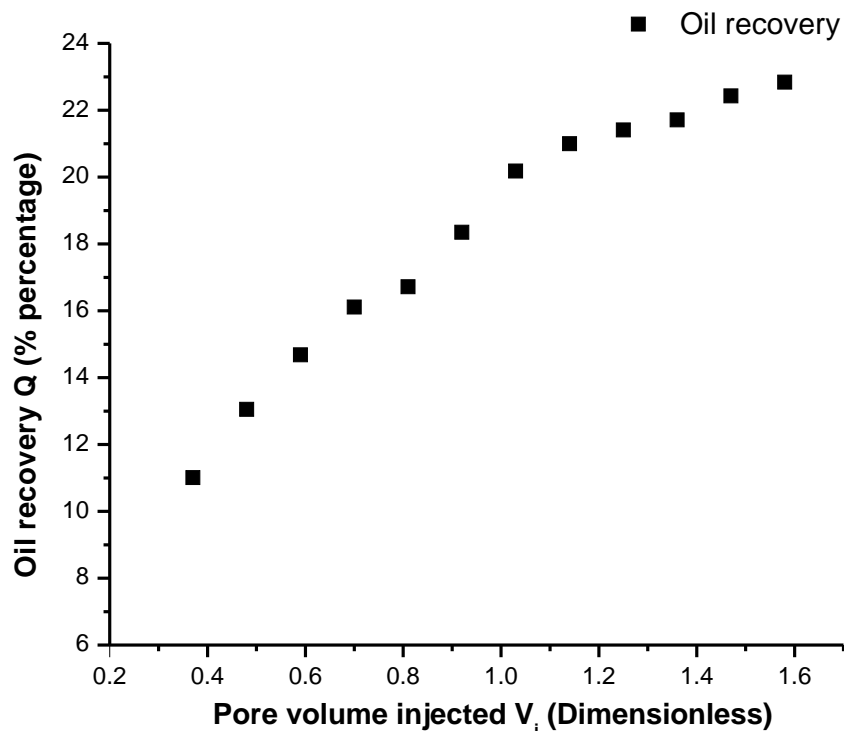


Fig. 4.15: Second displacement, production of fluids in the sample A-1.



The time required for the second displacement was 16 hr 58 min, approximately 15 hours longer than for the first displacement. This is due to the compaction of the rock and the collapse of the secondary porosity, since, by increasing the stress applied to the rock, the predominant flow channels in the first displacement were closed. This effect on the morphology of the rock allows a homogeneous sweep of the oil by the water in the rock matrix. The increase in the displacement time implies directly in the increment of the applied mechanical energy for developing the displacement, because of the high tortuosity in the rock. With the experimental results, an increase in oil recovery was obtained due to the second sweep in the pseudomatrix. This provides optimistic results for the field application of secondary and enhanced oil recovery processes in giant naturally fractured reservoirs with a high degree of depletion in the Gulf of Mexico.



**Fig. 4.16:** Second displacement, oil recovered in the sample A-1.

Quantification of the residual oil saturation in the pseudo-matrix  $S_{orm}$  in the core A-1 is reported in Table 4.16, the necessary experimental data for the estimation are listed next:

Pore volume,  $V_p = 91.39 \text{ cm}^3$

Connate water saturation,  $S_{wi} = 18.26 \text{ cm}^3$

Water saturation by first displacement,  $S_w = 33.30 \text{ cm}^3$

Oil saturation volume,  $V_o = 40.80 \text{ cm}^3$

Oil displaced produced,  $V_{op} = 18.50 \text{ cm}^3$

The next result was obtained:

$$S_{or} = \frac{V_o - V_{op}}{V_p} = \frac{40.80 - 18.50}{91.39} = 0.2440 \quad (4.17)$$

The next result was obtained:

$$S_{orm} = 24.40\% \quad (4.18)$$

The estimated value of residual oil saturation in the pseudo-matrix rock, is the final value obtained after the two displacements by water. The displacement finished when only water was recovered.

**Table 4.16:** Second displacement. Residual oil saturation in the sample A-1.

Sample	$S_{or}$ (% Percentage)	Displacing fluid
A-1	24.40	Water

#### 4.8.9 Discretization of the residual oil saturation in the pseudo-matrix and vuggy-fracture system

The residual oil saturation in the vuggy-fracture-matrix system satisfies the next equation:

$$\begin{aligned}
 S_{ort} &= S_{orm} + S_{orf} \\
 S_{orf} &= S_{ort} - S_{orm} \\
 S_{orf} &= 39.35\% - 24.40\% = 14.95\%
 \end{aligned}
 \tag{4.19}$$

Where  $S_{ort}$  is the residual oil saturation in the vuggy-fracture-matrix system,  $S_{orm}$  is the residual oil saturation in the pseudomatrix system (compacted vuggy-fracture-matrix system), and  $S_{orf}$  is the residual oil in the vuggy-fracture system.

It is observed from the results obtained after the two displacements that the largest portion of residual oil is stored in the pseudo-matrix medium. The final data are reported in Table 4.17.

A further contribution of this work, is the calculated time of displacement, compared to conventional services in the oil industry, and reported in the literature, the times for the development of immiscible displacements is very long, for example, in the paper of [Moreno et al. \(2010\)](#), the time for the development of a water displacement is approximately 333 hrs (14 days), and in other articles, the time is of the order of months ([Honarpour et al. \(2005\)](#)). The realization of laboratory experiments with very long displacement times does not imply the obtention of representative results for the reservoir scale.

**Table 4.17:** Distribution of residual oil saturation in the full diameter sample A-1.

Sample	$S_{ort}$ (% Percentage)	$S_{orf}$ (% Percentage)	$S_{orm}$ (% Percentage)
A-1	39.35	14.95	24.40

## 4.9 Physical similitude between model and prototype

The local equilibrium phase distribution in the rock, and the form of the relative permeability curves are dependent of the following characteristics of the rock and fluids: oil viscosity  $\mu_o$ , water viscosity  $\mu_w$ , permeability  $k$  (fracture permeability  $k_f$ , matrix permeability  $k_m$ ), interfacial tension  $\sigma$ , and the modulus of the flow velocity vector  $u = |\bar{u}|$ . Two independent dimensionless parameters can be constructed: The viscosity ratio  $\Pi_\mu = \mu_o/\mu_w$ , and the capillary number  $\Pi_c = \mu_w u/\sigma$ . The viscosity ratio characterizes the extent of the interaction between flowing phases and the capillary number characterizes the ratio of viscous and capillary forces on the pore scale. The physical effects of gravity and capillary forces can be measured by the gravity dimensionless number  $\Pi_g = \Delta\rho g H/\sigma$  (Barenblatt et al. (1990)). Like the capillary force, the gravity force is independent of displacement rate and will, therefore, manifest itself most strongly at low displacement rates, when the viscous and pressure forces are low (Peters et al. (1993)). These dimensionless numbers are considered the most relevant for the analysis of the oil-water contact advance and the physical similitude between model and prototype is reported in Table 4.18.

**Table 4.18:** Comparison of the dimensionless number between model and prototype.

Dimensionless Number	Mathematical expression	Full diameter sample fractured rock (model)	Naturally fractured reservoir (Prototype)
Capillary number	$c = \frac{\mu_w u}{\sigma}$	$1.30 \times 10^{-7}$	$0.38 \times 10^{-7}$
Gravity number (Barenblatt)	$g = \frac{\Delta \rho g H k^{1/2}}{\sigma}$	$2.69 \times 10^{-3}$	$328.42 \times 10^{-3}$
Gravity number	$g = \frac{\Delta \rho g k}{\mu_w u}$	0.12	1.69
Viscosity ratio	$\mu = \frac{\mu_o}{\mu_w}$	6.19	4.80

## 4.10 Concluding remarks

A novel experimental immiscible displacement test was designed to estimate the residual oil saturation in the vuggy-fracture and pseudo-matrix system, in a full diameter fractured rock sample. The key to the design is the nature of compaction in the rock described in Chapter 3 and is fundamental to understand the production of fluids and the residual oil saturation. The influence of temperature transforms the geomechanical behavior of the sample because of the ductility of carbonate rocks. The rock was classified according to Chapter 2.

With dimensional analysis, a dimensionless geomechanical time was obtained for each of the displacements. The expression is a generalization of the time of [Mattax and Kyte \(1962\)](#) , that includes a stress ratio. Also, the physical behavior of the displacement in the laboratory was compared with the reservoir behavior.

Furthermore, the complete experimental test is described step by step, and its application is easy in a petrophysics laboratory.

Finally, the discretization of residual oil saturation is of paramount importance for the implementation of improved oil recovery processes at the field scale.

# Chapter 5

## General Conclusions

This thesis presents the design of advanced experimental petrophysical tests to investigate the constitutive behavior of fractured rocks; the tests, and the data presented have been performed at reservoir conditions. The most relevant technical aspects discovered from the experiments are as follows:

The combined effects of stress and temperature can transform the morphology of the rock, by the compaction of the fracture network, until a pseudo-matrix state is reached. This transformation allows the discretized estimation of the most important petrophysical properties of the rock.

The representation by ellipses of the fracture network and matrix permeabilities have provided experimental evidence of the double physical behavior of fractured rocks. The fracture and matrix permeabilities mathematical matrices allow the permeability estimation at different values of effective reservoir stress. An average reservoir-scale permeability tensor can be experimentally determined employing experimental rock mechanics presented in this thesis complemented with statistical tools. The permeability tensor matrix can be considered the mathematical representation of the geomechanical behavior of the reservoir.

Therefore, it is possible to predict the behavior of the permeability tensor throughout the production period and to estimate the compaction of the reservoir and calculate the residual oil saturations. The experimental estimation of residual oil in vuggy-fractured rocks, can be extended and improved calculating the pressure variation (depressurization) through the scaling of the partial differential equations of immiscible flow, to obtain operational conditions for developing the displacement in one experimental run. Furthermore, using the production data and the effective stress condition, the matrix-fractures fluid transfer can be measured. The discussed procedure is applicable for the estimation of the residual oil saturation in the gas cap region.

The mathematical interpretation based on dimensional analysis is simple but very powerful application for scaling the experimental results in cores to field-scale behavior of naturally fractured reservoirs.

The compaction and flow constitutive behavior experiments described in this thesis are fundamental for the design of advanced tests for measuring capillary pressures, relative permeabilities, USBM test at reservoir conditions, prediction of future production of naturally fractured reservoirs, which are in the research and development process.

# Bibliography

- API-RP-40 (1998). *Recommended practices for core analysis*. Washington, DC: API, 2 edition.
- Avila, U. A. and Samaniego, F. (2015). Escalamiento de una prueba experimental para estimar la saturación residual de aceite, en la capa secundaria de un yacimiento naturalmente fracturado. *Ingeniería petrolera*, 55(05):250–263.
- Barenblatt, G. (2003). *Scaling*. Cambridge: Cambridge University Press.
- Barenblatt, G., Entov, V., and Ryzhik, V. (1990). *Theory of fluid flows through natural rocks*. Kluwer Academic Publishers.
- Bridgman, P. (1931). *Dimensional Analysis, revised edition*. New Haven, Connecticut: Yale University Press.
- Buckingham, E. (1914). On physically similar systems; illustrations of the use of dimensional equations. *Phys. Rev.*, 4(04):345–376. <http://dx.doi.org/10.1103/PhysRev.4.345>.
- Caudle, B. H. and Silberberg, I. H. (1965). Laboratory models of oil reservoirs produced by natural water drive. *SPE J.*, 5(01):25–36. <http://dx.doi.org/10.2118/984-PA>.
- Collins, R. E. (1952). Determination of the transverse permeabilities of large core samples from petroleum reservoirs. *Journal of applied physics*, 6(23):681–684. <https://doi.org/10.1063/1.1702278>.



- Craig, F., Geffen, T., and Morse, R. (1955). Oil recovery performance of pattern gas or water injection operations from model tests. *Petroleum Transactions, AIME*, 204(01):7–15. <https://doi.org/10.2118/413-G>.
- Craig, F. F., Sanderlin, J. L., and Moore, D. W. (1957). A laboratory study of gravity segregation in frontal drives. *Trans., AIME*, 210(01):275–282. <https://doi.org/10.2118/676-G>.
- Croes, G. A. and Schwarz, N. (1955). Dimensionally scaled experiments and the theories on the water-drive process. *Trans., AIME*, 204(01):35–42. <https://doi.org/10.2118/332-G>.
- Engelberts, W. F. and Klinkenberg, L. J. (1951). Laboratory experiments on the displacement of oil by water from packs of granular material. *3rd World Petroleum Congress, 28 May-6 June, The Hague, the Netherlands. WPC-4138*.
- Fitzgibbon, A., Pilu, M., and Fisher, R. B. (1999). Direct least square fitting of ellipses. *IEEE Transactions on Pattern Analysis and Machine Intelligence*, 21(5):476–480. <https://doi.org/10.1109/34.765658>.
- Gangi, A. F. (1978). Variation of whole and fractured porous rock permeability with confining pressure. *Int. J. Rock Mech. Min. Sci. Geomech. Abstr*, (15):249–257. [https://doi.org/10.1016/0148-9062\(78\)90957-9](https://doi.org/10.1016/0148-9062(78)90957-9).
- Gaucher, D. H. and Lindley, D. C. (1960). Waterflood performance in a stratified, five-spot reservoir – a scaled-model study. *Petroleum Transactions, AIME*, 219(01):208–215. <https://doi.org/10.2118/1311-G>.
- Geertsma, J., Croes, G. A., and Schwarz, N. (1956). Theory of dimensionally scaled models of petroleum reservoirs. *Trans., AIME*, 207(01):118–127. <https://doi.org/10.2118/539-G>.

- Gharbi, R. and Peters, E. (1993). Scaling coreflood experiments to heterogeneous reservoirs. *Journal of Petroleum Science and Engineering*, 10(02):83–95. [https://doi.org/10.1016/0920-4105\(93\)90033-B](https://doi.org/10.1016/0920-4105(93)90033-B).
- Greenkorn, R. A. (1964). Flow models and scaling laws for flow through porous media. *Ind. Eng. Chem.*, 56(03):32–37. <http://dx.doi.org/10.1021/ie50651a006>.
- Henley, D. H., Owens, W. W., and Craig, F. F. (1961). A scale-model study of bottom-water drives. *J Pet Technol*, 13(01):90–98. <http://dx.doi.org/10.2118/1539-G-PA>.
- Herrera, R. (2000). *Estudio petrofísico de muestras de diámetro completo con doble porosidad*. PhD thesis, School of Engineering, National Autonomous University of Mexico.
- Honarpour, M. M., Djabbarah, N. F., and Sampath, K. (2005). Whole core analysis - experience and challenges. *Society of Petroleum Engineers*, 8(06):127–133. <https://doi.org/10.2118/81575-PA>.
- Khan, A. R. and Caudle, B. H. (1969). Scaled model studies of thin oil columns produced by natural water drive. *SPE J.*, 9(03):317–322. <http://dx.doi.org/10.2118/2304-PA>.
- Khandoozi, S., Malayeri, M., Riazi, M., and Ghaedi, M. (2020). Inspectional and dimensional analyses for scaling of low salinity waterflooding (lswf): From core to field scale. *Journal of Petroleum Science and Engineering*, 189:1–23. <https://doi.org/10.1016/j.petrol.2020.106956>.
- Kimber, K. D. and Farouq Ali, S. M. (1989). Verification of scaling approaches for steam injection experiments. *Journal of Canadian Petroleum Technology*, 28(01):40–47. <https://doi.org/10.2118/89-01-03>.
- Kimber, K. D. and Farouq Ali, S. M. (1991). Scaled physical modeling of steam-injection experiments. *SPE Reservoir Engineering*, 6(04):467–469. <https://doi.org/10.2118/18751-PA>.

- Kimber, K. D., Farouq Ali, S. M., and Puttagunta, V. R. (1988). New scaling criteria and their relative merits for steam recovery experiments. *Journal of Canadian Petroleum Technology*, 27(04):86–94. <https://doi.org/10.2118/88-04-07>.
- Kulkarni, M. and Rao, D. (2006). Characterization of operative mechanisms in gravity drainage field projects through dimensional analysis. *SPE Annual Technical Conference and Exhibition, 24-27 September, San Antonio, Texas, USA*. <https://doi.org/10.2118/103230-MS>.
- Lei, G., Dong, P., Mo, S. Y., Yang, S., Wu, Z. S., and Gai, S. H. (2015). Calculation of full permeability tensor for fractured anisotropic media. *J. Petrol Explor Prod Technol*, 2(5):167–176. <https://doi.org/10.1007/s13202-014-0138-6>.
- Leung, W. F. (1986). A tensor model for anisotropic and heterogeneous reservoirs with variable directional permeabilities. *Soc. Petrol. Eng. J.*, (15134):405–420. <https://doi.org/10.2118/15134-MS>.
- Leverett, M. C., Lewis, W. B., and True, M. E. (1942). Dimensional-model studies of oil-field behavior. *Trans., AIME*, 146(1):175–193. <http://dx.doi.org/10.2118/942175-G>.
- Li, D. and Lake, W. (1995). Scaling flow through heterogeneous permeable media. *SPE Advanced Technology Series*, 3(01):188–197. <https://doi.org/10.2118/26648-PA>.
- Mattax, C. C. and Kyte, J. R. (1962). Imbibition oil recovery from fractured, water-drive reservoir. *SPE J.*, 2(02):177–184. <https://doi.org/10.2118/187-PA>.
- Moreno, R., Bonet, E., and Iatchuk, S. (2010). Residual-oil saturation for very long unconsolidated core, with live oil at reservoir conditions. *SPE Latin American and Caribbean Petroleum Engineering Conference, 1-3 December, Lima, Peru*. <https://doi.org/10.2118/139322-MS>.
- Nelson, R. (1975). *Fracture permeability in porous reservoirs: experimental and field approach*. PhD thesis, Department of Geology, Texas AM University, College Station, TX, 77843.

- Nelson, R. (2001). *Geologic Analysis of Naturally Fractured Reservoirs*. Gulf Professional Publishing, 2 edition.
- Perkins, F. M. and Collins, R. E. (1960). Scaling laws for laboratory flow models of oil reservoirs. *J Pet Technol*, 12(08):69–71. <http://dx.doi.org/10.2118/1487-G>.
- Peters, E. J. (2012). *Advanced petrophysics Volume 1: Geology, porosity, Absolute permeability, heterogeneity, and geostatistics*, volume 1. Live Oak Book Company.
- Peters, E. J., Afzal, N., and Gharbi, R. (1993). On scaling immiscible displacements in permeable media. *Journal of Petroleum Science and Engineering*, 9(03):183–205. [https://doi.org/10.1016/0920-4105\(93\)90014-6](https://doi.org/10.1016/0920-4105(93)90014-6).
- Peters, E. J. and Flock, D. L. (1981). The onset of instability during two-phase immiscible displacement in porous media. *SPE J.*, 21(02):249–258. <http://dx.doi.org/10.2118/8371-PA>.
- Pozzi, A. L. and Blackwell, R. J. (1963). Design of laboratory models for study of miscible displacement. *SPE J.*, 3(01):28–40. <https://doi.org/10.2118/445-PA>.
- Rapoport, L. A. (1955). Scaling laws for use in design and operation of water-oil flow models. *Trans., AIME*, 204(01):143–150. <https://doi.org/10.2118/415-G>.
- Rapoport, L. A., Carpenter, C. W., and Leas, W. J. (1958). Laboratory studies of five-spot waterflood performance. *Trans., AIME*, 213(01):113–120. <https://doi.org/10.2118/677-G>.
- Rapoport, L. A. and Leas, W. J. (1953). Properties of linear waterfloods. *J Pet Technol*, 5(05):139–148. <https://doi.org/10.2118/213-G>.
- Rayleigh, J. (1915). The principles of similitude. *Nature*, page 396–397. <https://doi.org/10.1038/096396d0>.

- Ruark, A. (1935). Inspectional analysis; a method which supplements dimensional analysis. *Journal of the Elisha Mitchell Scientific Society*, 51(01):127–133. [www.jstor.org/stable/24332065](http://www.jstor.org/stable/24332065).
- Sheidegger, A. E. (1954). Directional permeability of porous media to homogeneous fluids. *Geofisica pura e applicata*, 28(1):75–90. <https://doi.org/10.1007/BF01992394>.
- Sheidegger, A. E. (1956). On directional permeability. *Geofisica pura e applicata*, 1(33):111–113. <https://doi.org/10.1007/BF02629951>.
- Shook, M., Li, D., and Lake, L. W. (1992). Scaling immiscible flow through permeable media by inspectional analysis. *In situ*, 16(04):311–349. .
- Stephansson, O., Jing, L., and Tsang, C.-F., editors (1996). *Coupled Thermo-Hydro-Mechanical Processes of Fractured Media*, volume 79. Elsevier.
- Teklu, W., Brown, J., Kazemi, H., Graves, R., and AlSumaiti, A. M. (2013). Residual oil saturation determination - case studies in sandstone and carbonate reservoirs. *EAGE Annual Conference and Exhibition incorporating SPE Europec, 10-13 June, London, UK*. <https://doi.org/10.2118/164825-MS>.
- Trivedi, J. and Babadagli, T. (2008). Scaling miscible displacement in fractured porous media using dimensionless groups. *J. Petrol. Sci. Eng.*, 61(2-4):58–66. <http://dx.doi.org/10.1016/j.petrol.2008.03.001>.
- Wang, H. Y. and Samuel, R. (2016). 3d geomechanical modeling of salt-creep behavior on wellbore casing for presalt reservoirs. *Society of Petroleum Engineers*, 31(04):261–272. <https://doi.org/10.2118/166144-PA>.
- White, F. (2011). *Fluid mechanics*. New York: McGraw-Hill, 7 edition.